Multiscale modeling of mesoscale phenomena in weld pools

Kidess, Anton

DOI
10.4233/uuid:c5fd38bb-5345-48af-bca9-16f1d88744ac

Publication date
2016

Document Version
Final published version

Citation (APA)
Kidess, A. (2016). *Multiscale modeling of mesoscale phenomena in weld pools*. [Dissertation (TU Delft), Delft University of Technology]. https://doi.org/10.4233/uuid:c5fd38bb-5345-48af-bca9-16f1d88744ac

Multiscale modeling of mesoscale phenomena in weld pools

PROEFSCHRIFT

ter verkrijging van de graad van doctor
aan de Technische Universiteit Delft,
op gezag van de Rector Magnificus Prof. ir. K.C.A.M. Luyben,
voorzitter van het College van Promoties,
in het openbaar te verdedigen op vrijdag 9 december 2016 om 12:30
door

Anton KIDESS

Master of Science in Mechanical Engineering, University of Victoria

geboren te Riad

Dit proefschrift is goedgekeurd door de
promotor: Prof. dr. ir. C.R. Kleijn
copromotor: Dr. S. Kenjereš Dipl.-Ing.

Samenstelling van de promotiecommissie:

Rector Magnificus	voorzitter
Prof. dr. ir. C.R. Kleijn	Technische Universiteit Delft, promotor
Dr. S. Kenjereš Dipl.-Ing.	Technische Universiteit Delft, copromotor

Onafhankelijke leden:

Prof. dr. H.B. Dong	University of Leicester
Prof. dr. D.J. Browne	University College Dublin
Prof. dr. I.M. Richardson	Technische Universiteit Delft
Prof. dr. ir. A.A. van Steenhoven	Technische Universiteit Eindhoven
Prof. dr. ir. B.J. Boersma	Technische Universiteit Delft
Prof. dr. R.F. Mudde	Technische Universiteit Delft

This work was supported by the European Commission 7th Framework Programme for Research and Technological Development (FP7).

ISBN: 978-94-92516-22-0

Abstract

The permanent joining of metals via welding is a widely used technical process of omnipresent economic importance. It involves temporarily melting parts of the metal pieces to be joined. During that stage, the liquefied metal exhibits strong fluid flow. The mechanical properties of the welded piece depend on macroscale (=weld scale, e.g. temperature evolution during welding and joint geometry after welding) properties of the weld as well as its mesoscale (=smallest continuum scale, e.g. flow eddies during welding and grain structure after welding) and microscale (=molecular scale, e.g. chemical composition) properties.

There is a strong interaction between macroscale and meso/microscale weld properties. The ability to predict these in their mutual interaction is of great importance for improving welding technology towards better weld properties and increased weldability, especially in view of emerging new metallic engineering materials. To this end, computational modelling plays a promising role complementary to experimental studies, as it provides access to spatially and temporally resolved data that experiments cannot provide, and does not suffer from many difficulties encountered in experimental studies. The state of the art is that computational welding models have separately addressed either macroscale or mesoscale or microscale weld properties.

In this thesis, the modelling of the mutual interaction between macroscale (weld shape evolution and macroscale flow and temperature distribution) and mesoscale (grain structure and mesoscale flow structures) phenomena in the welding process is addressed. A mathematical model to simulate conduction mode laser welding is developed and used to gain fundamental insight into the influence of the flow of liquid metal on the macroscale and mesoscale evolution of the weld.

First, the interaction between macroscale flow and heat transfer during welding, and mesoscale grain structure after re-solidification is addressed. The developed model was applied to investigate the deliberate grain refining of solidifying steel using non-melting particles as potential nucleation sites. Unlike previous studies, in this study the melting stage of the welding process is included, taking into account fluid flow, thus providing appropriate initial conditions for simulating the solidification stage. It is shown that the fluid flow influences the resulting mesoscale solidification structure. Above a certain threshold, the concentration of grain refining particles is found to be of little influence on the development of the structure.

Secondly, the interaction between macroscale flow and heat transfer during welding, and the occurrence of mesoscale flow instabilities is addressed. Here, the state of the art in weld pool modelling, assuming stable and laminar macroscale flows only, is at odds with experimental observations which show violent small scale flow instabilities resembling turbulence. This neglect of mesoscale flow instabilities has been hypothesized to be the main cause for the inability of weld pool models to correctly predict macroscopic weld shapes, unless case-specific and unphysical tuning

of liquid metal parameters is applied. In the present thesis, for the first time, the mesoscale hydrodynamics in the weld pool has been studied using direct numerical simulation (DNS), resolving all scales relevant for turbulence, proving that the flow of liquid steel in laser welding - where the Marangoni number, i.e. the ratio of surface tension to stabilizing viscous forces, is relatively high - is indeed turbulent.

Subsequently, after having shown that the mesoscale flow instabilities observed in DNS can be faithfully reproduced using less computationally demanding dynamic large eddy simulations, the latter technique is used to study the relation between flow instabilities and Marangoni number in the range between $\sim 2 \times 10^6$ and $\sim 3 \times 10^7$. Within this range, a transition from stable laminar flow at the lowest Marangoni numbers, via transitional flow with rotational instabilities at medium Marangoni numbers, to turbulent flow at the highest Marangoni numbers occurs. These instabilities have not been reported in previous numerical studies.

Samenvatting

Het permanent met elkaar verbinden van metalen componenten door middel van lassen is een veelgebruikt technologisch proces van grote economische relevantie. Tijdens het lassen wordt een gedeelte van het metaal tijdelijk gesmolten, waarbij er een sterke stroming in het vloeibare metaal ontstaat. De mechanische eigenschappen van de lasverbinding hangen sterk af van de macroscopische eigenschappen van de las - zoals de tijdsevolutie van de temperatuur in en om de las tijdens het lassen en de vorm en afmetingen van de uiteindelijke las - alsook van de eigenschappen van de las op meso- en microschaal - zoals stromingswervelingen tijdens het lassen en de korrelstructuur en chemische samenstelling van de gerealiseerde las. Er bestaat een sterke wisselwerking tussen de eigenschappen van de las op macroschaal en de eigenschappen op meso/microschaal, zowel tijdens als na het lassen.

Teneinde doorbraken in lastechnologie te realiseren, zowel in verbeterde laseigenschappen als in de lasbaarheid van nieuwe en nieuw te ontwikkelen metallische materialen, is het nodig om de wisselwerking tussen micro-, meso- en macroverschijnselen te kunnen voorspellen. Numerieke simulatiemodellen spelen hierbij een belangrijke rol, complementair aan experimenteel onderzoek, omdat simulaties toegang geven tot informatie, met een tijds- en ruimtelijke resolutie, die experimenteel niet behaald kan worden. Beschikbare en gepubliceerde numerieke lasmodellen zijn echter beperkt tot het afzonderlijke en ontkoppeld simuleren van ofwel de macroschaal, de mesoschaal of de microschaal.

Het doel van dit proefschrift is het modelleren van de wederzijdse interactie tussen macroschaalverschijnselen (de evolutie van de vorm van de las en de stroming en temperatuurverdeling in de las) en mesoschaalverschijnselen (de stromingswervelingen in het vloeibare lasbad en de kristalkorrelstructuur in de gestolde las). Daarvoor is een numeriek model ontwikkeld voor het gekoppeld modelleren van verschillende schalen in laser-lasprocessen. Met dit model kon fundamenteel inzicht worden verkregen in de invloed die de stroming in het vloeibare lasbad heeft op de evolutie van de las op zowel de macro- als de mesoschaal.

Ten eerste was de interactie tussen de grootschalige stroming en warmteoverdracht tijdens het lassen, en de korrelstructuur in de gestolde las onderzocht. Met het hiertoe ontwikkelde model kon worden bestudeerd hoe kleine, niet-smeltende deeltjes die als nucleatiebron aan het lasbad worden toegevoegd leiden tot een verfijning van de korrelstructuur in de las. In deze simulaties was, voor het eerst, ook de smeltfase van het lasproces en de daarin optredende stroming gemodelleerd, waaruit de correcte initiële condities voor de simulatie van het stollingsproces volgen. Het was aangetoond dat de stroming, zowel tijdens het smelten als tijdens het stollen, van belangrijke invloed is op de korrelstructuur in de las na stolling. De concentratie van de nucleatiekernen, mits boven een minimale drempel, bleek voor het verloop van de stolling en de korrelstructuur van het materiaal niet van belang.

Vervolgens is de interactie tussen de stroming en warmteoverdracht op macroschaal,

en het optreden van kleinschalige stromingsinstabiliteiten onderzocht. Daartoe hebben we, voor het eerst, de kleinschalige stroming in een smeltbad van vloeibaar metaal gemodelleerd met behulp van zogenaamde directe numerieke simulaties (DNS), dat wil zeggen met voldoende resolutie om alle turbulente schalen af te dekken. Dit onderzoek werd gemotiveerd door de discrepantie tussen bestaande lasbadmodellen, die slechts grootschalige, stabiele en laminaire stromingen modelleren, en experimentele observaties die krachtige stromingsinstabiliteiten op kleine schaal laten zien. In de literatuur bestond het vermoeden dat het buiten beschouwing laten van kleinschalige stromingsinstabiliteiten de belangrijkste reden is voor het onvermogen van bestaande lasbadmodellen om de juiste vorm van gestolde las te voorspellen, tenzij in deze modellen de materiaaleigenschappen van het stromende vloeibare metaal ad-hoc en op niet-fysische wijze worden gebruikt als fitparameter. Met behulp van DNS wordt in dit proefschrift aangetoond dat, door het optredende relatief grote Marangonigetal, de stroming in een smeltbad van vloeibar staal onder een laser straal inderdaad turbulent is.

De in DNS geobserveerde kleinschalige stromingsinstabiliteiten en -turbulentie konden kwantitatief worden gereproduceerd met behulp van, veel minder rekenkracht vereisende, dynamic large eddy (LES) simulaties. Deze techniek is gebruikt om de relatie te onderzoeken tussen het Marangonigetal en de aard van de stroming in het smeltbad, voor Marangonigetallen tussen $\sim 2 \times 10^6$ en$\sim 3 \times 10^7$. Bij de laagste onderzochte Marangonigetallen is de stroming stabiel, symmetrisch en laminair. Bij hogere Marangonigetallen verschijnen grootschalige, periodiek oscillerende rotationele stromingspatronen. Bij nog grotere Marangonigetallen wordt de stroming volledig turbulent. Het optreden van dit scala aan instabiliteiten in dit soort stromingen is in dit werk voor de eerste keer numeriek aangetoond.

Zusammenfassung

Das permanente Verbinden von metallischen Werkstoffen mittels Schweißen ist ein weit verbreiteter technischer Prozess von hoher wirtschaftlicher Bedeutung. Dabei werden die zu verbindenden Teile zeitweise geschmolzen, wobei am Schweißpunkt im flüssige Metall eine starke Strömung entsteht. Die mechanischen Eigenschaften der Verbindung hängen stark von den makroskopischen Eigenschaften der Schweißnaht ab - z.B. der zeitlichen Evolution der Temperatur in und um die Naht während des Schweißens und die Form und Abmessungen der Naht nach dem Schweißen - sowie von den Eigenschaften der Naht auf Meso- und Microskala - z.B. kleinskalige Strömungsverwirbelungen und der Kristallstruktur und chemischen Zusammenstellung.

Es gibt eine starke Wechselwirkung zwischen den makroskopischen Eigenschaften der Schweißnaht und den Eigenschaften auf Meso- und Mikroskalen. Um Schweißtechnologie zu verbessern, sowohl was die Eigenschaften der Naht als auch die Schweißbarkeit von neuen Werkstoffen betrifft, ist es wichtig diese Wechselwirkungen zwischen Phänomenen auf Mikro-, Meso- und Makroskalen zu verstehen und vorhersagen zu können. Numerische Simulationsmodelle spielen hier als Komplement zu Laborexperimenten eine entscheidende Rolle, da sie, auch abgesehen von den enormen experimentellen Herausforderungen beim Schweißen, Informationen mit räumlicher und zeitlicher Auflösung liefern die Experimente nicht bieten können. Der aktuelle Stand der Technik von Schweißmodellen ist das unabhängige, d. h. nicht-gekoppelte, Untersuchen von entweder der Makroskala, der Mesoskala oder der Mikroskala.

Das Ziel dieser Dissertation ist das Modellieren der gegenseitigen Interaktion zwischen der Makroskala (die Evolution der Form der Schweißnaht und die Strömung und Temperaturverteilung in der Naht) und der Mesoskala (kleinskalige Strömungswirbel im flüssigen Metall und die Kristallstruktur nach Erstarren). Hierzu wurde ein numerisches Modell entwickelt um die Effekte auf den verschiedenen Skalen gekoppelt untersuchen zu können, und mit Hilfe dessen ein elementares Verständis des Einflusses der Strömung im flüssigen Schweißbad auf die Evolution der Naht sowohl auf der Meso- als auch auf der Makroskala gewonnen wurde.

Zuerst wurde die Interaktion zwischen der makroskopischen Strömung und des Wärmetransports während des Schweißens und der Kristallstruktur nach dem Erstarren der Naht studiert. Mit dem entwickelten Modell konnte untersucht werden, wie als Nukleationskeime hinzugefügte, nicht-schmelzende Partikel eine Verfeinerung der Kristallstruktur auf Mesoskala herbei führen können. In diesen Simulationen wurde, erstmalig, auch die Schmelzphase des Schweißprozesses und die dabei auftredende Strömung modelliert, womit realistische Anfangsbedigungen für die Simulation des Erstarrungsprozesses vorlagen. Es wurde gezeigt, dass die Strömung sowohl während des Schmelzvorgangs als auch während des Erstarrens einen wichtigen Einfluss hat auf die Kristallstruktur in der Naht. Die Konzentration der

Nukleationskeime, sofern über einer minimalen Grenze, ist für den Verlauf des Erstarrungsprozesses unbedeutend.

Weiterhin wurde die Interaktion zwischen der Strömung und des Wärmetransports auf der Makroskala, und dem Auftreten von kleinskaligen Strömungsinstabilitäten untersucht. Dazu haben wir, erstmalig, kleinskalige Strömungseffekte in einem Schmelzbad mit Hilfe von direkten numerischen Simulationen (DNS), d. h. mit genügend hoher räumlicher und zeitlicher Auflösung um alle turbulente Skalen abzudecken, untersucht. Der heutige Stand von Schweißbadmodellen basiert auf der Annahme von großskalig stabilen und laminaren Strömungen, die nicht im Einklang stehen mit experimentellen Beobachtungen von kräftigen kleinskaligen Strömungsinstabilitäten. Das Vernachlässigen dieser Strömungsinstabilitäten wird als gewichtiger Grund vermutet für das Unvermögen der Modelle überhaupt die korrekte Form der Schweißnaht vorherzusagen, ohne Materialeigenschaften des strömenden, flüssigen Metalls ad-hoc und ohne gute physikalische Grundlage als Fitparameter zu mißbrauchen. Mit der DNS konnte hier gezeigt werden, dass die Strömung in einem Schmelzbad von flüssigem Stahl unter einem Laserstrahl tatsächlich turbulent ist. Dem berechneten Prozess liegt eine relativ hohe Marangoni-Zahl, d. h. ein großes Verhältnis von Oberflächenspannungs- zu stabilisierenden viskosen Kräften, zugrunde.

Nachdem gezeigt wurde, dass die in der DNS beobachteten auf der Mesoskala auftretenden Strömungsinstabilitäten auch mittels weniger rechenaufwändiger Grobstruktursimulation (engl.: large eddy simulation, LES) reproduzierbar sind, wurde letztere Methodik übernommen um den Zusammenhang zwischen dem Auftreten der Strömungsinstabilitäten und Marangoni-Zahlen im Bereich von $\sim 2 \times 10^6$ und $\sim 3 \times 10^7$ weiter zu untersuchen. Innerhalb dieses Zahlenbereichs gibt es für die kleinste untersuchte Marangoni-Zahl eine stabile, symmetrische, laminare Strömung, die bei größeren Marangoni-Zahlen übergeht in eine Strömung mit großskaligen, periodisch oszillierenden, rotierenden Strömungsmustern. Bei den größten Marangoni-Zahlen ist die Strömung vollkommen turbulent. Das Auftreten dieser Breite an Instabilitäten in solchen Strömungen ist mit dieser Dissertation zum ersten Mal numerisch nachgewiesen.

Contents

1. Introduction

1.1. Background

History Welding is the permanent joining of workpieces by application of heat and/or pressure, an industrial process that is ubiquitous in modern manufacturing [1]. Examples include tiny laser spot welds on multi-blade safety razors, welding of tailored blanks in the automotive industry, or welding of pipe segments in the oil and gas industry. Primitive welding has been carried out since the Bronze Age, by pouring molten bronze between two bronze parts to be joined [2] (a conceptually similar welding process is still carried out today in form of thermit welding of rails [3]). Another primitive welding technique is forge welding [4], where two hot pieces of metal are joined by hammering them together. The necessary application of pressure to the soft but not liquid material sets this type of welding apart from fusion welding, where pieces are joined by melting them at the interface. In this dissertation we will focus on fusion welding, and particularly the impact of the flow of liquid metal on the heat transfer, of which the latter naturally has a crucial effect on the properties of the weld.

In the 19th century welding profited from ever faster progress in science and engineering, such as the discovery of acetylene and liquid air which enabled oxyfuel welding [5], where the reaction of a fuel with pure oxygen produces very high temperatures (up to 3700 K [6]) useful for welding. Welding was still primarily used as a means of repair up until World War I [7], when arc welding began to replace riveting in manufacturing [8]. Here, a strong voltage is applied between a workpiece and an electrode in the welding torch. The current and voltage applied is high enough to ionize the gas between the workpiece and the electrode, creating an arc.

Welding research in the time after World War II was impacted by increasing knowledge of material properties, metallurgy [9–11] and new welding processes, such as laser welding after the advent of high power lasers in the 1970s [12]. In laser welding, a high power laser beam, typically from a Nd:YAG or CO_2 source, is targeted at the workpiece, commonly controlled by a robot. Depending on the thickness of the workpiece, a continuous or pulsed laser may be desirable. Lasers provide highly concentrated and controllable heat sources, but low light absorptivity of the target material can lead to a large waste of energy. Due to the high cost of welding lasers they are usually applied to high volume industrial processes.

The impact of weld pool flow The increasing production speed and improvements in steelmaking processes led to the observation that weldability of materials varied strongly from batch to batch. Bennett and Mills [13] observed that traces of aluminum can significantly alter the penetration of a weld, though it remained unclear how exactly the impurities affected the weld. Early theories focused on the effect of those impurities on the welding arc (e.g. Glickstein and Yeniscavich [14]), for instance through vaporization of elements such as manganese. Fluid flow was known to influence the heat transfer in fusion welding, though it was not yet understood if the motion was caused by buoyancy, surface tension gradients (due to thermal gradients [15]) or arc forces [16–18]. Roper and Olson [19] first postulated capillary flow effects due to the impurities to be significant in weld pools, though falsely ruling out liquid-vapour surface tension changes as negligible and instead suggested capillary effects at the liquid-solid interface affecting the penetration behavior. Interestingly, one of the first studies on thermocapillary flows driven by capillary effects at the liquid-gas interface [20] concluded that fluid motion due to thermally caused surface tension gradients is improbable due to the inhibiting influence of impurities. However, using high-speed video Heiple and Roper [21] were able to show that the flow direction could be altered by adding surface active elements, causing a change in the sign of the surface tension gradients. They also indicated that surface tension forces may dominate Lorentz forces in the weld pool under an arc. Later studies on laser and electron beam welding found variable weld penetration to occur without arc effects [22], stressing the importance of surface tension effects on the flow.

Numerical simulations of welding processes With the increasing power and accessibility of computers in the 1980s, numerical simulations became an important tool for welding research. Early simulations would aim at specific, tightly defined problems, such as fluid flow in the pool [18], heat transfer [23], phenomena occurring at the welding electrode [24], the welding arc [25, 26], thermo-mechanical distortion [27] or microstructure development [28]. With time, welding models would become more self-contained, such as combined simulations of the welding arc and weld pool [29–31]. An important contribution to the accurate modeling of weld pool flows, being driven mainly by capillary effects, was the development of a mathematical model to describe the combined influence of a surface active element and temperature on the liquid-gas surface tension by Sahoo et al. [32], which is still the most commonly used model used today.

The state of the art is that computational welding models have separately addressed either macroscale or mesoscale or microscale weld properties. The European Commission FP7 project MINTWELD (Modeling of Interface Evolution in Advanced Welding)*, which provided the funding for the work described in this thesis, aims at the development of an integrated multiscale model to gain increased understanding into interface evolution in welding, and ultimately lead to improved alloy design

*URL: http://cordis.europa.eu/project/rcn/91206_en.html

and process optimization to reduce cracking failures. To do so, linked models encompassing multiple time and length scales were developed to work together [33]: from atomistic ab initio and molecular dynamics models over nanoscale phase field models and mesoscale solidification models up to macroscale computational fluid dynamics (CFD) and structural finite element models (Fig. 1.1). The macroscale weld pool hydrodynamics CFD model described in this thesis is coupled to a mesoscale solidification model developed by a project partner to investigate the possibility of control of the developing microstructure during weld pool solidification (chapter 4). The CFD model has furthermore been used to answer fundamental questions about the interaction between macroscale weld pool flow phenomena and flow instabilities happening at the mesoscale leading to turbulence, described in the following.

1.2. Outline and Research questions

As described above, a permanent connection of two work pieces can be achieved by a wide range of welding processes [34]. In the present study, we focus on fusion welding processes, in particular stationary conduction mode laser welding. Conduction mode laser welding refers to the melting of material with a low power laser, where "low power" is enough to melt the material but not enough to cause significant evaporation. This process is very attractive for fundamental studies of the influence of flow on fusion welding as it exhibits a wide range of interesting physical phenomena in the liquid pool while minimizing experimental uncertainties, and keep the modeling tractable. An in-depth description of the process will be given in the next chapter, followed by a scaling analysis and description of a mathematical model to simulate the process.

Previous studies of fusion welding processes focused either on the macro-scale while neglecting mesoscale effects, such as solidification structure or small vortices in the liquid metal flow, or focused on the mesoscale while neglecting macro-scale effects, such as fluid flow. However, the macro- and mesoscale should not be separated, as they are tightly interconnected. For instance, the mesoscale solidification structure determines the macroscale mechanical properties of the weld, whereas the macroscale fluid flow and heat transfer determine the mesoscale structure. Where the macroscale heat transfer and fluid flow has been studied, commonly the mesoscale fluid structures (turbulent eddies) have not been properly resolved, leading to underpredictions of heat and momentum diffusion. In this work, a numerical model encompassing coupled effects both on macro- and mesoscale will be introduced and used to answer fundamental questions pertaining to fusion welding processes and liquid metal flows.

Chapter 4 describes the development of a coupled mesoscale/macroscale simulation model of a conduction mode welding process of a steel to which non-melting TiN particles have been added in order to control the developing microstructure during solidification of the weld pool. We will use the model to answer the questions:

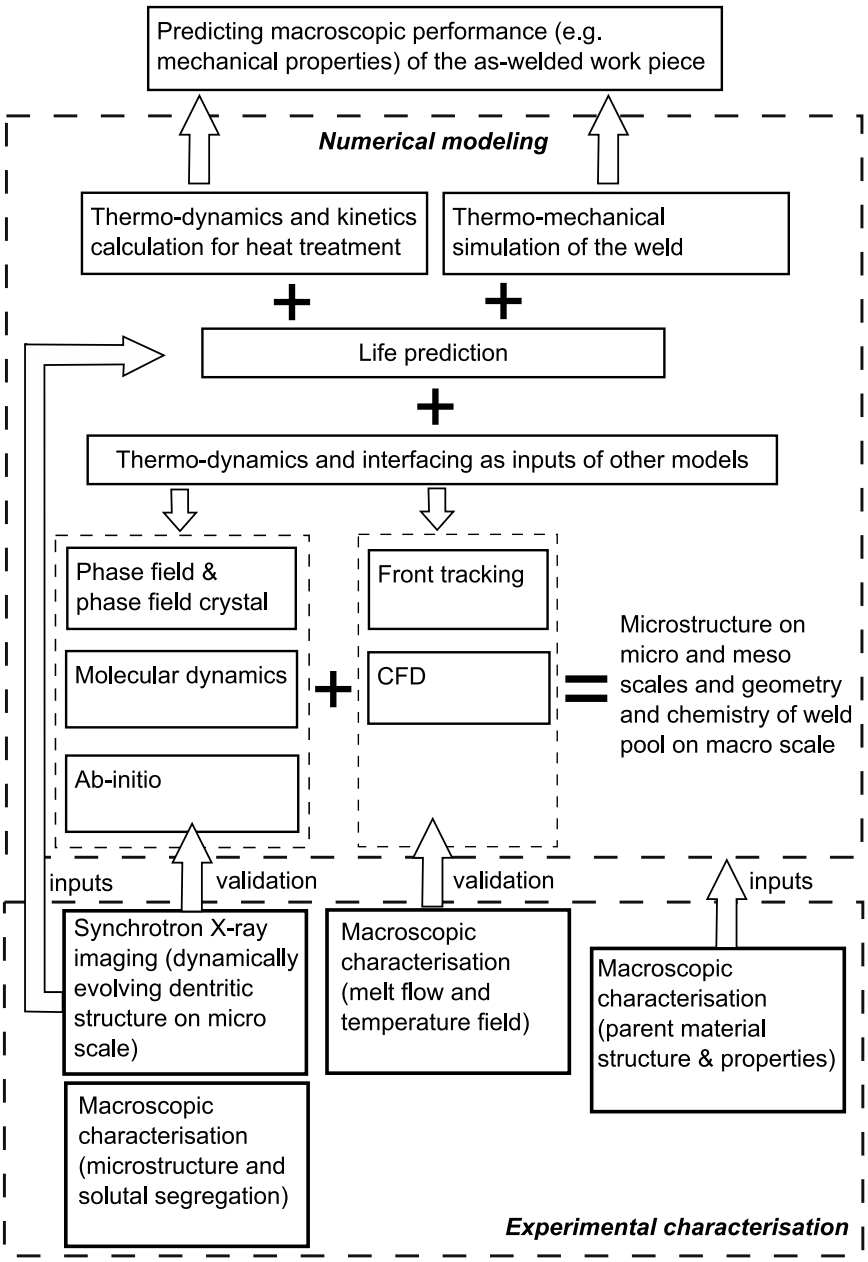

Figure 1.1.: Structure of the MINTWELD project, reproduced from Tong et al. [33]

What is

(1.1) the effect of grain refining particles on the mesoscale structure of a solidifying weld;

(1.2) the influence of fluid flow on the developing crystal structure, and

(1.3) the influence of grain refiner density on the mesoscale structure development?

Furthermore, this chapter will demonstrate the capabilities of a coupled macro-scale-meso-scale model developed as part of the MINTWELD project to investigate microstructure development during solidification.

The inadequate performance of previously published weld pool flow models to predict the post-solidification shape of a weld will be addressed in chapter 5. Specifically, the role of turbulence in weld pool hydrodynamics will be investigated using direct numerical simulations (DNS) to answer the question:

(2) Is the commonly oversimplified treatment of turbulence in weld pool models, using constant, but case specific $\mathcal{O}(10) - \mathcal{O}(100)$ *enhancement factors of diffusion coefficients to mimic turbulent transport, the reason for their inadequate performance?*

Building upon this study, the suitability of dynamic large eddy modeling (LES) to simulate wall-bounded, low Prandtl number thermocapillary flows will be investigated in chapter 6. The validated model will be used to answer the question:

(3) How, in thermocapillary liquid pool flows with surfactants, does the nature and stability of the flow depend on the Marangoni number?

1.3. Funding

I would to thank the European Commission for sponsoring the MINTWELD project (reference 229108) via the FP7-NMP program, and SURFsara for the support in using the Lisa Compute Cluster (project MP-235-12).

2. Modeling of weld pool physics

Fusion welding processes involve complex physical phenomena spanning multiple length and time scales, in particular phase changes, heat transfer by conduction, convection and radiation, as well as surprisingly strong fluid flow, all of which are tightly coupled to one another.

In any fusion welding process, an initially solid work piece will be heated by application of an external energy source in the vicinity of a joint. The heat will be transferred into the bulk of the material via conduction, and eventually the material at the joint will melt. Focusing on conduction mode laser welding [8, 34], we assume that the power density applied is not high enough to cause significant evaporation of the work piece (in terms of mass fluxes).

In the molten material, as in any liquid, surface tension varies with temperature, and surface tension gradients will lead to thermocapillary forces driving fluid motion. Due to the extreme temperature gradients encountered in weld pools the resulting thermocapillary flows may lead to significant additional transport of mass, momentum, thermal and kinetic energy. The relationship between surface tension and temperature is strongly dependent on the minor presence of surface active elements naturally present in the pool environment, leading to complex flow patterns.

In the following, several dimensionless numbers will be introduced to gauge the importance of specific transport phenomena in the weld pool. Once the significant

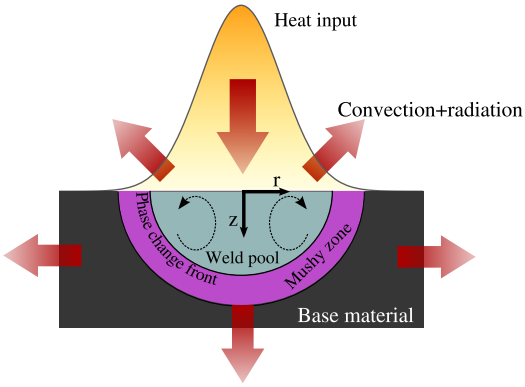

Figure 2.1.: Schematic of a laser weld pool

phenomena are identified, we can proceed to devise a mathematical model to describe the phenomena.

2.1. Scaling analysis relevant for laser welding

In this section, we will determine the orders of magnitude of the dimensionless numbers characterizing a conduction mode laser weld of a steel work piece. For symbols used in this and subsequent chapters, we refer to the nomenclature.

The laser is assumed to remain stationary, and the power density continuous (as opposed to pulsed). To compute a dimensionless number, the representative material property data shown in Tab. A.1 in the appendix will be used. Furthermore, for the order of magnitude estimates, we assume the weld pool to be of depth $D = 1\,\mathrm{mm}$ and radius $L = 1\,\mathrm{mm}$ (aspect ratio $A = D/L = 1$), and a maximum temperature difference $\Delta T = 600\,\mathrm{K}$.

The Prandtl number in liquid metals is commonly smaller than 1. In liquid steel specifically, the Prandtl number is

$$Pr = \frac{\nu}{\alpha} = \mathcal{O}(10^{-1}) \tag{2.1}$$

To estimate the relative importance of convective and conductive heat transfer, we will first have to estimate the velocities encountered in the weld pool. In turn, we first analyse the importance of the two driving forces, buoyancy and surface tension (thermocapillary). The Grashof number gives the importance of buoyancy forces to viscous forces

$$Gr = \frac{g\beta_T(T - T_s)D^3}{\nu^2} = \mathcal{O}(10^2) \tag{2.2}$$

Due to the small scales of the melt pool, the Grashof number is too small for buoyancy to solely drive convection, even if the pool were to be heated from below [35].
Buoyancy might still have an effect when combined with thermocapillary forces, however. The importance of tangential surface tension forces in driving fluid flow is gauged by the Marangoni number

$$Ma = \frac{\partial\gamma}{\partial T}\frac{D\Delta T}{\mu\alpha} = \mathcal{O}(10^4) \tag{2.3}$$

The ratio of the Marangoni number over the Grashof number gives the relative importance of tangential surface tension forces over buoyancy forces. Since the Marangoni forces are orders of magnitudes larger, we can safely neglect the influence of buoyancy forces in the shallow liquid pools of interest here.

Following Rivas and Ostrach [36]*, the characteristic surface velocity in a thermocapillary driven cavity flow can be estimated as:

$$U_s = \left(\frac{\partial \gamma}{\partial T} \frac{Q_0 \alpha}{\mu \lambda} \right)^{1/2} \tag{2.4}$$

given $Pr^{2/3} \left(A^2 Ma\right)^{1/3} \gg 1$.

Here, we find $Pr^{2/3} \left(A^2 Ma\right)^{1/3} \approx 4$. With a typical maximum heat flux density of $Q_0 = 2 \times 10^7 \,\mathrm{W\,m^{-2}}$, common both for arc and conduction mode laser welding, $U_s \approx 0.5 \,\mathrm{m\,s^{-1}}$. It is debatable if this velocity is high enough to trigger the transition from laminar to turbulent flow. A critical Ma or Re number for the onset of turbulent flow has not yet been universally established for the types of flow under consideration here, and the vast majority of welding literature is based on the assumption of laminar flow. A more detailed discussion of this question will be presented in a later chapter of this thesis, and for now we will also assume the flow in the pool to be laminar.

With the velocity scale, we can now determine the thermal Péclet number:

$$Pe = \frac{L U_s}{\alpha} = \mathcal{O}(10^2) \tag{2.5}$$

As the Péclet number is much larger than one, convection will be the dominant heat transfer mechanism in the weld pool, and the weld pool shape may be significantly altered depending on the pattern of the flow.

Finally, to estimate the importance of normal surface tension forces, i.e. the resistance to deformation of the free surface between liquid metal and the gas phase, we can obtain the capillary number as

$$Ca = \frac{\mu U_s}{\gamma} = \mathcal{O}(10^{-3}) \tag{2.6}$$

*The scaling by Rivas & Ostrach has been applied to welding by Pumir and Blumenfeld [37] as well as Chakraborty et al. [38]. Alternative scaling approaches have been presented by DebRoy and David [39] and Chakraborty et al. [40], Chakraborty and Chakraborty [41].

Due to the very high surface tension of the liquid metal, large deformations of the free surface due to fluid flow do not occur. Results from literature for confirm this conclusion [42–44].

Concluding this chapter, based on the scaling presented, we neglect buoyancy in the pool and deformation of the free surface, whereas the question of laminar or turbulent flow due to the strong Marangoni has to be investigated.

2.2. Mathematical model for conduction mode laser welding

Based on the scaling analysis in the previous section, we can present a set of governing equations to model the relevant phenomena in the weld pool. In this section we limit the discussion to conduction mode laser welding, where a defocused or low-power laser beam is directed at the target, leading to melting without significant evaporation and thermocapillary driven fluid flow. Both the heat source and the target are assumed to remain stationary[†].

Based on the scaling analysis we will assume that the free surface between the liquid metal and the atmospheric phase to not deform significantly. By this, we can completely neglect the gas phase in the model, introducing effects related to the gas phase and the free surface as boundary conditions to the governing equations. At this point no turbulence model will be introduced, meaning we assume the flow to be laminar, or the resolution of the following discretization to be high enough to fully resolve the possibly turbulent flow.

2.2.1. Governing equations

To mathematically describe the aforementioned phenomena, we require a set of equations for the transport of heat and momentum:

$$\frac{D}{Dt}(\rho H) = \nabla \cdot (\lambda \nabla T) \tag{2.7}$$

$$\frac{D}{Dt}\vec{U} = -\frac{1}{\rho}\nabla p + \nabla \cdot (\nu \nabla \vec{U}) - \vec{F}_{damp} \tag{2.8}$$

[†]A moving heat source can easily be incorporated, see sec. A.4 in the appendix.

It is convenient to rewrite the energy equation in terms of temperature. The enthalpy H is a function of temperature as well as composition described by the solid fraction g. Assuming equal density for the solid and liquid phase, we find

$$\rho H = \left(\rho g \int_{T_{ref}}^{T} c_{p,s} d\xi \right) + \left(\rho(1-g) \int_{T_{ref}}^{T} c_{p,l} d\xi \right) + \rho(1-g) h_f \tag{2.9}$$

Here, h_f is the latent heat of fusion. Introducing the assumption that also the heat capacity c_p is the same for the solid and liquid phase and independent of temperature, the relationship between the enthalpy and the temperature simplifies to

$$\rho H = \rho c_p (T - T_{ref}) + \rho(1-g) h_f \tag{2.10}$$

Now, we can rewrite Eqn. 2.7 fully in terms of temperature:

$$\frac{D}{Dt}\left[\rho c_p T\right] + \frac{D}{Dt}\left[\rho(1-g)h_f\right] = \nabla \cdot (\lambda \nabla T) \tag{2.11}$$

With $\frac{D}{Dt}\rho h_f = 0$ this leads to

$$\frac{D}{Dt}\left[\rho c_p T\right] = \nabla \cdot (\lambda \nabla T) + \rho h_f \frac{dg}{dt} + \rho h_f \vec{U} \cdot \nabla g \tag{2.12}$$

The last term in eq.2.12 is often neglected in literature (e.g. [45–49]), mostly without justification. Since ∇g is non-zero only in the vicinity of the melting/solidifying interface, where the liquid velocity is essentially perpendicular to ∇g, this term will be neglected in chapter 4 as well.

For the melting of a pure material the solid fraction g will be a step-function switching at the melting temperature. For the more general case of a phase change encountered in an alloy, melting and solidification actually takes place over a temperature range between the solidus and liquidus temperatures, T_s and T_l. Here, we assume a linear dependency on temperature, as recommended by Swaminathan and Voller [50] for steel:

$$g = \frac{T_l - T}{T_l - T_s},\ T_s < T < T_l \tag{2.13}$$

To describe the flow in the regions where the temperature lies below T_l with the same set of equations, the sink $\vec{F}_{damp}$ has been introduced into the momentum equation. Two models to determine $\vec{F}_{damp}$ will be introduced in the following section.

2.2.2. Modeling of flow in the mushy zone

2.2.2.1. Porosity technique

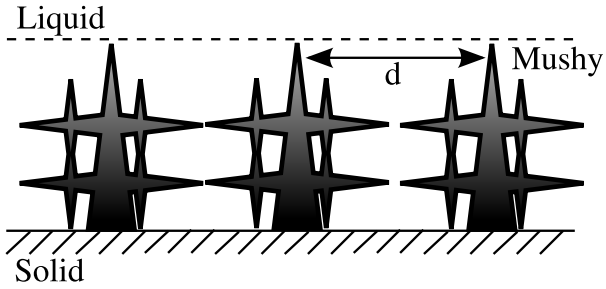

Figure 2.2.: Schematic of columnar growth with primary dendrite arm spacing d. The flow within the mushy zone is around the stationary dendrites, primarily normal towards the depicted plane.

Material within the temperature range between T_s and T_l is mushy - neither solid nor liquid. In welding, typically columnar growth is the main growth mode. Here, solidification happens non-uniformly at the solid boundaries of the domain, leading to tree-like columns of solid pointing into the liquid (Fig. 2.2), and the velocity of the solid parts is always zero. The flow within the mushy zone can then be modeled analogous to a porous medium. The relevant equation is Darcy's law [51], with $\vec{U}$ the velocity in the porous medium and K [m^2] the permeability of the medium:

$$\nabla p = -\frac{\mu}{K}\vec{U} \tag{2.14}$$

In solidification applications, Darcy's law is included in the momentum equation as a source term which at high solid fractions dominates over all other terms:

$$\vec{F}_{damp} = \frac{\mu}{\rho K}\vec{U} \tag{2.15}$$

The permeability should be a tensor which represents different permeability perpendicular and normal to the columns [52]. However, while assuming an isotropic permeability does not reflect the entire physics involved, it is very commonly done. Then, the permeability K can be expressed in terms of the solid fraction by the isotropic Blake-Kozeny equation (very similar also to the Carman-Kozeny equation):

$$K = K_0 \frac{(1-g)^3}{g^2} \tag{2.16}$$

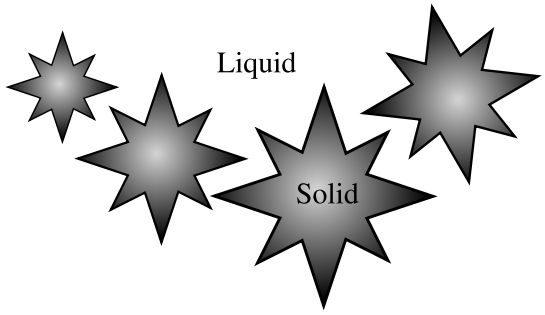

Figure 2.3.: Schematic of equiaxed solidification. The nucleated solid is modelled as spherical particles that float in the melt, effectively increasing its viscosity.

A drawback of this model is that the Blake-Kozeny equation is formally valid only for large solid fractions (> 0.3) but is typically applied to the entire range.

In the present work, the damping source term is implemented as [53–55]:

$$\vec{F}_{damp} = \frac{C}{\rho} \frac{g^2}{(1-g)^3} \vec{U} \tag{2.17}$$

There is no agreement on the value of the permeability coefficient $C = \mu / K_0$ in the published literature. The value $C = 10^6\,\mathrm{kg\,m^{-3}\,s^{-1}}$ used here lies in between the values of $C = 1.6 \times 10^4\,\mathrm{kg\,m^{-3}\,s^{-1}}$ by Rai et al. [56], $C = 1.6 \times 10^6\,\mathrm{kg\,m^{-3}\,s^{-1}}$ by Brent et al. [57], $C = 2 \times 10^6\,\mathrm{kg\,m^{-3}\,s^{-1}}$ used by Pardeshi et al. [58], $C = 1.2 \times 10^8\,\mathrm{kg\,m^{-3}\,s^{-1}}$ by Ferreira et al. (2009) and $C = 2.48 \times 10^8\,\mathrm{kg\,m^{-3}\,s^{-1}}$ suggested by Singh et al. [52].

In practice, the exact value of the permeability is not significant during melting in welding due to the high thermal gradients and very thin mushy zone, and the melt front can be assumed planar. During solidification the mushy zone will be much larger, and the permeability may be meaningfully determined based on the solidification conditions.

2.2.2.2. Enhanced viscosity technique

For substances where distinct phases cannot be determined, such as waxes [59], or when solid crystals float in the melt (Fig.2.3), which can occur due to nucleation of equiaxed dendrites due to undercooling [60], the damping of the flow due to the solid is better modeled using an alternative approach using an increased viscosity instead of a damping source term. In liquid regions the proper molecular viscosity is applied, whereas in solid regions, a very large viscosity is applied to suppress the flow. In the mushy zone some transition between those two extremes is necessary.

The equiaxed dendrites are free to move with the liquid, and with increasing solid fraction the liquid metal will turn into a slurry. We assume the particles to be spherical, and use a correlation suggested by Thomas [61] for a suspension of spherical solid particles in a liquid:

$$\mu_{equi} = \mu_0 \left(1 + 2.5g + 10.05g^2 + 0.00273\exp(16.6g)\right),\ 0 \leq g \leq g_c \tag{2.18}$$

This model, which predicts the viscosity to increase by 36% for $g = 0.1$ and by a factor 16 for $g = 0.5$, breaks down when the equiaxed network becomes coherent at high solid volume fractions. Thus, we switch to the porous medium model for equiaxed regions with a high volume fraction above a coherency threshold g_c.

In chapter 4, we will study solidification in which both equiaxed and columnar dendrites are present in the mushy zone. The influence of the first (below the coherency threshold) on the flow will be modelled through eq.2.18, whereas the influence of the second (and equiaxed dendrites above the coherency threshold) will be modelled through eq.2.17. The value of the coherency threshold g_c will be investigated in chapter 4 as well.

2.2.3. Boundary conditions for heat transfer

The governing equations are of course not complete without a complementing set of boundary conditions. For the temperature equation, boundary conditions for the absorption of laser light, as well as heat losses via convection and radiation are necessary. For the momentum equation, a shear boundary condition will be used to model the thermocapillary forces acting on the free surface.

2.2.3.1. Convective heat transfer at the boundary

At the hot boundaries natural convection will lead to a heat loss into the surrounding, mathematically described by

$$q'' = -\lambda \frac{\partial T}{\partial n} = h(T - T_\infty) \tag{2.19}$$

with n the direction of the normal outward pointing vector to the solid surface.

To apply this boundary condition, we have to determine a value for the heat transfer coefficient h. Natural convection above a hot horizontal flat plate occurs for

$$Ra = \frac{g\beta}{\alpha\nu}(T - T_\infty)L^3 > \mathcal{O}(10^3) \tag{2.20}$$

Above the hot weld pool surface, we have $Ra = \mathcal{O}(10)$. As a result, $Nu \approx 1$ and $h = Nu\lambda/L = \mathcal{O}(10)\mathrm{W\,m^{-2}\,K}$. The convective heat loss is generally small compared to the loss by radiation, and negligible compared to heat input by the laser.

2.2.3.2. Radiation

At the elevated temperatures necessary for a weld pool to develop, radiation may be a significant source of heat loss. The appropriate boundary condition is

$$q'' = -\lambda \frac{\partial T}{\partial n} = \epsilon\sigma_b(T^4 - T_\infty^4) \approx 4\epsilon\sigma T^3(T - T_\infty) \tag{2.21}$$

with $4\epsilon\sigma T^3 = \mathcal{O}(100)\mathrm{W\,m^{-2}\,K^{-1}}$.

2.2.3.3. Heat input boundary condition

The simplest way to model the laser irradiation is a top-hat distribution, where the power density is constant up to a certain radius r_q and then drops sharply:

$$I(r) = \eta \frac{P}{\pi r_q^2},\ r < r_q \tag{2.22}$$

where P is the total laser power and η is the laser absorptivity on the weld pool surface. Another commonly assumed power distribution is a radially symmetric Gaussian given by

$$I(r) = \eta k_q \frac{P}{\pi r_q^2} \exp\left(-k_q \frac{r^2}{r_q^2}\right) \tag{2.23}$$

where r_q is the radius where the laser intensity drops off to e^{-k_q} times the peak value. The most uncertain parameter in the conduction mode laser welding model is the laser absorption coefficient η. In the following section a guide to determine η will be given.

2.2.3.4. Modeling of laser absorption η

In the following, a short review of the theory of laser absorptivity by a surface will be given, and it is referred to the work of Bergström [62] for a more in-depth understanding. Only absorption of the beam at normal incidence is considered. Since the absorption (and thus energy efficiency) drops sharply with non-normal incidence angles, strictly the approach is only suitable for flat incidence targets.

The total absorption η of a laser beam on a metallic surface can be decomposed into contributions due to various internal and external effects. Internal contributions are related to multiple physical effects, all of which are considered bulk metal properties. The external contributions, including surface roughness, oxidization, and defects and impurities, are related to the surface characteristics of the work piece in question.

There are numerous correlations of varying complexity to estimate the internal absorptivity. A simple correlation for the absorptivity of ideal surfaces η_{int} is provided by the Fresnel equations, which for normal incidence of the laser beam are given by Mahrle and Beyer [63]:

$$\eta_{int} = 1 - \frac{(n-1)^2 + k_L^2}{(n+1)^2 + k_L^2} \tag{2.24}$$

The refractive index n and the extinction coefficient k_L (the subscript L refers to the laser) are wavelength dependent optical "constants" which for pure substances at room temperature can be found tabulated in literature [64–66]. For iron at room temperature and Nd:YAG laser light with $\lambda_L = 1.064\,\mu m$, $n = 3.29$ and $k_L = 4.39$, which gives an absorptivity of $\eta_{int} = 0.35$, and iron at high temperatures (1800 K) $n = 5.46$, $k_L = 3.96$ and the absorptivity is $\eta_{int} = 0.38$ [63]. These almost temperature-independent values provide a lower bound for the total absorptivity, as external contributions will increase the value.

For steel alloys with a chemical composition significantly different from pure iron the optical constants might not be known, especially at high temperatures. In this case, other correlations are necessary. A possible simple model is the Hagens-Rubens relationship (which has been extended to an extensive theory on absorption effects by Drude), which relates the absorptivity to the laser wavelength λ_L and the electrical conductivity of the absorbing material σ_e [67]:

$$\eta_{HR} = f(\lambda_L) = \sqrt{\frac{16\pi\varepsilon_0 c}{\lambda_L \sigma_e}} \tag{2.25}$$

Here, c is the speed of light and ε_0 is the vacuum permittivity. For $\lambda_L = 1.064\,\mu m$ and $\sigma_e = 1 \times 10^6\,S\,m^{-1}$ this gives $\eta_{HR} = 0.35$. However, the Hagen-Rubens relationship is only valid for normal incidence and wavelengths $\lambda_L > 15\,\mu m$ (e.g. for commonly used CO_2-lasers). For near-infrared light, such as Nd:YAG laser light, using the HR-relationship will underestimate the absorptivity.

If the optical constants for the material of interest are not tabulated in literature, and the laser wavelength is smaller than 15 µm, the absorptivity has to be calculated using the full correlations given by Drude theory. The necessary correlations can be found in literature (see e.g. Bergström [62], Dausinger and Shen [68]), but are unnecessary complex for the studies presented in this thesis.

2.2.4. Boundary conditions for momentum transfer - thermocapillary shear

Forces normal to the free surface due to surface tension only appear when the interface is not perfectly flat, i.e. its curvature is non-zero. Since here we assume a non-deforming fluid interface, we only need to determine the tangential surface force. A non-zero tangential component of the surface forces appears if the surface tension varies along the liquid surface, due to the presence of a temperature or concentration gradient. In this case liquid will start flowing from low to high surface tension areas. The shear at the free surface due to Marangoni forces is equal to the derivative of surface tension across the interface:

$$\tau = \mu \nabla_n U = \nabla_t \gamma \tag{2.26}$$

The tangential component of the surface stress, i. e. the stress due to the Marangoni force, is equal to the tangential gradient of the surface tension, which is dependent on temperature and the chemical activity a_i of surface active species:

$$\vec{F}_S = \nabla_t \gamma(T, a_i) \tag{2.27}$$

The gradient of surface tension can be expressed in terms of partial derivatives:

$$\nabla_t \gamma(T, a_i) = \frac{\partial \gamma(T, a_i)}{\partial T} \nabla_t T + \sum_i \frac{\partial \gamma(T, a_i)}{\partial a_i} \nabla_t a_i \tag{2.28}$$

The nature of the Marangoni driven flow can vary dramatically for different concentrations of surface active species (Fig.2.4). In the following, we will always assume

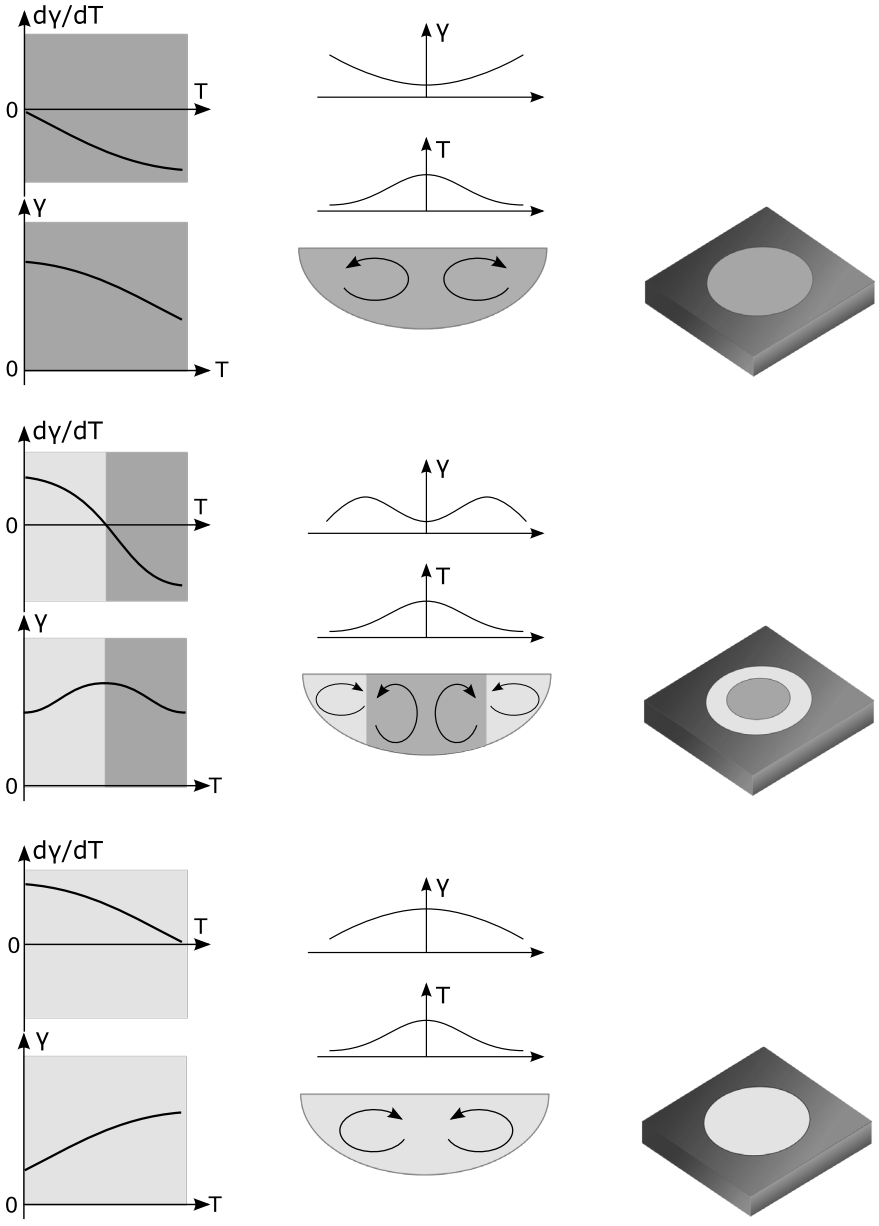

Figure 2.4.: Flow configurations for possible variations of the dependence of surface tension on temperature, e.g. due to a changing concentration of surface active species. The flow is always directed from low to high surface tension areas.

a homogeneous concentration of surface active species, and thus the solutocapillary part of the Marangoni forces, i.e. the last term of eq. 2.28, will be zero.

The first therm on the right hand side of eq. 2.28, $\partial\gamma(T,a_i)/\partial T$, is determined following a thermochemical model by Belton [69] as extended by Sahoo et al. [32], assuming homogeneous distribution of a single surfactant:

$$\frac{\partial\gamma(T,a_i)}{\partial T} = -\frac{\partial\gamma(T)}{\partial T}\Big|_{pure} - R\Gamma_s \ln(1+K_i a_i) - \frac{K_i a_i}{(1+K_i a_i)}\frac{\Gamma_s \Delta H^0}{T} \tag{2.29}$$

Here, $(\partial\gamma/\partial T)\Big|_{pure}$ is the surface tension temperature coefficient of the pure material without surfactants, R is the ideal gas constant, Γ_s the surface saturated excess concentration of surfactant, K_i the equilibrium constant for the adsorption reaction, a_i the activity of the surfactant species and ΔH^0 the heat of adsorption. Strong surface active elements are tellurium, selenium, oxygen, sulfur, phosphorus (listed in decaying order of surface active effect). Manganese, calcium, silicon, aluminum indirectly have an influence on the surface tension, e.g. by deoxidizing the melt. Concentrations of tellurium and selenium are commonly low in steel and iron, and thus their presence is usually neglected. Sulfur and oxygen have a similar effect on the surface tension, i.e. the decrease in surface tension they cause are in the same order of magnitude, and thus are sometimes lumped together into a single surfactant species concentration. Neglecting the influence of oxygen is justified when welding in a clean environment, i.e. under a oxygen-free shielding gas, or for high concentrations of aluminum which binds the oxygen and reduces its surface active effect. The surface tension temperature gradient is plotted for two exemplary surfactant concentrations in Fig. 2.5.

Even though many elements are surface active in iron [70–73], sulfur has received the most attention as it is non-reactive with tertiary elements, whereas e.g. oxygen reacts with aluminum rendering it non-surface-active [74]. Building upon the work of Belton more sophisticated models [75–82], e.g. with better correlations for ternary solutions, have been proposed but have not been applied in welding literature.

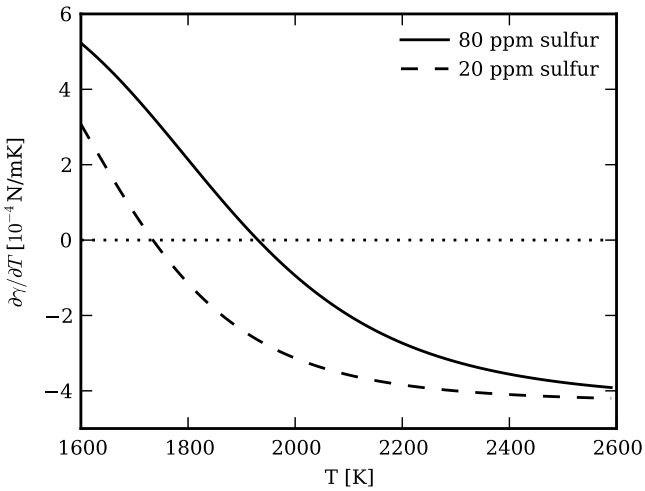

Figure 2.5.: Surface tension temperature gradient function for iron with sulfur concentrations of 20 ppm and 80 ppm determined by eq. 2.29 [32]. For 80 ppm the sign change has shifted to higher temperatures.

3. Model verification

3.1. Melting and solidification

3.1.1. 1D solidification benchmark

The implementation of the solidification algorithm described in section (sec. 2.2.1) was tested using a solidification benchmark proposed by Voller and Swaminathan [83]. The benchmark problem is the transient solidification without convection of a 1-dimensional slab of an Al-4.5%Cu alloy, which initially has a uniform temperature of 969 K above the liquidus temperature of 919 K. The slab solidifies as one side of the slab is set to a fixed temperature of 573 K, below the solidus temperature of 821 K. The results are presented in Fig. 3.1. Our prediction of the liquidus line shows excellent agreement with semi-analytical data [84] and is in fact more accurate than Voller's own numerical results. The width of the mushy region is slightly overpredicted compared to the semi-analytic results.

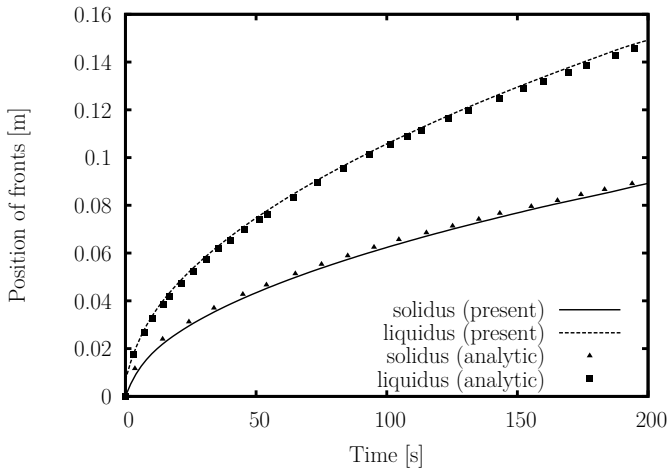

Figure 3.1.: The mushy zone evolution obtained with our present implementation compared to semi-analytical results by Voller and Swaminathan [83].

3.1.2. 2D solidification benchmark

This testcase represents a 2D casting mold of 18 cm by 18 cm filled with initially liquid Al-2wt%Cu at 700 °C. The liquid loses heat to a surrounding fixed at 400 °C, with a heat transfer coefficient of 3000 $W\,m^{-2}\,K^{-1}$. We use the symmetry of the system due to the neglect of natural convection and only model the lower left quarter of the system, such that the left and lower boundaries of the domain are walls and the other two boundaries are symmetry planes. The domain and boundary conditions are sketched in Fig.3.2.

A quantitative comparison of the reference solution given by Browne and Hunt [85] for the temperature history at a monitoring point x=3.6cm, y=4.5cm and the temperature distribution at a diagonal line throughout the domain at two time instances are presented in Fig.3.3 and Fig.3.4. Good agreement with the reference data was achieved.

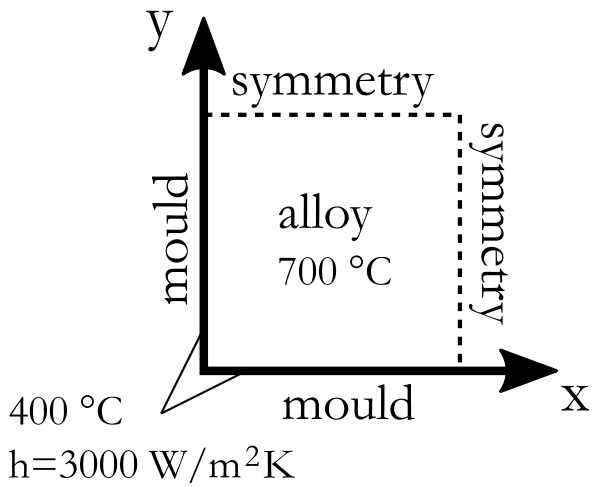

Figure 3.2.: Sketch of the domain and boundary conditions

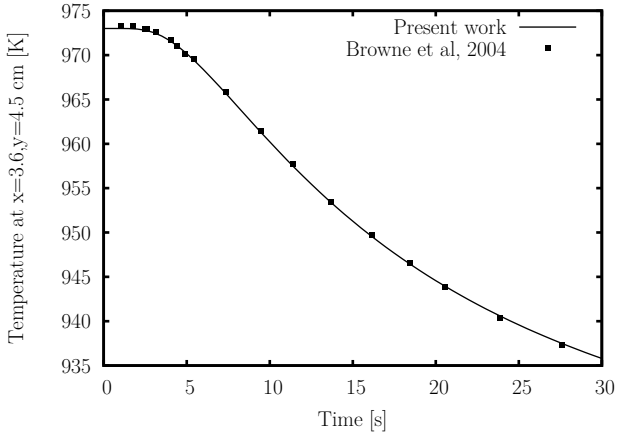

Figure 3.3.: Temperature at a monitoring point over time in the 2D solidification benchmark, comparison with reference data [85].

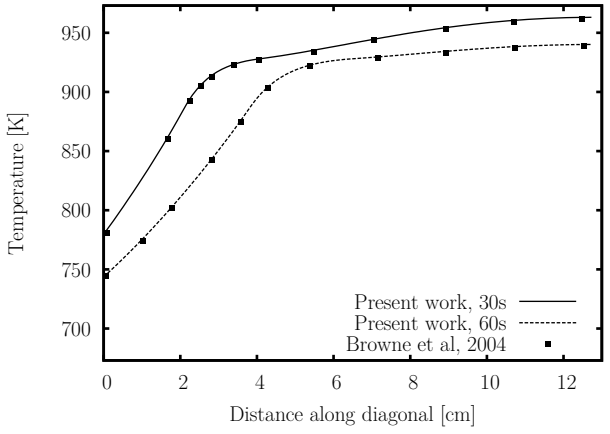

Figure 3.4.: Thermal profile at $t = 30\,\mathrm{s}$ and $t = 60\,\mathrm{s}$ along the diagonal of the casting mold in the 2D solidification benchmark, comparison with finite volume reference data [85].

3.2. Thermocapillary driven flow

3.2.1. Thermocapillary driven flow with phase change

With the test cases in the previous sections, we have tested the phase change model without fluid flow. In this section, we study a benchmark problem in which both parts are investigated together. We compute the melting of bismuth below an argon gas layer in an elongated slot (Fig.3.5) up to a steady-state. Initially the slot is filled two-thirds ($L_1 = 10\,\text{mm}$) with liquid and one third ($L_2 = 0.5L_1$) with solid bismuth, up to a height $H = 0.4L_1$. The left boundary of the slot is kept at an elevated temperature T_H above the melting temperature, and the right side at a temperature T_C below the melting temperature. At the bottom wall, a linear temperature distribution is enforced, pinning the solid-liquid interface to its initial position where the temperature is T_M. The system is placed within a microgravity environment, eliminating natural convection. The relevant dimensionless numbers are shown in Tab.3.1. The simulation results are compared with benchmark results by Tan et al. [86]. The mesh resolution is 140×65, which is slightly finer than the mesh used by Tan et al. While this benchmark is less challenging than a welding simulation due to its larger dimensions and smaller thermal gradients, it does include most of the building blocks necessary to run a basic welding simulation.

The steady state result is shown in Fig.3.6. The applied temperature gradient leads to a thermocapillary driven flow away from the hot wall towards the solid, leading to additional melting. Due to the size of the cavity, the main recirculation zone is accompanied by a weak secondary recirculation zone in the bottom left corner of the cavity. A comparison between the obtained liquid-solid interface and results by Tan et al. is shown in Fig.3.7. The small discrepancy close to the free surface is due to the simplification of a non-deformable free surface adopted in the present study, whereas Tan et al. included the (small) deformation of the liquid surface. Thus we can conclude both our phase change and thermocapillary force implementation to be valid.

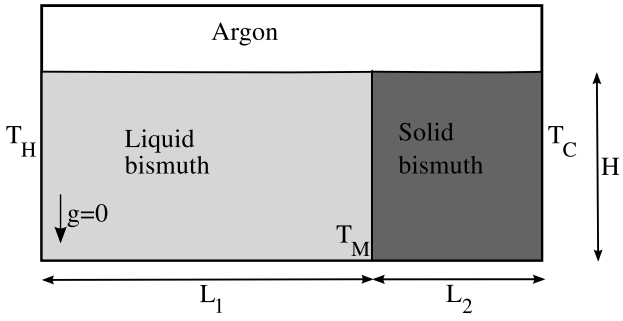

Figure 3.5.: Problem setup in the benchmark case by Tan et al. [86]

Table 3.1.: Relevant dimensionless numbers in the thermocapillary phase change benchmark

Dimensionless number	Value
$\Delta T = T_H - T_C$	12 K
$Ra = \beta_T g \Delta T H^3/(\nu\alpha)$	0.031
$Ca = (\partial\gamma/\partial T)\Delta T/\gamma$	0.0022
$Pr = \nu/\alpha$	0.019
$Bo = \rho g H^2/\gamma$	$1.88 \cdot 10^{-4}$
$Ma = (\partial\gamma/\partial T) H \Delta T/(\alpha\mu)$	244
$St = c_p \Delta T/h_f$	0.033

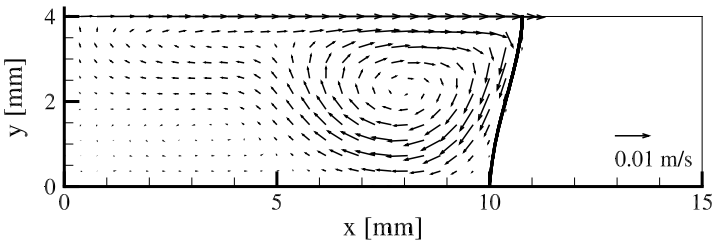

Figure 3.6.: Phase boundary and velocity vectors after 200s

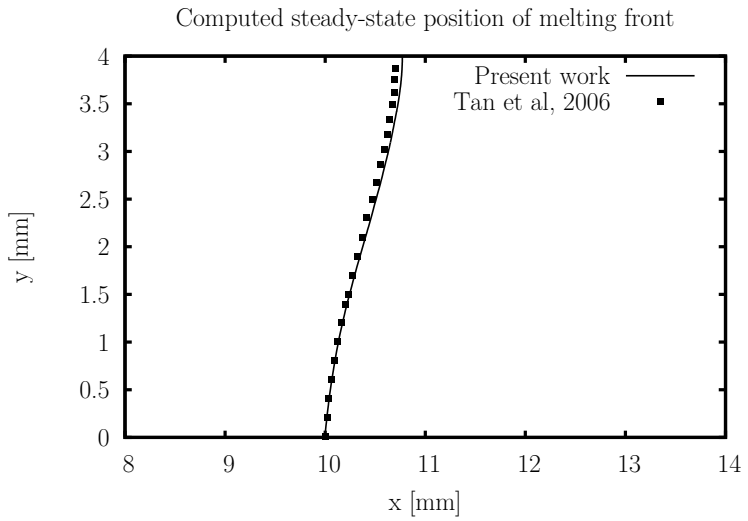

Figure 3.7.: Comparison of steady-state solid-liquid interface position

3.3. Integrated laser welding model

3.3.1. Verification of melting onset

In this test case we verify the welding model by comparison with analytical predictions by Xie and Kar [88] for the melting onset time t_m of a 1D, semi-infinite slab subject to a heat source with constant irradiance I:

$$t_m = \frac{\pi \lambda_s (T_m - T_0)^2 c_s \rho_s}{4(\eta \cdot I)^2} \tag{3.1}$$

The numerically determined onset time is compared with the theoretical prediction in Fig.3.8 using the data from Tab.3.2. The agreement is very good, verifying the temperature solution and boundary condition implementation.

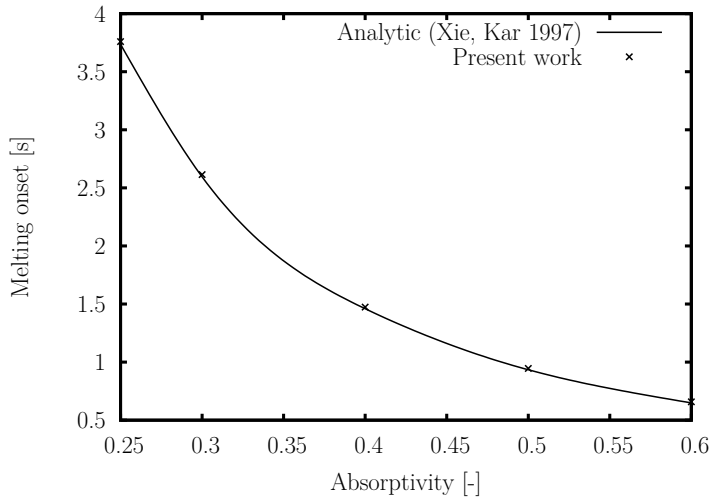

Figure 3.8.: Comparison of numerical and analytical prediction of melting onset

Table 3.2.: Data used to estimate melting onset

Property	Value
Melting temperature T_m	1770 K
Initial Temperature T_0	298 K
Thermal conductivity of solid λ_s	$40\,\mathrm{W\,m^{-1}\,K^{-1}}$
Heat capacity of solid c_s	$450\,\mathrm{J\,kg^{-1}\,K^{-1}}$
Density of solid ρ_s	$6900\,\mathrm{kg\,m^{-3}}$
Power P	2695 W
Beam radius r	5.34 mm
Absorptivity η	1
Irradiance I	$P/(\pi r^2)\,\mathrm{W\,m^{-2}}$

3.3.2. Welding case by Pitscheneder et al. (1996)

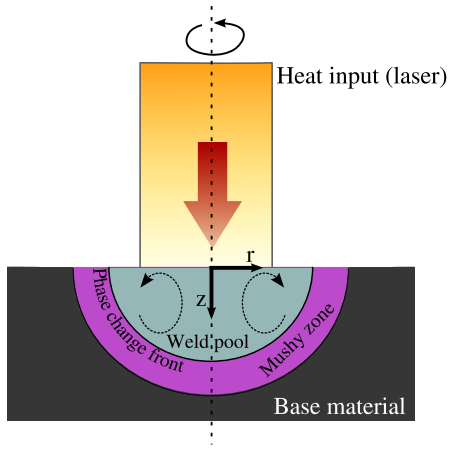

Figure 3.9.: Problem setup in the welding case by Pitscheneder et al. [89]

In this test case, we reproduce welding predictions published by Pitscheneder et al. [89], who investigated the influence of sulfur content on the temporal evolution of spot laser weld pools. In their model, Pitscheneder et al. assume a flat liquid steel-gas interface, which simplifies the modeling significantly. The computational domain consists of the weld pool and base material sketched in Fig. 3.9, and the surface tension force and laser heat flux are implemented as boundary conditions at the top boundary of the domain. Pitscheneder et al. report good agreement of their results with welding trials they conducted, yet only after enhancing the viscosity and ther-

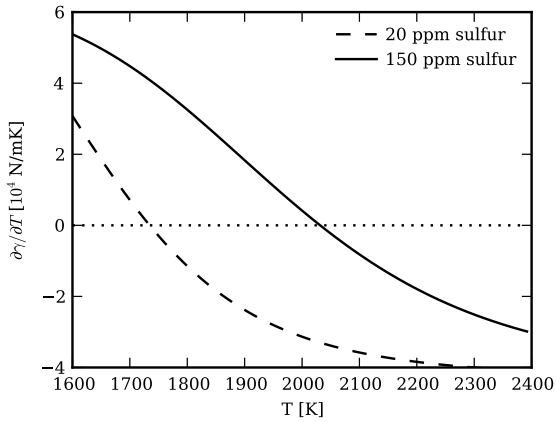

Figure 3.10.: Effect of sulfur concentration and temperature on surface tension

mal conductivity by an empirical factor of 7 compared to their molecular values in literature. In this testcase, we evaluate the capability of our model to reproduce the experimental weld pool shapes reported by Pitscheneder et al.. In doing so, we use the same set of parameters and the same enhancement factors of viscosity and thermal conductivity used by them.

The heat input is applied as a top-hat distribution with a cutoff radius of 1.4 mm. Due to this nonuniform heating a strong temperature gradient develops at the weld pool surface, which drives a flow towards areas of higher surface tension. The dependency of the surface tension gradient on temperature and surface active species concentration used by Pitscheneder et al. is shown in Fig.3.10. The surface tension gradient is predominantly negative for a sulfur content of 20 ppm, while for 150 ppm of sulfur it has a sign change at a high temperature. From this dependency, we can already predict an outwards directed flow for 20 ppm of sulfur, leading to a shallow weld pool at all laser powers. For 150 ppm, there will be a strong inwards directed flow, which for high laser powers will meet an outwards flowing vortex at the center of the weld pool.

The experimental weld pool shapes obtained by Pitscheneder et al. [89] and the simulated shapes obtained here for laser powers of 1900 W, 3850 W and 5200 W are shown in Fig.3.11. Our model performed well in reproducing the experimental results.

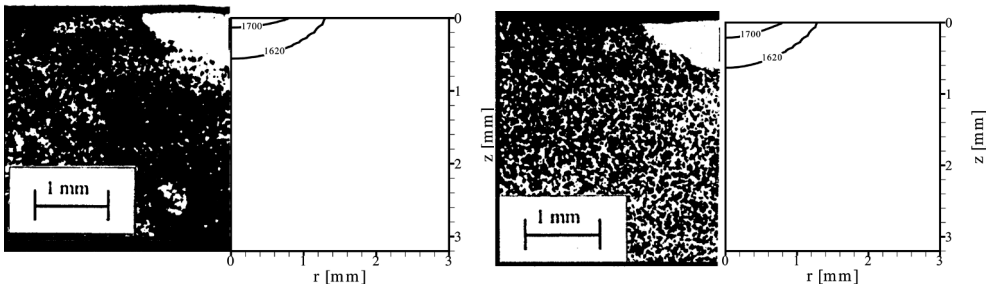

(a) Weld pool geometry for a laser power of 1900 W

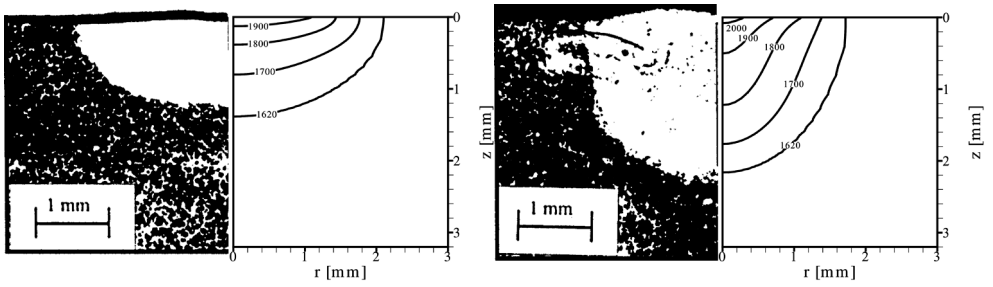

(b) Weld pool geometry for a laser power of 3850 W

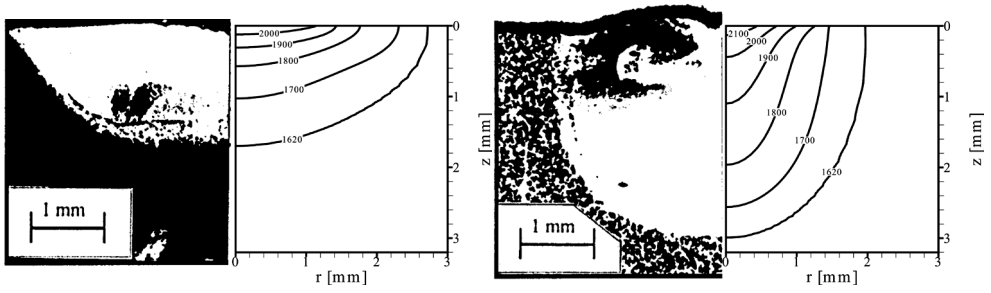

(c) Weld pool geometry for a laser power of 5200 W

Figure 3.11.: Weld pool geometry reported by Pitscheneder et al. [89] for various laser powers (experimental micrograph reproduced from reference, temperature profiles from own simulation results). Images in the left column refer to 20 ppm sulfur, images in the right column to 150 ppm sulfur.

4. An integrated model for the post-solidification shape and grain morphology of fusion welds*

4.1. Introduction

Welding is a ubiquitous industrial process of great economic and technological importance [1]. Welding processes involve complex physical phenomena spanning multiple length and time scales [33]. In particular, fusion welding processes involve phase changes, heat transfer by conduction, convection and radiation, as well as surprisingly strong fluid flow driven by Marangoni effects (gradients in surface tension), all of which are tightly coupled to one another.

Key mechanical properties of alloy welds are related both to *(i)* their shape and to *(ii)* their grain structure, and thus it is highly desirable to exert as much control as possible on both during weld formation. Whereas the shape is mainly determined by macroscopic phenomena such as heat transfer and Marangoni driven fluid flow during the melting phase, and can be largely influenced by modifying the fluid flow through the addition of surface active species [21, 89], the grain structure is mainly determined by mesoscopic (grain scale) crystallization phenomena during solidification of the melt, and can be controlled by the addition of non-melting grain refining particles [28, 90–93].

Typically, the grain morphology of a post-solidification weld consists of columnar dendrites, characterized by elongated, tree-like columns of solid which have grown into the melt. Equiaxed solidification, where solidification nucleation occurs within the melt away from the columnar front, is not common, as the thermal gradient ahead of the solidification front is too large to allow for the necessary undercooling for equiaxed growth to occur [90, 94]. However, the transition of the common columnar solidification mode to equiaxed solidification is of practical interest. Equiaxed material is less prone to the unwanted hot-cracking (tears appearing in the fusion zone near the end of the solidification process [95]) and also impedes the undesired segregation of alloying elements to the central plane of the weld [28, 91, 96].

*The contents of this chapter have been published in the International Journal of Heat and Mass Transfer 85 (June 2015), doi:10.1016/j.ijheatmasstransfer.2015.01.144.

Since quantitative experimental research of macroscopic shape evolution and mesoscopic structure evolution in welds is tremendously difficult to conduct [97], there is a need for efficient, realistic numerical models that can predict both [98].

The majority of previously published numerical studies (e.g. [42, 89, 99–101]) on macroscopic phenomena during welding have focused on the evolution of the weld pool shape and temperature up to the end of the melting stage, and thus neglect further changes in the weld pool shape during re-solidification after the heat source has been removed. However, it has been shown that the shape of the weld pool can still change significantly during the subsequent re-solidification [102, 103]. A proper study of macroscopic weld formation should therefore include the solidification stage.

Other previous studies have focused on predicting the post-solidification mesoscopic grain structure of the weld, which is entirely determined during the solidification stage. In these studies the microstructure was either studied by a-posteriori analysis, neglecting undercooling of the melt and the possibility of heterogeneous nucleation sites (e.g. Zhang et al. [101]), or the solidification progression was modeled using mesoscopic models, while neglecting the influence of macroscopic phenomena such as fluid flow in the molten metal on the weld pool shape [28, 104–108].

However, the macroscale and the mesoscale cannot be separated, as macroscale phenomena such as fluid flow and heat transfer determine the evolution of solidification on the mesoscale as well. Therefore, a proper prediction of weld properties requires a combination of both types of modeling. In this paper we present such an integrated macroscale/mesoscale model and we show that it can be used to simultaneously predict the macroscopic shape and the mesoscopic grain structure of a solidified conduction-mode laser weld. On the macroscale, we compute the heat transfer and (thermocapillary driven) fluid flow in the weld. On the mesoscale, the solidification evolution is determined from actual interface kinetics, rather than interface equilibrium assumptions. With this integrated model, we investigate the role of fluid flow during solidification, and the possible alteration of the solidification mesostructure in a steel alloy laser weld using grain refining particles.

4.2. Mathematical formulation

4.2.1. Governing equations

A schematic of a typical stationary weld is shown in Fig.4.1, where a non-moving slab of metal is targeted by a fixed high power laser. The laser irradiation will be absorbed by the target material, leading to an increase in temperature and eventually a melting phase change. Heat will be transferred into the bulk of the welded material by conduction and convection. These phenomena are mathematically modeled with

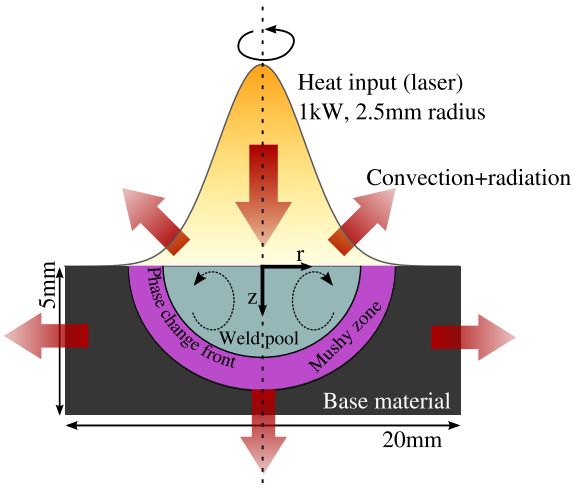

Figure 4.1.: Schematic representation of the studied laser welding. The domain is assumed to be axisymmetric.

an energy transport equation with a source term for the latent heat of the phase change

$$\frac{D}{Dt}(\rho c_p T) = \nabla \cdot (\lambda \nabla T) + S_{latent} \tag{4.1}$$

Due to the non-uniform heating of the top surface, large temperature gradients will develop. These temperature gradients result in gradients in surface tension, leading to thermocapillary forces along the liquid-gas interface driving flow in the weld pool. The momentum transport is described by the Navier-Stokes equations, with a momentum sink that models the friction in the so-called mushy zone, where the liquid and solid phase co-exist

$$\frac{D}{Dt}\vec{U} = -\frac{1}{\rho}\nabla p + \nabla \cdot (\nu \nabla \vec{U}) - \vec{F}_{damp} \tag{4.2}$$

In the following sections, we will first describe the mesoscale models used to determine the volume fraction of solid and the developing mesoscale structure during solidification, followed by a discussion of the source terms in equations 4.1 and 4.2, and their boundary conditions.

4.2.1.1. Columnar dendrite growth

At the edge of the weld pool, columnar solidification starts instantaneously once the melt starts to be undercooled. To compute the growth of columnar dendrites, we follow the model by Browne and Hunt [109]. Here, the columnar dendrite front is depicted by a series of massless computational markers which can be thought of as an envelope that connects all dendrite tips (Fig.4.2). The markers are displaced explicitly perpendicular to the local columnar dendrite front, using an analytically determined local growth velocity:

$$v = C(\Delta T_c)^2 \tag{4.3}$$

$$C = \frac{-D_l}{8m(1-\alpha_p)C_0\Gamma} \tag{4.4}$$

The growth velocity v is dependent on the undercooling $\Delta T_c = T_l - T$ and a kinetics coefficient C, which can be determined using analytical solutions of dendrite growth. Here, we use the model for C developed by Burden and Hunt [110] (equation 4.4), which is based on the hypothesis that structures grow near the optimum condition, with D_l, m, α_p, C_0 and Γ the diffusion coefficient of solute in the liquid, the slope of the liquidus line, the partition coefficient, the alloy composition and the Gibbs Thomson coefficient, respectively. Alternative growth laws, such as the KGT model [111] based on the marginal stability criterion [112], may easily be incorporated.

The markers are initialized along the liquidus isotherm once the heat source is extinguished and solidification begins. If a given marker temperature exceeds the liquidus temperature due to remelting, it is reset to the closest liquidus isotherm position [105]. Based on the location of markers, a volume fraction of mush ϕ_{col} can be determined in a given finite control volume.

4.2.1.2. Equiaxed nucleation and growth

If non-melting grain refining particles are present within the melt, there is a possibility for nucleation of equiaxed grains within the weld pool away from the columnar solidification front. Nucleants are present because they have been purposely added in the form of grain-refining particles to the weld pool, although in reality they may possibly also result from fragmentation of columnar dendrite arms. Recent work [113] has shown that dendrites bend / bow in the presence of fluid flow. Whether this leads to fragmentation has not been experimentally confirmed and therefore our model takes into account added particles only.

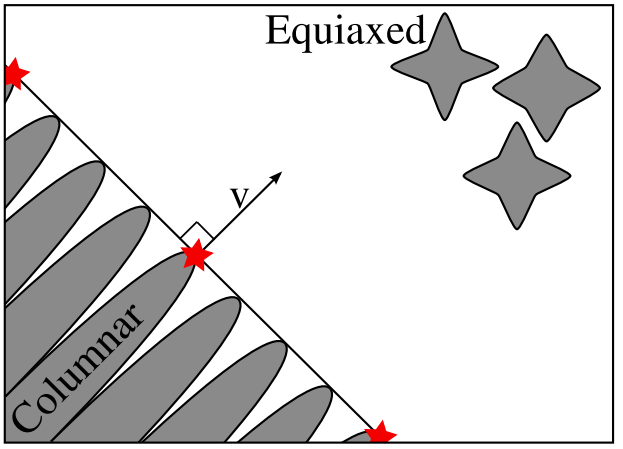

Figure 4.2.: Schematic of the mushy zone at the mesoscale, with columnar dendrite tips, equiaxed dendritic grains and computational markers (stars with velocity v) located at columnar dendrite tips

For the modeling of the nucleation and growth of equiaxed grains, we follow a volume averaging approach proposed by Mirihanage and Browne [46]. The minimum diameter of particles that can act as nucleation sites for a given undercooling ΔT_c is given by

$$d_{min} = \frac{4\gamma_{sl}}{\Delta S_v \Delta T_c} \tag{4.5}$$

where γ_{sl} and ΔS_v are the solid-liquid interfacial tension and the fusion entropy, respectively.

If the grain refiner particles were equisized, we could assume instantaneous nucleation once the necessary undercooling given by equation 4.5 is reached. More realistically, however, we assume a log-normal distribution of grain refiner particle sizes, with a median $\mu_{1/2}$ and a unitless standard deviation σ_d. The integral of the probability density function of all particles up to a size d_{min} gives the cumulative density function

$$F(d_{min}) = \frac{1}{2}\mathrm{erfc}\left(-\frac{\log(d_{min}/\mu_{1/2})}{\sqrt{2}\sigma_d}\right) \tag{4.6}$$

The number N of nucleation sites (particles larger than d_{min}) in a control volume ΔV is then given by

$$N = \rho_{seeds} \Delta V \left(1 - F(d_{min})\right) \tag{4.7}$$

or, in derivative form as

$$\frac{\partial N}{\partial t} = -\rho_{seeds} \Delta V \frac{\partial F(d_{min})}{\partial t} \tag{4.8}$$

where ρ_{seeds} is the local number density of grain refiner seeds (seeds per unit volume). The volume of equiaxed grains V_{equi} within a control volume ΔV is given by the number of nucleated grains within ΔV, and the volume of each of those grains. The change with time in V_{equi} can then be written as

$$\frac{\partial V_{equi}}{\partial t} = N \frac{\partial V_{ex}}{\partial t} + \frac{\partial N}{\partial t} V_{nuc}, \tag{4.9}$$

where $\partial V_{ex}/\partial t$ is the growth of volume of existing grains and V_{nuc} is the volume of newly nucleated grains. The growth term can be computed as

$$\frac{\partial V_{ex}}{\partial t} = \frac{4}{3}\pi \frac{d}{dt} R^3 = 4\pi R^2 v \tag{4.10}$$

The dendrite tip velocity v is computed using the same analytical growth velocity relationship used in the columnar solidification model (equation 4.3). The volume averaged dendrite envelope radius R at a given time can easily be determined as

$$R(t) = \sqrt[3]{\frac{3}{4\pi} \frac{V_{equi}(t)}{N}} \tag{4.11}$$

From equations (4.5-4.11), we may now calculate the temporal evolution of the envelope volume of equiaxed dendrites within the control volume ΔV around a location $(\vec{r}, \Delta V)$, and from this we may calculate the local equiaxed grain volume fractions as

$$\phi^*_{equi}(\vec{r}) = \frac{V_{equi}(\vec{r}, \Delta V)}{\Delta V(\vec{r})} \tag{4.12}$$

After some time the equiaxed grains have grown to an extent at which they will start feeling the presence of neighboring grains. To model this so-called grain impingement, we restrict the growth at high volume fractions using an exponential relationship known as the Avrami equation [114]:

$$\phi_{equi} = 1 - \exp(-\phi^*_{equi}) \tag{4.13}$$

4.2.1.3. Grain transport

Unlike the columnar grains that remain stationary, equiaxed grains are able to move. Since we assume the grains perfectly follow the fluid flow, the grain transport can be computed by the solution of an advection equation for the amount of nucleated grains and the equiaxed volume fraction:

$$\frac{dN}{dt} = \nabla \cdot (\vec{U}\, N) \tag{4.14}$$

$$\frac{d\phi_{equi}}{dt} = \nabla \cdot (\vec{U}\phi_{equi}) \tag{4.15}$$

4.2.1.4. Columnar to equiaxed transition

The columnar front progresses following the growth kinetics given by equation 4.3 until it meets a coherent equiaxed network. In this case, a columnar to equiaxed transition (CET) may take place, resulting in a different solidification structure. To predict this transition, for every time instance we first compute the growth of equiaxed grains independently of the presence of columnar grains. The volume fraction of the envelope of equiaxed grains is clipped in a way that the sum $\phi_s = \phi_{equi} + \phi_{col}$ of equiaxed and columnar dendrites does not exceed 1. Now we compute the evolution of the columnar dendrite tips using a mechanical blocking criterion: We assume an equiaxed envelope volume fraction ϕ_s larger than a certain threshold to be coherent in a way that it mechanically blocks further advancement of the columnar dendrite tips. Equiaxed grains that are not bound in a coherent network are integrated into the columnar dendritic network without blocking its progression. There is some variance in the published literature on the choice of the threshold value, ranging from 0.2 [115] to 1 [116]. Since we neglect solutal effects, the mechanical blocking is the only mechanism by which a columnar to equiaxed transition may take place.

4.2.1.5. Latent heat release

The effect of melting and solidification on the heat transfer are taken into account via the source term S_{latent} in equation 4.1.

$$S_{latent} = \rho h_f \frac{dg}{dt} \tag{4.16}$$

with g the volume fraction of solid material. While the heat source is active, g is evaluated as the equilibrium change of volume fraction of solid f_s

$$f_s = \frac{T_l - T}{T_l - T_s},\ T_s < T < T_l \tag{4.17}$$

During the solidification stage, when the heat source is switched off, the solid fraction g is determined from non-equilibrium solidification kinetics as a combination of the growth of equiaxed and columnar dendrites. The envelope fraction (volume fraction of mush) within a control volume is now given by $\phi_s = \phi_{col} + \phi_{equi}$. The solid fraction within that envelope (the area shaded gray in Fig.4.2) is again denoted by f_s. Now, the solid fraction g within a control volume follows from

$$g = \phi_s f_s = (\phi_{col} + \phi_{equi}) f_s = g_{col} + g_{equi} \tag{4.18}$$

Equation 4.17 has been implemented as a linear evolution of the solid fraction between T_l and T_s, in order to reduce the computational complexity of the model [109] (avoiding the need for iteration), as in this preliminary model the focus is on successfully coupling both FT and CFD models. A more physically realistic, non-linear relationship, e.g. the Lever Rule or the Scheil equation [117], could be used at the expense of computational efficiency.

4.2.1.6. Coupling of momentum and heat transport

Through the inclusion of the momentum sink term, the momentum equation 4.2 is valid for the entire domain including both liquid and solid regions. In the (semi-) solid regions, a distinction is made if it is composed of a columnar or equiaxed crystal structure. Columnar dendrites are stationary as they are attached to the unmolten solid, and thus are modeled as a porous medium, introducing a momentum sink following the isotropic Blake-Kozeny model [52]

$$\vec{F}_{damp} = \frac{\mu}{\rho K} \vec{U} \tag{4.19}$$

$$K = K_0 \frac{(1 - g_{col})^3}{g_{col}^2 + \epsilon} \tag{4.20}$$

with $\mu / K_0 = 10^6 \,\mathrm{N\,s\,m^{-4}}$ and $\epsilon = 10^{-3}$ to avoid division by zero.

Equiaxed grains are able to move with the liquid, and with increasing equiaxed volume fraction the liquid metal will turn into a slurry. We model this by increasing the viscosity in the slurry, following a correlation suggested by Thomas [61] for spherical solid particles in a liquid:

$$\mu_{equi} = \mu \Big[1 + 2.5 \phi_{equi} f_s + 10.05 (\phi_{equi} f_s)^2 + 0.00273 \exp(16.6 \phi_{equi} f_s) \Big] \tag{4.21}$$

This model breaks down when the equiaxed network becomes coherent at high volume fractions. Thus, we switch to the porous medium model eq.4.19 for equiaxed regions with a high volume fraction above the coherency threshold.

4.2.2. Boundary conditions

We assume the weld pool to be axisymmetrical and make use of this by only simulating a wedge of the domain. Circumferential gradients and velocities are zero on the wedge faces. The boundary conditions for the other faces are outlined in the following.

4.2.2.1. Heat input

At the top surface, the laser irradiation is modeled by a Gaussian distributed heat flux. At all surfaces, including the top surface, there is an outflux of heat due to natural convection and radiation. This heat outflux is very small compared to the laser irradiation, but once the latter is switched off, it is this heat outflux which together with conduction of excess heat into the unmolten material causes solidification of the weld.

$$\lambda \frac{\partial T}{\partial n} = \dot{q}_{laser} - \dot{q}_{radiation} - \dot{q}_{convection} \tag{4.22}$$

$$\dot{q}_{radiation} = \sigma_b \epsilon (T^4 - T_\infty^4) \tag{4.22a}$$

$$\dot{q}_{convection} = h (T - T_\infty) \tag{4.22b}$$

$$\dot{q}_{laser} = k_q \frac{\eta P}{\pi r_q^2} \exp(-k_q \frac{r^2}{r_q^2}) \tag{4.22c}$$

The numerical values of the input parameters are given in Tab.4.2.

4.2.2.2. Momentum

At the top gas-liquid interface, we introduce a shear stress in the liquid due to surface tension gradients (i.e. Marangoni forces) along the interface:

$$\mu \nabla_n U_t = \frac{d\gamma}{dT} \nabla_t T \tag{4.23}$$

The variation of surface tension with temperature is computed using the thermochemical model of Sahoo et al. [32].

At all other surfaces, we set the velocity to zero.

4.3. Numerical procedure

Our solver is built on top of the open source finite volume framework OpenFOAM (version 2.1.x) [118]. Postprocessing of the results for publication is done with the open source software matplotlib [119].

The non-linearity associated with the pressure-velocity-coupling is handled by the iterative PISO algorithm [120]. Once a divergence free velocity field has been computed, the temperature equation is solved. If a phase change occurs, the temperature equation will be non-linear and thus solved iteratively. The non-linearity due to latent heat during melting is dealt with using an implicit source term linearization technique [83]. Here, we assume instantaneous progression of the melting front based on local temperature conditions. While this algorithm is appropriate for melting conditions, during solidification it fails to predict undercooling and the metallurgically relevant transition from columnar to equiaxed grain growth. This deficiency is alleviated by using the mesoscale front-tracking model for solidification predictions by Browne and coworkers [109]. In this case we displace the computational markers forming the solidification front based on the temperature of a previous time step, and then iteratively determine the current temperature and solid fraction within the mushy zone (f_s in equation 4.17) with under-relaxation.

Since OpenFOAM can perform 3D simulations only, the solution domain is an axisymmetric wedge of size $r = 10\,\text{mm}$ and $z = 5\,\text{mm}$ with an opening angle of $5°$. The axisymmetric model presents a marked improvement over previously published 2D planar results e.g. by Duggan et al. [105] or Koseki et al. [107]. For the fluid flow and heat transfer equations, we use a mesh of 200x100 uniform cells. For the volume averaged approach to determine equiaxed nucleation and growth we use a mesh

that is coarse enough to ensure a reasonable amount of grain refining particles per control volume. Here, we use a uniform mesh of 160x80 cells, corresponding to an average of four grain refining particles per grid cell at $\rho_{seeds} = 1000^{3/2}\text{mm}^{-3}$. The code is arranged in such a way that the mesh for the fluid flow and heat transfer calculations can be chosen independently from the mesh used for the nucleation and growth calculations. The computations on the two meshes are fully coupled, meaning that data (temperature from macro- to meso-, and solid fraction from meso- to macroscale) is exchanged in both directions at every time step via a linear interpolation framework [33]. This allows for an independent adaptation of the fluid flow and heat transfer mesh to the mesh requirements imposed by the macroscopic length scales.

The time step is fixed at 25 µs. We use a 2nd order backward differencing time marching scheme, and a 2nd order TVD scheme (limitedLinear) for the divergence terms.

4.4. Results and discussion

Following the previous studies by Villafuerte et al. [28, 91], Park [93], Duggan et al. [105] and Koseki et al. [107, 121], we investigate a laser spot weld on an Fe-15.9wt%-Cr-14.1wt%-Ni steel alloy. To determine the growth kinetics coefficient C, this ternary alloy is treated as a pseudo-binary alloy, as the chromium segregates preferentially to the liquid and the partition coefficient of the nickel is close to 1.0, and thus the chromium is assumed to be the dominant solute [122].

In contrast to previously published computational results, we include fluid flow in our analysis, as it is known to have a strong effect on the heat transfer and shape evolution in a weld pool, both during the melting stage and the solidification stage. The influence of fluid flow on the mesoscale grain structure formation during solidification in welding has not been reported in the literature to date.

4.4.1. Weld evolution during the melting stage

The fluid flow in the pool is driven by surface tension gradients due to temperature gradients. The surface tension dependency on temperature is tightly coupled to the concentration of surface active agents (surfactants) present in any weld pool, such as sulfur and oxygen. In the following we neglect the presence of oxygen and assume sulfur is the only surfactant (homogeneously) present in the system.

A sketch of the problem investigated is shown in Fig. 4.1. The relevant material properties together with their respective literature sources are listed in Tab. 4.1. The properties related to heat inputs and losses are listed in Tab. 4.2. For simulations with

Table 4.1.: Material properties of the Fe-Cr-Ni alloy

Property	Value	Unit	Ref.
Eutectic temperature T_s	1679	K	[105]
Liquidus temperature T_l	1710	K	[105]
Specific heat capacity c_p	780	$\mathrm{J\,kg^{-1}\,K^{-1}}$	[105]
Density ρ	7250	$\mathrm{kg\,m^{-3}}$	[105]
Thermal conductivity λ	35	$\mathrm{W\,m^{-1}\,K^{-1}}$	[105]
Latent heat of fusion h_f	$1.854 \cdot 10^5$	$\mathrm{J\,kg^{-1}}$	[105]
Dynamic viscosity μ	$6.1625 \cdot 10^{-3}$	Pa s	[123]
Surface tension temperature coefficient $\partial\gamma/\partial T$	$-4.3 \cdot 10^{-4}$	$\mathrm{N\,m^{-1}\,K^{-1}}$	[32]
Entropy factor	$3.18 \cdot 10^{-3}$	–	[32]
Heat of adsorption	$-1.66 \cdot 10^8$	$\mathrm{J\,kg^{-1}}$	[32]
Surface excess at saturation	$1.3 \cdot 10^{-8}$	$\mathrm{kmol\,m^{-2}}$	[32]
Burden and Hunt growth kinetics coefficient C	$8.995 \cdot 10^{-5}$	$\mathrm{m\,s^{-1}\,K^{-2}}$	[117]
Diffusivity of Cr in the liquid D_l	$1.8 \cdot 10^{-9}$	$\mathrm{m^2\,s^{-1}}$	[117]
Gibbs-Thomson coefficient Γ	$3.88 \cdot 10^{-7}$	m K	[117]
Liquidus slope m	-2.9	K/wt%	[117]
Partition coefficient α_p	0.86	-	[117]
Solid-liquid interfacial tension γ_{sl}	0.299	$\mathrm{J\,m^{-2}}$	[105]
Fusion entropy ΔS_v	$7.71 \cdot 10^5$	$\mathrm{J\,kg^{-1}\,K^{-1}}$	[105]

grain refining particles present, unless otherwise specified we use a TiN particle density of $(1000/\mathrm{mm^2})^{3/2}$, which is the 3D equivalent of a 2D density of $1000/\mathrm{mm^2}$ as used by Koseki et al. [107]. In their simulations, Koseki et al. assign a homogeneous fixed size of grain refining particles based on a measured required undercooling of $\Delta T_c = 1.8\,\mathrm{K}$ by Bramfitt [92] to achieve nucleation of equiaxed grains on TiN particles. Here, we assume a log-normal distribution of particle sizes (Eqn. 4.6) as measured by Park [93] with parameters $\mu_{1/2} = 0.636 \times 10^{-6}\,\mathrm{m}$ and $\sigma_d = 0.1$, such that the peak of the distribution is close to the value determined by Bramfitt, while the spread of the distribution lies in-between the fixed size assumed by Koseki et al. and the wider log-normal distribution measured by Park.

The high power laser irradiation will lead to melting of the base metal in fractions of a second and thus the formation of a weld pool. For an alloy with a sulfur concentration of 200 ppm the surface tension gradient $\partial\gamma/\partial T$ is positive for temperatures up to nearly 2100 K (Fig.4.3). Since fluids flow towards regions of higher surface tension, the fluid flow will dominantly be directed towards the center of the pool, where the highest temperatures lead to the highest surface tension. Such a flow pat-

Table 4.2.: Properties related to the laser and heat losses

Property	Value	Unit
Laser power P	1000	W
Distribution coefficient k_q	2	$[-]$
Beam radius r_q	$2.5 \cdot 10^{-3}$	m
Incidence time	0.8	s
Absorptivity η	1	$[-]$
Emissivity ϵ	0.5	$[-]$
Convective heat transfer coefficient h	8	$\mathrm{W\,m^{-2}\,K^{-1}}$
Ambient temperature T_∞	300	K

tern leads to a weld pool with a width over depth ratio smaller than 1, characteristic for conduction mode welds (a weld with negligible vaporization of the melt [124]) with a high content of surface active species (Fig.4.4). At lower sulfur concentrations, the sign change of $\partial\gamma/\partial T$ is shifted towards lower temperatures (Fig.4.3). For a concentration of 80 ppm, $\partial\gamma/\partial T$ will not remain positive over the entire weld pool surface, and thus the maximum surface tension will not be located at the center of the weld pool but shifted radially outwards, close to the critical 1900 K isotherm. The liquid metal in the weld pool will flow towards this point, leading to two recirculation zones in the weld pool, resulting in decreased penetration with a characteristic bulge of the pool boundary under the stagnation point and a width to depth ratio larger than 1 (Fig.4.5).The computed maximum velocities in the weld pool are in the order of 0.3-0.4 $\mathrm{m\,s^{-1}}$, which is in good agreement with a maximum velocity of $[(\partial\gamma/\partial T)q/(\mu c_p)]^{0.5} = 0.3\,\mathrm{m\,s^{-1}}$ obtained by a scaling analysis [38], and simulation results of $0.4\,\mathrm{m\,s^{-1}}$ for comparable conduction mode laser welds [89].

Here it is illustrative to stress that neglecting fluid flow entirely, as has been done in previous studies [28, 105–108], leads to a very different, hemispherical weld pool shape, irrespective of the sulfur concentration (Fig.4.6). This highlights the need of a proper weld pool flow model to obtain an accurate initial condition for the solidification computations.

4.4.2. Weld evolution during the solidification stage

Whereas the final shape of the weld is mostly (but not entirely) determined during the heating phase, its grain morphology is fully determined during the cooling phase. Here we study the influence of accounting for solidification kinetics using our front tracking model versus the use of an equilibrium enthalpy method, and the influence of accounting for fluid flow, on the shape and morphology evolution

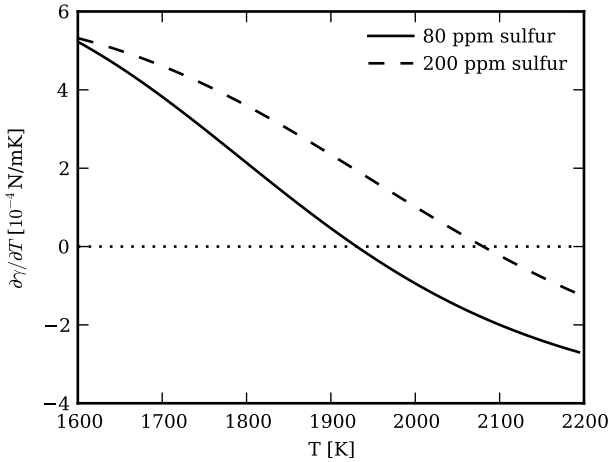

Figure 4.3.: Change of surface tension temperature coefficient with temperature and impurity concentration

during the cooling stage.

For a 200 ppm sulfur weld, the evolution of the melt pool and temperatures therein, at two time instances after deactivation of the heat source, is shown in Fig. 4.7, computed both with the commonly used enthalpy method which does not take into account growth kinetics, and with our combined front-tracking equiaxed growth model. With the latter the temperatures within the weld pool show some difference when compared to the computed temperatures using an enthalpy method. Shown are the $T_s = 1679\,\mathrm{K}$ solidus temperature isotherm and the $T_l = 1710\,\mathrm{K}$ liquidus isotherm. Notable differences are found in the location of the liquidus isotherm and these differences increase during further solidification. In the enthalpy method the solidification front is coincident with the liquidus isotherm, whereas in the front-tracking method the solidification front progression is significantly delayed resulting in a large undercooled region and a much thinner mushy zone. The same conclusion can be drawn for the completely differently shaped weld in a low (80 ppm) sulfur alloy (see Fig. 4.8). The transient position of the solidus isotherm with the two models, on the other hand, is virtually the same for both the high and low sulfur case.

Thus, simulations aimed solely at predicting the weld pool shape can be carried out with a basic enthalpy method without the need for a sophisticated solidification model. If the post-solidification grain structure is of interest however, a sophisticated solidification model, such as the one presented here, is necessary to compute accurate thermal gradients and solidification front progression, as enthalpy methods have no microstructure information.

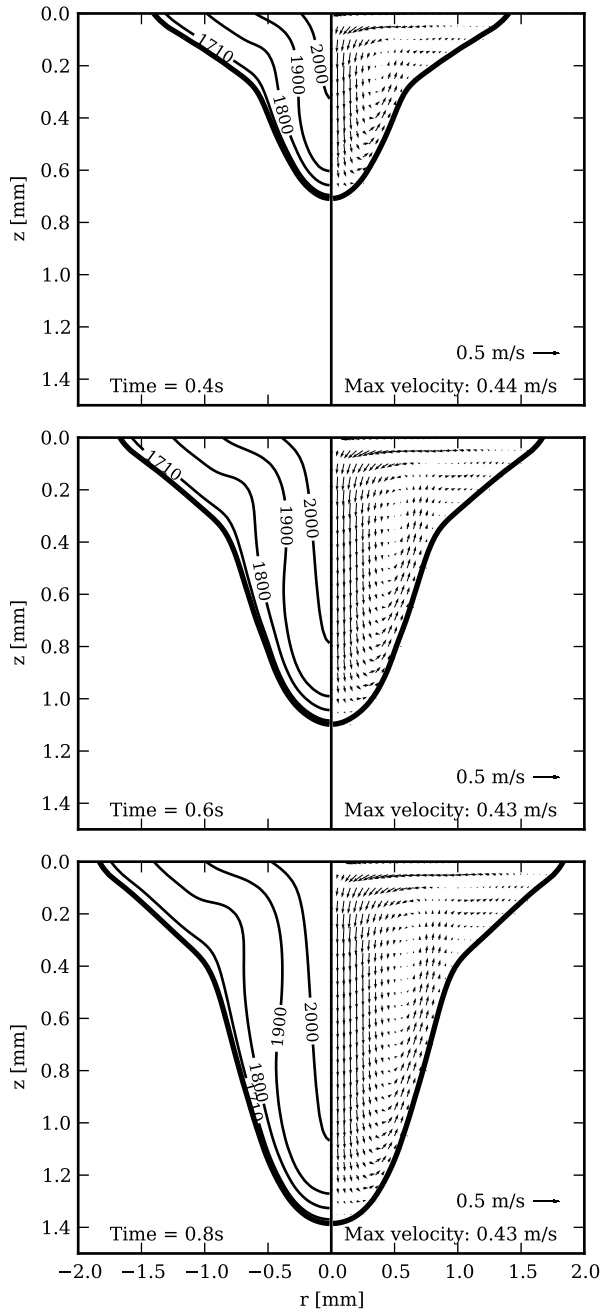

Figure 4.4.: Development of the weld pool with isotherms in Kelvin and flow velocity vectors during the heating stage at three time instances with 200 ppm sulfur. The final image shows the state at t=0.8s when the laser is shut off and solidification begins.

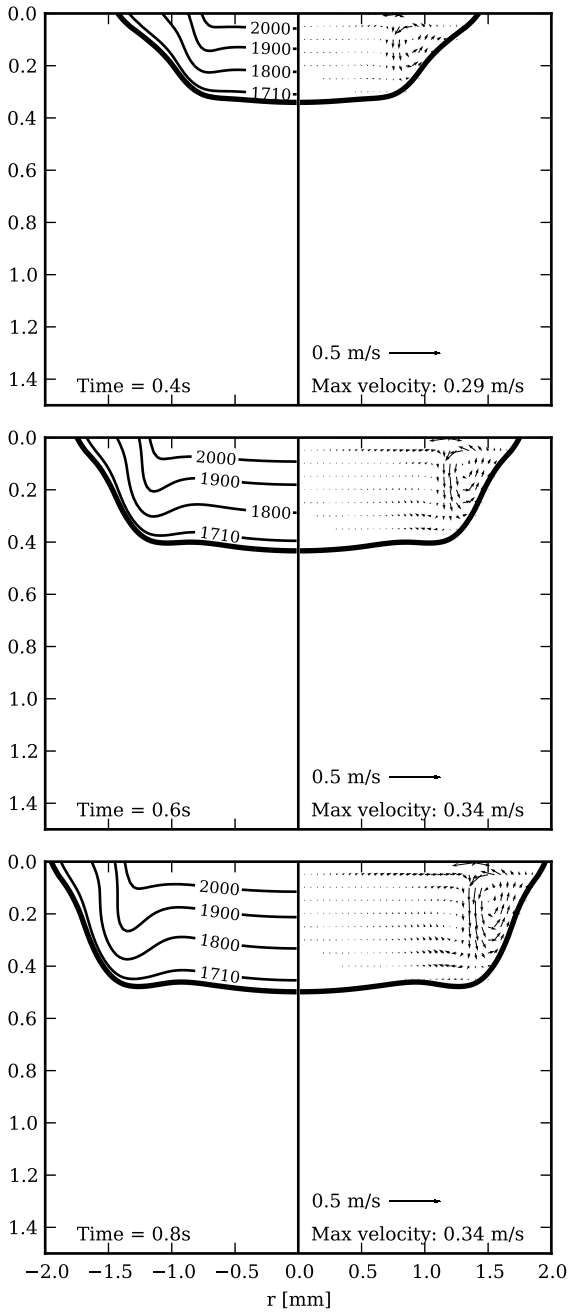

Figure 4.5.: Development of the weld pool with isotherms in Kelvin and flow velocity vectors during the heating stage at three time instances with 80 ppm sulfur. The final image shows the state at t=0.8s when the laser is shut off and solidification begins.

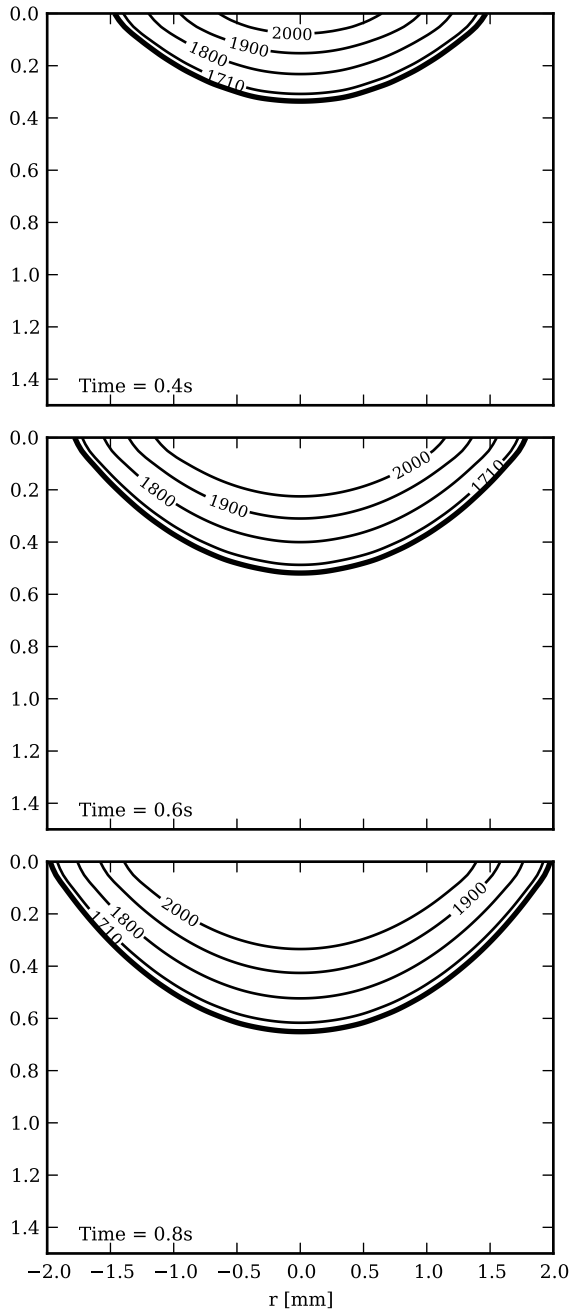

Figure 4.6.: Development of the weld pool with isotherms in Kelvin during the heating stage at three time instances with pure thermal diffusion. The final image shows the state at t=0.8s when the laser is shut off and solidification begins.

The question of the significance of fluid flow during the cooling phase on the evolution of the solidification process is addressed in Fig. 4.9 and Fig. 4.10, for high and low sulfur concentrations respectively. For both cases, starting from the same initial condition at the end of the melting phase, the solidification phase is subsequently computed with and without fluid flow. The inclusion of fluid flow in the solidification phase leads to better mixing and heat transfer, and thus lower and more uniform temperatures in the core of the weld pool. This leads to significant differences in the weld pool shape [102, 103], and more importantly in the post-solidification grain morphology, as will be shown in the next section.

For the high sulfur case, the inclusion of fluid flow, which in this case is directed inward along the weld top surface and downward along the weld axis, leads to continued heat transport to the bottom of the weld after the heat source has been switched off, and thus to continued local melting. This causes a deeper and less wide weld as compared to the situation in which fluid flow is ignored.

For the low sulfur case, the downward fluid flow and convective heat transport is weaker and further away from the axis. Yet, the inclusion of fluid flow leads to continued heat transport to the bottom of the weld after the heat source has been switched off, and a deeper weld as compared to the situation in which fluid flow is ignored.

4.4.3. Influence of grain refining particles on grain morphology evolution during solidification

Up to this point, we have investigated solidification within the weld pool in the absence of grain refining particles, leading to columnar dendritic growth only. When taking into account the promotion of equiaxed nucleation using grain refiners, at some point the columnar front progression is blocked and the solidification structure transitions into equiaxed grains. This is addressed in the current subsection.

4.4.3.1. Sensitivity to numerical and model parameters

First, we assess the sensitivity of the main simulation outcome of interest,*viz.* the location of the columnar-equiaxed transition line, as represented by the total volume of equiaxed solid in the weld, on *(i)* time step and mesh size and *(ii)* the precise value of the threshold for coherence of equiaxed grains.

Ad *(i)*: A simulation with a doubled fixed time step of 50 µs resulted in a slight increase of 4.6% of the volume of equiaxed solid (and a corresponding decrease in the volume of columnar dendritic solid). The total volumes of equiaxed solid in the weld, as computed with a fixed time step of 25 µs on three different meshes, *viz.* the standard mesh, and two meshes that are coarsened and refined by a linear factor 1.25 compared to the standard mesh (see Roache [125] for a justification of

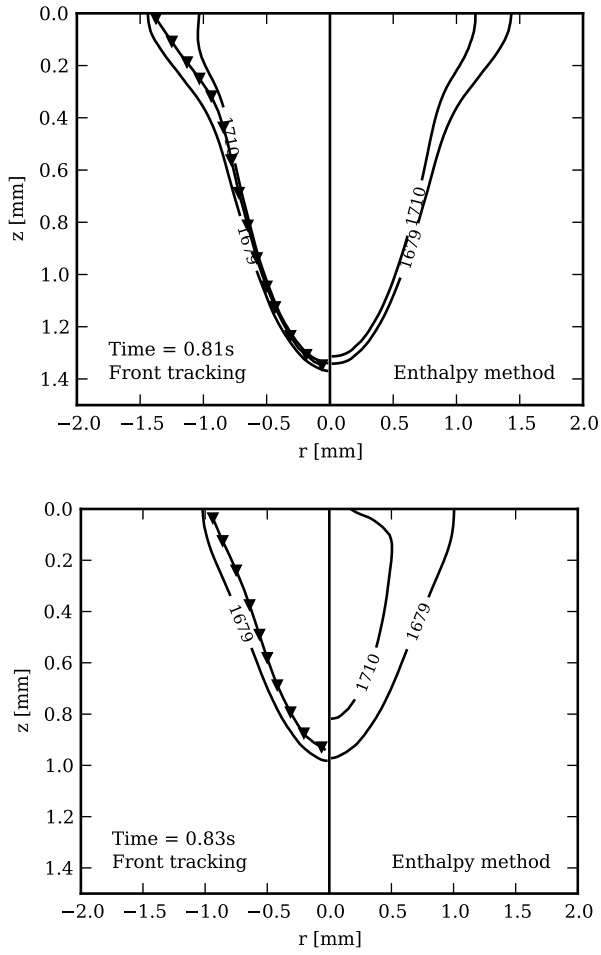

Figure 4.7.: Temperature evolution at two time instances after the heat source has been switched off at t=0.80s, for 200 ppm sulfur concentration. The location of the columnar dendritic solidification front is depicted by a line with triangle symbols.

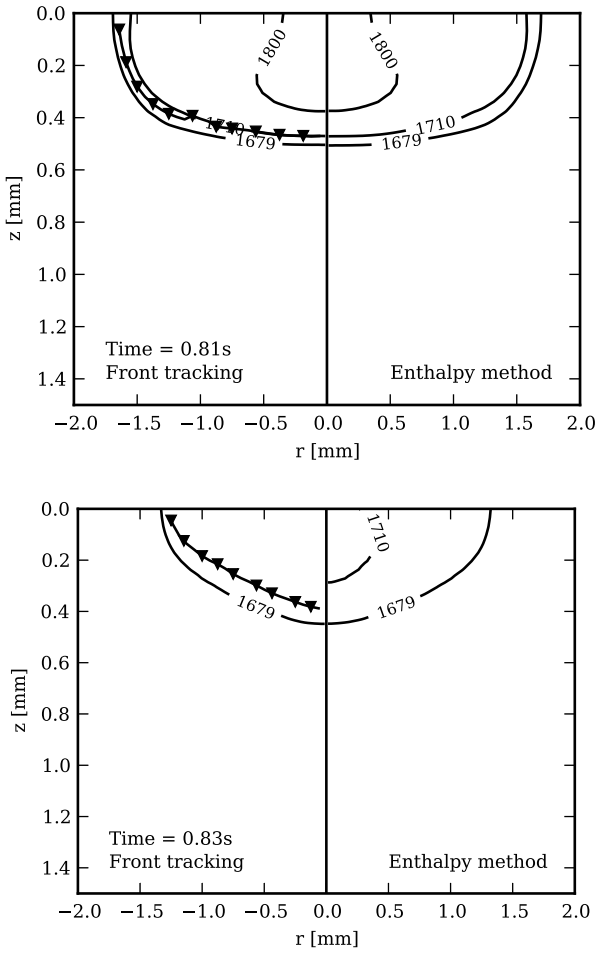

Figure 4.8.: Temperature evolution at two time instances after the heat source has been switched off, 80 ppm sulfur

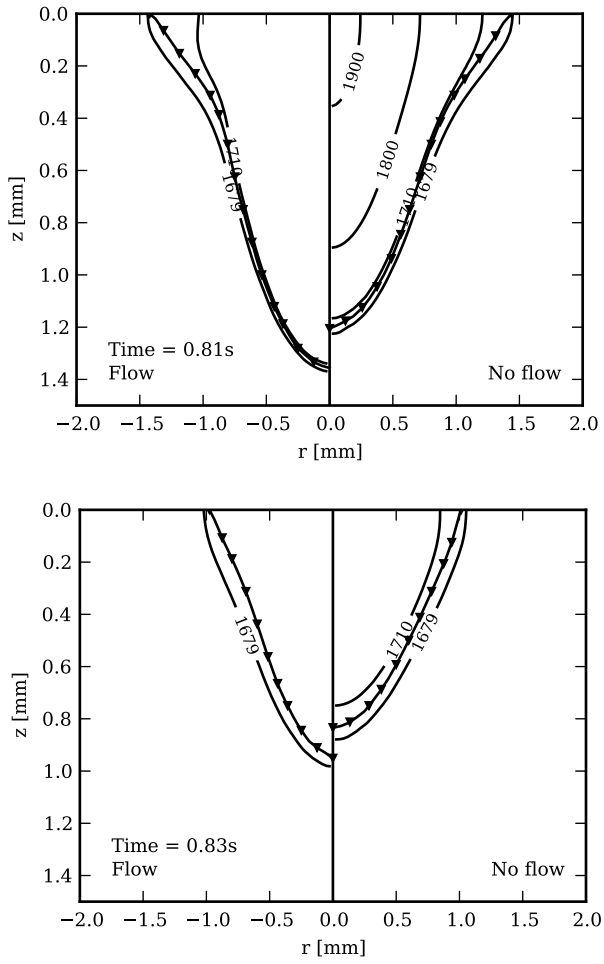

Figure 4.9.: Temperature evolution at two time instances during solidification with and without the consideration of fluid flow, 200 ppm sulfur. The line with triangle symbols depicts the location of the columnar dendritic solidification front.

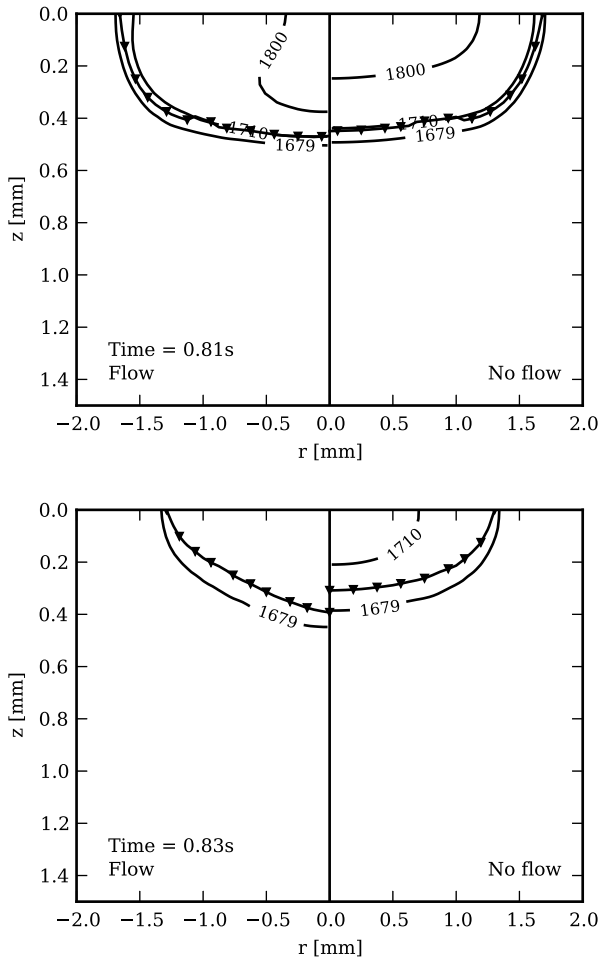

Figure 4.10.: Temperature evolution at two time instances during solidification with and without the consideration of fluid flow, 80 ppm sulfur. The line with triangle symbols depicts the location of the columnar dendritic solidification front.

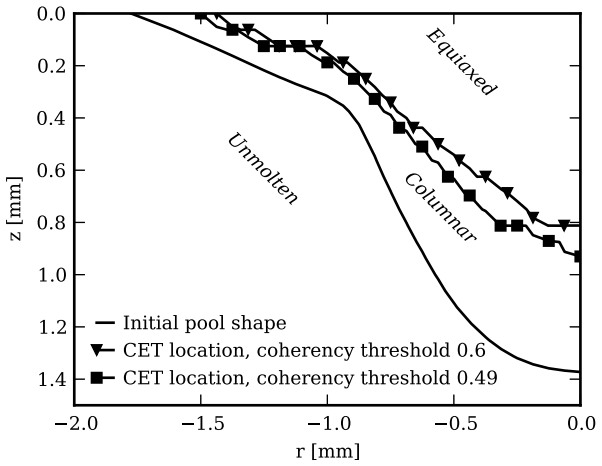

Figure 4.11.: Sensitivity on the coherency threshold of the computed transition from columnar to equiaxed solidification structure in a weld pool, 200 ppm sulfur

the refinement ratio), show a monotonic convergence, allowing for the computation of an asymptotic value by Richardson extrapolation. Compared to the asymptotic value, the coarse mesh result is 6.1% smaller, the base mesh result 2.0% smaller and the fine mesh result 0.48% smaller.

Ad *(ii)*: In a previous section, we mentioned that the precise value of the threshold for coherence of the equiaxed grains is not agreed upon in the literature (ranging from 0.2 [115] to 1[116]). To study the sensitivity of our results to this threshold value, we simulated solidification of a weld pool using a coherency threshold of 0.49 and 0.6, leading to a 15% difference in the volume of equiaxed structure in the weld (Fig.4.11). The same conclusion has been drawn by Mirihanage and Browne [46], who found the occurrence of the columnar-to-equiaxed transition (CET) in a casting to be rather insensitive to the exact value of the coherency threshold. All further simulations in the current study were performed with the most commonly used blocking threshold of 0.49 as proposed by Hunt [126].

4.4.3.2. Influence of grain transport

The presence of fluid flow in the weld pool during solidification leads to a significantly earlier transition to equiaxed growth, as can be seen in Fig.4.12 and Fig.4.13 for high and low sulfur cases respectively. Conversely, the location of the columnar-to-equiaxed transition was found to be rather insensitive to the inclusion or neglect of the transport of equiaxed grains with the flow, as described by equations (4.14) and (4.15).

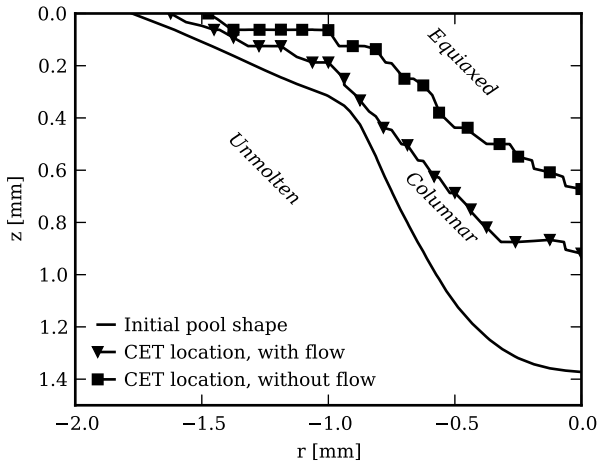

Figure 4.12.: Equiaxed transition in a weld pool with and without fluid flow, 200 ppm sulfur

Hence, the earlier transition to equiaxed growth when including fluid flow is mainly due to the lower thermal gradients and lower temperatures in the melt (see Fig.4.9), which result in a larger liquid region with sufficient undercooling for the equiaxed nucleation and growth to take place. This conclusion agrees with Hunt's criterion [126], stating that the fraction of equiaxed grains is inversely proportional to the magnitude of the thermal gradients cubed in the melt.

4.4.3.3. Influence of grain refining particle number density

The influence of the number density of grain refining particles on the transition from columnar to equiaxed solidification is illustrated in figures (Fig.4.14) and (Fig.4.15), which show that the transition to equiaxed solidification can be triggered with a grain refiner density of $500^{3/2}$ particles per mm^3, and that the position of the transition is only slightly affected by an increase of the grain refiner number density to $1000^{3/2}$ particles per mm^3. This observation matches the findings by Koseki et al. [107] that grain refiner density mainly influences the size of the resulting equiaxed grains, and not the point at which they reach coherency. Simulating the effect of a grain refiner density lower than $500^{3/2}$ particles per mm^3 is not feasible using our current volume averaged approach, as this would require very large computational cells in relation to the weld pool area to allow for a sufficient number of grain refiner particles per computational cell. In figures (Fig.4.16) and (Fig.4.17), we show the thermal gradient and equiaxed envelope volume along a diagonal line $r_{\angle} = \sqrt{r^2 + z^2}$, $z = r$ at a time instance where the equiaxed grains reach coherency.

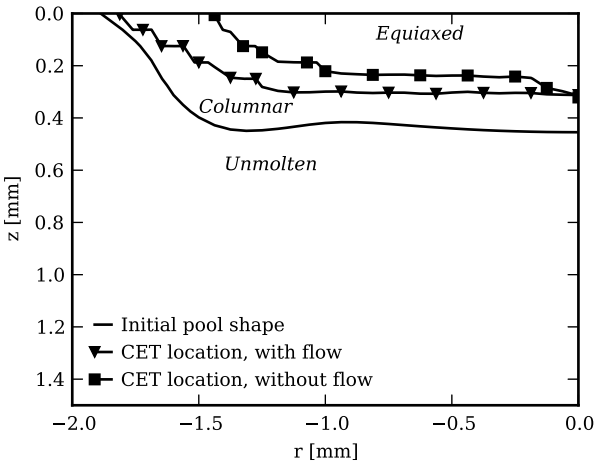

Figure 4.13.: Equiaxed transition in a weld pool with and without fluid flow, 80 ppm sulfur

We can identify a low, fairly uniform temperature gradient within the weld pool which rises sharply around the liquid-solid interface and is insensitive to the number of grain refining particles present. As a result, favorable conditions for the growth of equiaxed grains are met at the same location for both particle densities, though coherency is achieved slightly later in time for the lower number density.

4.5. Conclusion

In addition to the macroscopic shape of a weld, the mesoscopic grain morphology is crucial in determining the resultant properties. These two are determined by the interaction between macroscale fluid flow and heat transfer, and mesoscale grain solidification kinetics, during the heating and cooling phase of a welding process. Whereas both macroscale and mesoscale phenomena have previously been studied separately through computational models, an integrated model for both scales is needed to predict weld properties on both relevant scales.

Such an integrated model has been presented in the current work. The model is conceptually simple and computationally inexpensive, while granting insight into the post-solidification shape and grain morphology of a weld.

The model has been applied to study the melting and solidification of a laser spot weld on two Fe-Cr-Ni steel alloys, *viz.* with a low and high sulfur content. Due to their very different dependency of surface tension on temperature, the weld pools

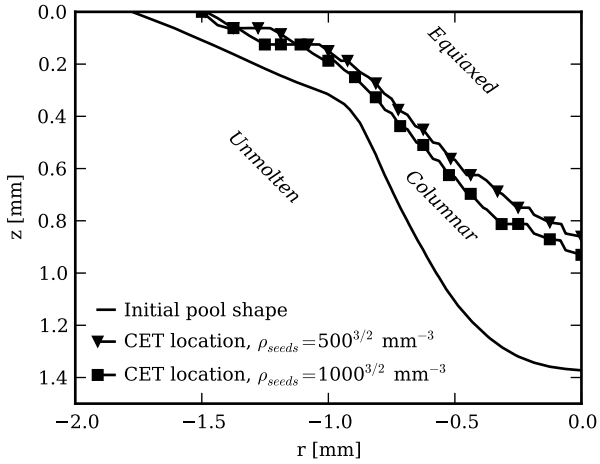

Figure 4.14.: Equiaxed transition in a weld pool with two different densities of grain refining particles, 200 ppm sulfur

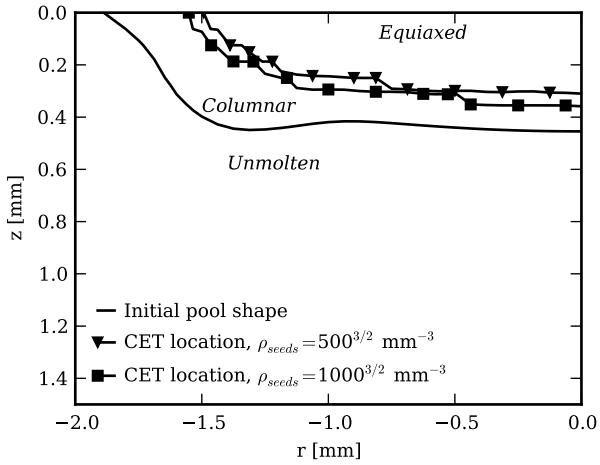

Figure 4.15.: Equiaxed transition in a weld pool with two different densities of grain refining particles, 80 ppm sulfur

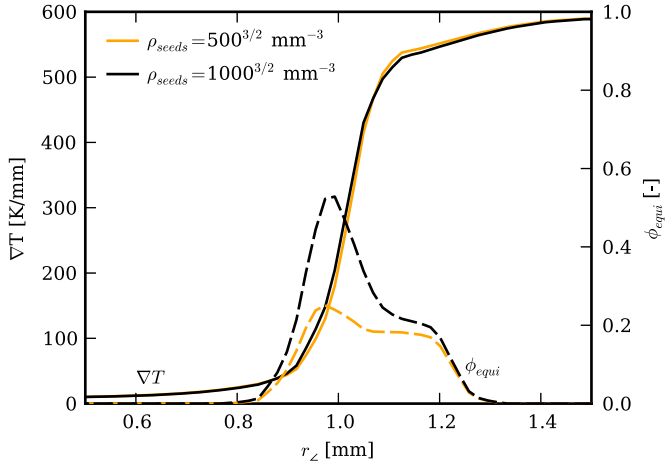

Figure 4.16.: Thermal gradient and equiaxed envelope volume fraction along a diagonal line $z = r$ away from the weld pool center, 200 ppm

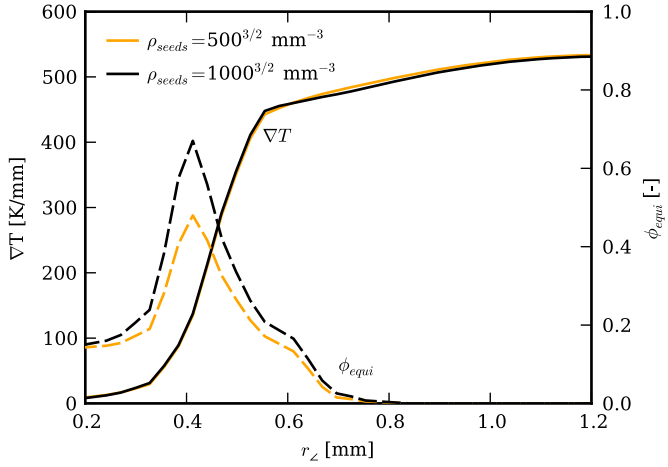

Figure 4.17.: Thermal gradient and equiaxed envelope volume fraction along a diagonal line $z = r$ away from the weld pool center, 80 ppm

of these two alloys represent the two extremes in surface tension driven flow commonly observed during welding. Although demonstrated here for laser spot welding, the presented results are relevant for arc welding as well, as both types of welding are equivalent once the heat source is turned off.

The predicted solidification evolution has been compared to that obtained with the commonly used equilibrium enthalpy method, in which solidification takes place quasi-statically and its kinetics is ignored. Apart from the obvious fact that an equilibrium method cannot predict the important transitions in grain morphology, a marked difference between the two methods was observed in the thermal gradients within the weld pool during solidification. This in turn has a strong impact on the developing grain structure. However, if only the weld pool shape, and not its grain morphology, is of interest, the equilibrium enthalpy method is found to be sufficient to obtain accurate results for the partial penetration cases examined here.

Neglecting fluid flow during the cooling phase, as done in previously reported studies, was found to have a significant influence on the predicted weld pool shape and grain morphology. Thus any accurate simulation of weld pools should include fluid flow.

The use of grain refining particles was found to be an effective means to favorably alter the grain morphology by initiating a transition from columnar to equiaxed growth. This transition was found to be not very sensitive to the most uncertain parameter in the model, *viz*. the coherency threshold value, nor to the density of grain refining particles above a certain critical value.

5. Marangoni driven turbulence in high energy surface melting processes*

5.1. Introduction

A long-standing question in the modelling of weld pool hydrodynamics is the one of the possible occurrence of turbulence and its influence on heat and momentum transfer. The underlying problem is that no welding model seems to exhibit true predictive capabilities, not even with respect to such a simple overall weld pool property as its post-solidification shape. Rather, all simulations require the adaptation of unphysical input parameters and/or material properties to truthfully reproduce experimental results. For instance, Winkler et al. [47] and Pavlyk and Dilthey [127] tune the heat input characteristics as well as the concentration of surface active species to obtain results matching experiments. More commonly, many authors (e.g. [87, 89, 127–131]) resort to the modification (i.e. enhancement) of transport coefficients, specifically thermal conductivity and viscosity, to match experimental results. No guideline has been established on how to modify the transport properties and generally they are tuned on an ad-hoc basis without any physical reasoning and a-priori dependence on weld pool properties. For example, Pitscheneder et al. [89] enhance the molecular thermal conductivity and dynamic viscosity by a constant factor 7 to match experiments, Anderson et al. [128] increase only the viscosity by a constant factor 30, Mishra et al. [132] increase only the thermal conductivity by a factor 4, De and DebRoy [129] propose an optimization algorithm to determine the best values for thermal conductivity and viscosity with multiplication factors up to 17. Even when uncertainties in boundary conditions, e.g. heat transfer efficiency and energy distribution, are minimal, such as in the conduction-mode (i.e. with negligible vaporization) laser welding experiments conducted by Pitscheneder et al. [89], enhanced transport coefficients are required to match experimental weld shapes, strongly suggesting that the published weld pool models lack the inclusion of significant physics.

Furthermore, previously published computational studies fail to report oscillations and non-axisymmetric flow patterns at the liquid surface, such as have been ob-

*The contents of this chapter have been published in the International Journal of Thermal Sciences 104 (June 2016), doi:10.1016/j.ijthermalsci.2016.01.015

served in experiments for conduction-mode laser and autogeneous gas tungsten arc welds. Kraus [133] observes that "weld pool surface temperature profiles do not reach quasi-steady-state conditions, but rather vary around some time-averaged or mean values". Zehr [44] reports that "high speed video images of the melt pool seem to reveal substantial oscillations of the free surface as the laser interacts with the workpiece". Finally, Zhao et al. show highly unstable flow with multiple flow cells using surface particle-image-velocimetry of a gas-tungsten arc-weld [134, 135].

A few hypotheses as to how to account for lacking physics, and thus improve the prediction of weld pool models, have been proposed and tested by other authors. One identified deficiency is the common comparison of post-solidification weld pool shapes with numerical simulation results not including the solidification stage. Ehlen et al. [102] and Saldi et al. [103] have determined that the weld pool shape can significantly change during this last stage of a welding process. Unfortunately, while the inclusion of the solidification stage can improve the predictions in some situations, it still does not ensure predictive capabilities [103].

Another possible source of error may be attributed to the often neglected motion of the liquid-gas interface. Simulations conducted by Ha and Kim [42] based on Pitscheneder's laser welding experiments [89] however show a very limited influence of a deformable free surface on the weld pool shape. The same conclusion has been made by Zehr [44] based on 3D simulations of conduction-mode laser welding.

Winkler et al. [47] have proposed the lack of surface chemistry and surface mass transfer processes in published models, resulting in a homogeneous distribution of surface active elements such as sulfur in the pool and at its surface, as potential source of the discrepancy. The group was able to improve their predictions using a mass transport model for a surface active element [136], and even more so when taking into account the effect of multiple surfactants [137][†]. However, even though their results using a laminar flow assumption are promising, they do conclude that there is a need to address the question of turbulent flow in weld pools. This conclusion is reinforced by the previously mentioned experimental observations of flow instabilities which are not seen in the simulations by Winkler et al. even when including the effects of surfactant redistribution.

Although sometimes done without explicit justification (e.g. He et al. [138], Roy et al. [139]), the hypothesized occurrence of turbulence has been a natural reasoning for many authors (e.g. Anderson et al. [128], Choo and Szekely [140]) to justify increasing transport coefficients, which given turbulent flow would occur naturally due to turbulent diffusion. A few authors have attempted to replace the tuning of transport properties by the use of turbulence models such as RANS (Reynolds Averaged Navier Stokes) [141–154] or LES (Large Eddy Simulation) [155]. While this leads to improved agreement with experiments (as does any increase of transport

[†]It should be noted that Winkler et al. use a value for the standard heat of absorption in disagreement with the commonly used value [32], which may have lead to fortuitous improvement of the results due to a resulting altered surface tension temperature dependency $d\gamma/dT$.

coefficients), the use of particularly RANS turbulence models developed for aerodynamics in complexly shaped, Marangoni driven weld pool flows with a free surface and non-smooth solid-liquid interface, is questionable. In fact, Pavlyk and Dilthey [127] conclude their numerical study of a gas-tungsten-arc weld with the statement "that neither an increase of the transport coefficients by a constant factor nor an application of the k-ϵ model improved the correspondence between the predicted and actual weld pool shapes", and support further investigation of the role of turbulence in such flows.

To analyze the possible role of turbulence, Chakraborty and Chakraborty [156] have presented a scaling analysis for high energy surface melting processes such as the laser welding process of interest here. The analysis allows the estimation of the flow regime based on three dimensionless numbers: (i) the melt pool depth-to-radius aspect ratio $A = D/L$, (ii) the Prandtl number Pr and (iii) a dimensionless number N inversely proportional to the Marangoni number Ma:

$$N = \left(\mu \Big/ \left(\rho \left| \frac{\partial \gamma}{\partial T} \right| \frac{\eta P}{\mu \pi \lambda} \right) \right)^{1/3} \tag{5.1}$$

For the Pitscheneder experiment (see Tab.5.1 for material properties) at a welding power of 5200 W and a sulfur concentration of 150 ppm, the values of those dimensionless numbers are $A \approx 1.5$, $Pr = 0.178$ and $N \approx 0.01$.

According to the analysis by Chakraborty and Chakraborty [156]:
(i) convection starts to play a major role in the transport of thermal energy when $Pr \geq O(N^2 A^{-8/3})$. With $O(N^2 A^{-8/3}) \approx 3 \cdot 10^{-5}$ this is certainly the case here;
(ii) The onset of turbulence is expected for $2A^{2/3}N^{-2} \geq O(Re_{crit})$, where Re_{crit} is estimated from experiments to be around 600 [41, 156]. Here, $2A^{2/3}N^{-2} \simeq 2.6 \cdot 10^4$, which is a strong indication for the flow to be turbulent;
(iii) Turbulent thermal diffusion is predicted to exceed molecular thermal diffusion when $Pr \geq O(25N^2 A^{-2/3})$. With $25N^2 A^{-2/3} \simeq 2 \cdot 10^{-3}$ this is indeed expected to be the case here.

Now that we have established a need to investigate the possibility of turbulent flow and heat transport in melt pools, we will use simulations with very high temporal and spatial resolution to investigate the significance of turbulence without having to resort to questionable modelling techniques. To date, no such simulation results of welding have been published, as even with access to supercomputing facilities the computational cost remains substantial for long welding times. The conduction-mode laser welding experiments by Pitscheneder et al. [89] will be used as an attractive test case for the hypothesis of the occurrence of turbulence, as uncertainties in boundary conditions are minimized while still exhibiting the need for significantly enhanced transport coefficients in laminar simulations in order to match the experimental results.

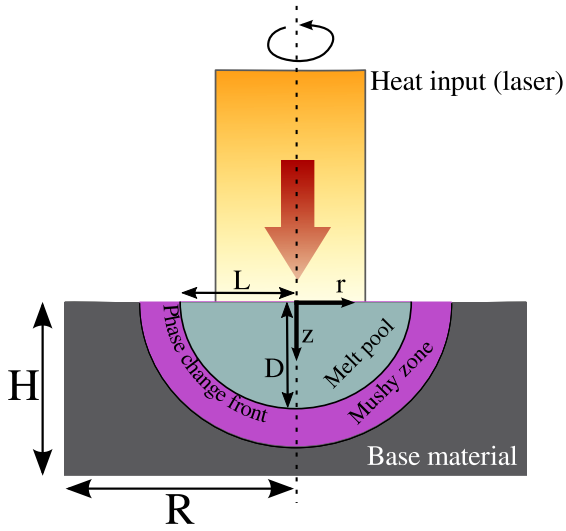

Figure 5.1.: Schematic representation of the studied laser welding.

5.2. Model formulation

5.2.1. Governing equations

A schematic of a typical weld is shown in Fig.5.1, where a slab of metal is targeted by a high power laser. The laser irradiation will be absorbed by the target material, leading to an increase in temperature and eventually a melting phase change. Heat will be transferred into the bulk of the welded material by conduction and thermo-capillary driven convection. These phenomena are mathematically modeled with an energy transport equation with a source term for the latent heat of the phase change

$$\frac{D}{Dt}(\rho c_p T) = \nabla \cdot (\lambda \nabla T) + S_{latent} \tag{5.2}$$

Due to the non-uniform heating of the top surface, large temperature gradients will develop. These temperature gradients result in gradients in surface tension, leading to thermocapillary forces along the non-deformable liquid-gas interface driving flow in the melt pool. The momentum transport is described by the Navier-Stokes equations, with a momentum sink that models the friction in the so-called mushy zone, where the liquid and solid phase co-exist

$$\frac{D}{Dt}\vec{U} = -\frac{1}{\rho}\nabla p + \nabla \cdot (\nu \nabla \vec{U}) - \vec{F}_{damp} \tag{5.3}$$

Here, we have assumed constant density over all phases.

5.2.1.1. Latent heat release

The effect of melting and solidification on the heat transfer are taken into account via the source term S_{latent} in equation 5.2

$$S_{latent} = \rho h_f \frac{dg}{dt} \tag{5.4}$$

with h_f the latent heat of fusion and g the volume fraction of solid material, which is assumed to vary linearly over the melting temperature range between solidus and liquidus

$$g = \frac{T_l - T}{T_l - T_s},\ T_s < T < T_l \tag{5.5}$$

5.2.1.2. Coupling of momentum and heat transport

Through the inclusion of the momentum sink term, the momentum equation 5.3 is valid for the entire domain including both liquid and solid regions. The (semi-)solid regions are modeled as a porous medium, introducing a momentum sink following the isotropic Blake-Kozeny model [52]

$$\vec{F}_{damp} = \frac{\mu}{\rho K}\vec{U} \tag{5.6}$$

$$K = K_0 \frac{(1-g)^3}{g^2 + \varepsilon} \tag{5.7}$$

with $\mu / K_0 = 10^6\,\mathrm{N\,s\,m^{-4}}$ and $\varepsilon = 10^{-3}$.

5.2.2. Boundary conditions

For 2D simulations we assume the melt pool to be axisymmetrical and make use of this by only simulating a wedge of the domain. Circumferential gradients are zero on the wedge faces. The conditions on the remaining boundaries (which are the same in 2D and 3D) are outlined in the following.

5.2.2.1. Heat input

At the top surface, the laser irradiation is modeled by a top-hat distributed heat flux. Because the heat loss due to radiation and convection is only a small fraction of the laser irradiation, we apply adiabatic boundary conditions everywhere except the irradiated area, where we apply a top-hat distribution as

$$\lambda \nabla_n T\Big|_{z=0} = \frac{\eta P}{\pi r_q^2},\ r \leq r_q \tag{5.8}$$

Here we follow Pitscheneder et al. [89] with $\eta = 0.13$, $P = 5200\,\mathrm{W}$ and $r_q = 1.4\,\mathrm{mm}$.

5.2.2.2. Momentum

At the liquid-gas interface, we introduce a shear stress in the liquid due to surface tension gradients along the interface (Marangoni force):

$$\mu \nabla_n U_t\Big|_{z=0} = \frac{d\gamma}{dT} \nabla_t T \tag{5.9}$$

The variation of surface tension with temperature is computed using the thermo-chemical model of Sahoo et al. [32]. The relevant curve for a sulfur concentration of 150 ppm is plotted in Fig. 5.2. At all other surfaces, we set the velocity to zero.

5.3. Numerical procedure

Our solver is built on top of the open source finite volume framework OpenFOAM (version 2.1.x) [118].

We use a 2nd order backward differencing time marching scheme, and a 2nd order TVD scheme (limitedLinear [157]) for the divergence terms. At every time step, the non-linearity associated with the pressure-velocity-coupling is handled by the iterative PISO algorithm [120]. Once a divergence free velocity field has been computed at a given time step, the energy transport equation (5.2) is solved. If a phase change occurs, the temperature equation will be non-linear. The non-linearity due to latent heat is dealt with using an implicit source term linearization technique [83].[‡]

To properly resolve the turbulent structures in space and time using direct numerical simulations, we estimate the length and time scales of the smallest turbulent eddies

[‡]The solver and input files will be made available through the journal's supplementary material.

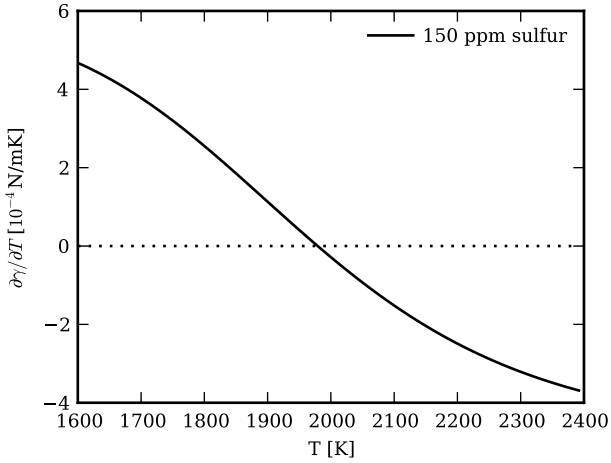

Figure 5.2.: Surface tension temperature coefficient

Table 5.1.: Material properties of the S705 alloy [89]

Property	Value	Unit
Solidus temperature T_s	1610	K
Liquidus temperature T_l	1620	K
Specific heat capacity c_p	670	$\mathrm{J\,kg^{-1}\,K^{-1}}$
Density ρ	8100	$\mathrm{kg\,m^{-3}}$
Thermal conductivity λ	22.9	$\mathrm{W\,m^{-1}\,K^{-1}}$
Latent heat of fusion h_f	$2.508 \cdot 10^5$	$\mathrm{J\,kg^{-1}}$
Viscosity μ	$6 \cdot 10^{-3}$	Pa s
Surface tension temperature coefficient $\partial\gamma/\partial T$	$-5.0 \cdot 10^{-4}$	$\mathrm{N\,m^{-1}\,K^{-1}}$
Entropy factor	$3.18 \cdot 10^{-3}$	–
Heat of adsorption	$-1.66 \cdot 10^8$	$\mathrm{J\,kg^{-1}}$
Surface excess at saturation	$1.3 \cdot 10^{-8}$	$\mathrm{kmol\,m^{-2}}$

(Kolmogorov scales), which depend on a characteristic velocity and a characteristic length scale. Anticipating the simulation results presented in the next section, and looking at the experimental and numerical results reported by Pitscheneder et al. [89], we estimate a characteristic velocity $U_s \approx 0.2\,\mathrm{m\,s^{-1}}$, and a characteristic length scale of $2L \approx 4 \times 10^{-3}\,\mathrm{m}$. Now with the turbulent kinetic energy dissipation rate $\epsilon \approx U_s^3/D$, the Kolmogorov length scale is estimated by

$$L_K = \left(\frac{\nu^3}{\epsilon}\right)^{1/4} = \left(\frac{D\nu^3}{U_s^3}\right)^{1/4} \approx 2 \times 10^{-5}\,\mathrm{m} \tag{5.10}$$

The Kolmogorov time scale is given by

$$t_K = \left(\frac{\nu}{\epsilon}\right)^{1/2} \approx 6 \times 10^{-4}\,\mathrm{s} \tag{5.11}$$

The solution domain is a cylinder of radius $R = 7.5\,\mathrm{mm}$ and height $H = 7.5\,\mathrm{mm}$, discretized with a mesh of 4.8 million cubic control volumes. The area where we expect fluid flow consists of small cubes with a a cell spacing of 23 µm, whereas we use larger cells of 188 µm away from the liquid region. The mesh is shown in Fig.5.3. The time step is dynamically set obeying a maximum Courant number of $Co = U\Delta t/\Delta x < 0.33$, resulting in a typical time step of less than $1 \times 10^{-5}\,\mathrm{s}$.

To further demonstrate the sufficient resolution of our mesh for proper direct numerical simulation (DNS), anticipating the simulation results presented in the next section, we determine the distribution of the turbulence dissipation rate in the simulated flow as $\epsilon = \nu\overline{\nabla U'} : \overline{\nabla U'}$, with the computed velocity fluctuations $U' = U - \overline{U}$. The ratio of the mesh spacing Δx and the smallest turbulence length scales L_K, based on the simulated velocity and dissipation averaged over a time of 0.5 s, is plotted in Fig.5.4 for a slice through the pool, showing excellent resolution of even the smallest scales in our simulations. Only a very small region near the stagnation point at the surface, consisting of few mesh cells, is under-resolved by a factor up to 4.

5.4. Results and Discussion

5.4.1. Validation with enhanced transport coefficients

In order to obtain good agreement between their numerically simulated melt pool shapes and experimentally observed post-solidification weld shapes, Pitscheneder et al. [89] artificially enhance the viscosity and thermal conductivity of the welded steel by a non-elucidated constant factor 7. We can reproduce their result using

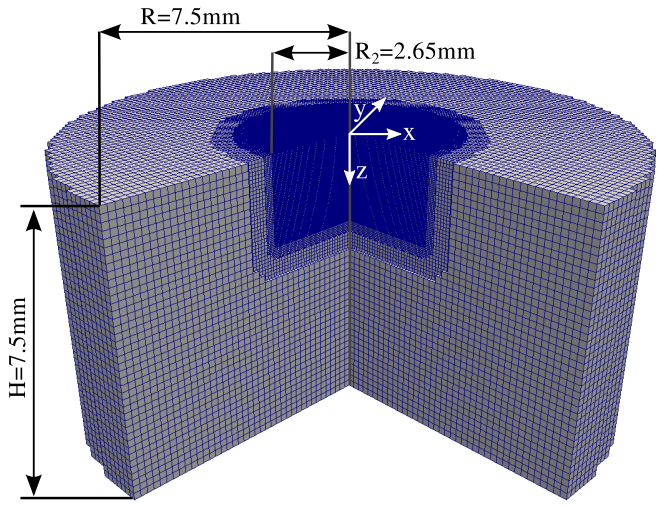

Figure 5.3.: 3D mesh, where one quarter of the domain has been clipped for visualization. The coarse outer mesh with a grid cell size of 188 µm is refined in three steps to the finest inner mesh with a grid cell size of 23 µm. The latter is too fine to be resolved in this figure.

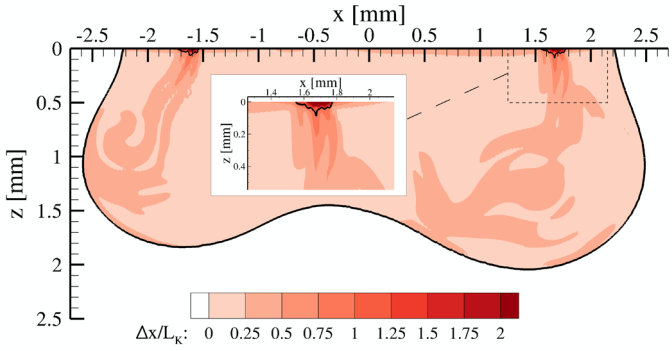

Figure 5.4.: Grid size to turbulent length scale ratio $\Delta x / L_K$ in the in the y=0 mm plane, with the dissipation ϵ averaged over a time of 0.5 seconds. A length scale ratio smaller than 1 means turbulence is perfectly resolved, which is the case everywhere except a small region near the stagnation point at the surface (separated by a black line, with a maximum value of 4).

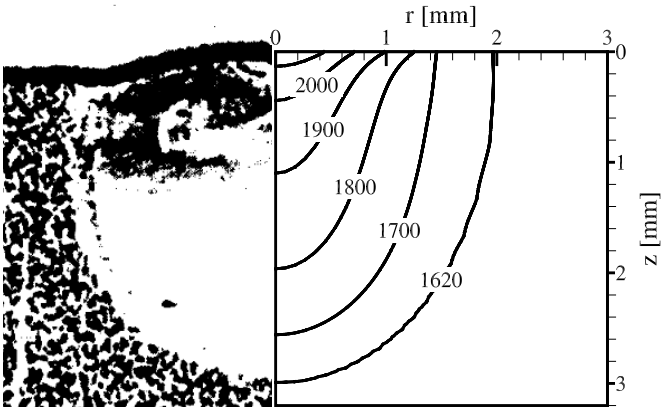

Figure 5.5.: The right hand side of the figure shows the current faithful representation of the experimental result (left half of the figure, reproduced from [89]) after 5 s of welding, using an enhancement factor of 7 for both the viscosity and the thermal conductivity. Temperature isolines in Kelvin (simulation result, right half).

this constant enhancement factor, when, as done by Pitscheneder et al., we use a coarse 2D-axisymmetric grid[§], relatively large time steps, and a diffusive upwind discretization scheme (see Fig. 5.5). Without artificially increasing the transport coefficients, i.e. when using physically realistic values for the viscosity and the thermal conductivity, the flow within the melt pool differs significantly and so does the obtained final weld pool shape, as we will show in the following section.

5.4.2. Direct numerical simulations without enhancement of transport properties

The melt pool shape after 5.00 s of heat input, obtained from fully resolved three-dimensional direct numerical simulations with realistic (non-enhanced) transport properties, is shown in Fig. 5.6. Also shown are melt pool shape snapshots after 4.27 s and 4.70 s of heat input. Compared to the results obtained with enhanced transport coefficients and a diffusive numerical scheme on a coarse 2D mesh, as shown in Fig. 5.5, it is now clearly visible that (i) the flow has not remained symmetric, leading to an asymmetric melt pool shape at this time instance; (ii) the melt pool is a bit wider and much less deep, leading to a pool depth-to-radius aspect ratio which is

[§]Strongly refined towards the free surface and pool centre, with the smallest $\Delta r = 90\,\mu\text{m}$ and $\Delta z = 12\,\mu\text{m}$

now smaller than 1; (iii) The melt pool shape is now strongly time dependent and oscillating.

These observations may be understood as follows: Due to the low (i.e. non-enhanced) molecular thermal conductivity, higher temperatures are now sustained at the melt pool surface, which lead to a large region subject to a negative surface tension gradient, in place of the previously dominant positive surface tension gradient (Fig.5.2). The latter caused a flow directed inward along the pool surface, and towards the pool bottom along its axis, resulting in a deep, hemispherical pool shape as shown in Fig.5.5. The sign change in the surface tension gradient now leads to a surface flow directed radially outward from the pool centre, rather than the inward directed flow in the 2D simulation with enhanced transport coefficients. This results in a wide, shallow pool, rather than a deep, narrow pool. At the edge of the melt pool surface, where temperatures are lower, the surface tension gradient is still positive. As a result, the radially outward surface flow from the pool centre impinges onto a second surface flow directed radially inward from the edge of the pool towards the pool centre. At the point where the two opposing flows meet, at a radial distance of roughly 1.5 mm, a circular, downward jet from the pool surface towards the base of the pool is formed. This jet is unstable, as both its origin and its angle oscillate in time. The oscillating, hot, downwardly directed jet transports so much heat away from the surface that the melt pool boundary is continuously melting and re-solidifying, depending on where the jet is facing at a given time instance. This causes the oscillation of the pool boundary, as visible from the overlayed pool shapes at two additional time instances in Fig.5.6. The flow is also strongly three dimensional, with significant, unsteady flow present in the azimuthal direction (Fig.5.7). The flow pattern and vorticity ω at various time instances around $t = 3.0\,\mathrm{s}$, roughly 0.01 s apart, is shown in Fig.5.8. During these time instances the right jet oscillates back and forth, whereas the left jet is relatively stable. This is of course not true for all time instances, highlighting the chaotic nature of the independent motion of the two jets.

The melt pool flow instabilities are also visible in the temperatures at the pool surface, shown in Fig.5.9. The oscillations are most apparent in the centre of the pool where the oscillation frequency is high, but also at the rim of the pool with a lower frequency due to the dampening effect of melting and re-solidification.

At the stagnation line, where the radially outward surface flow from the pool centre impinges on the radially inward surface flow from the pool edge and where there is a sign change in the surface tension coefficient, very high thermal gradients of $\mathrm{O}(3000\,\mathrm{K\,mm^{-1}})$ occur. Since the thermocapillary force is proportional to these thermal gradients, this is also where we encounter the highest flow velocities (Fig.5.10), locally as high as $2\,\mathrm{m\,s^{-1}}$.

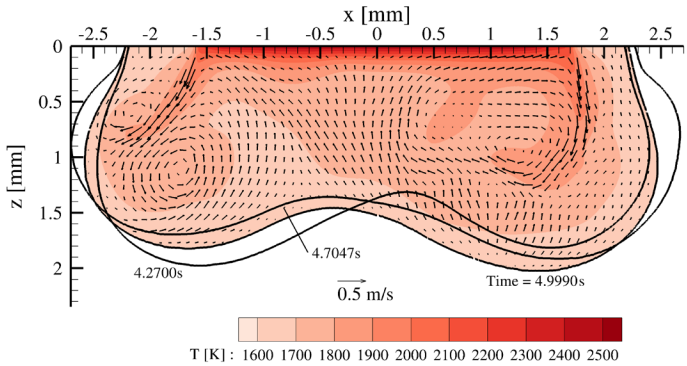

Figure 5.6.: Melt pool shape, temperatures (in Kelvin) and velocity vectors in the y=0 mm plane at the end of heating $t = 5.0$ s. Note that the velocity vectors have been interpolated to a coarse grid in post-processing for clarity. The pool shape at two other time instances is overlayed, showing the pool boundary oscillation.

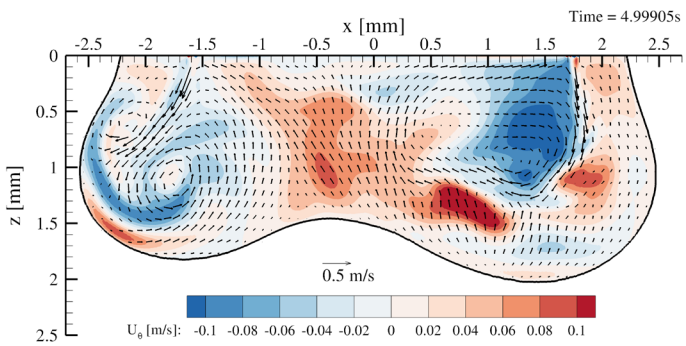

Figure 5.7.: In-plane (x,z) velocities in the y=0 mm plane at $t = 5.0$ s indicated by vectors, and out-of-plane (azimuthal) velocities indicated by colour contours.

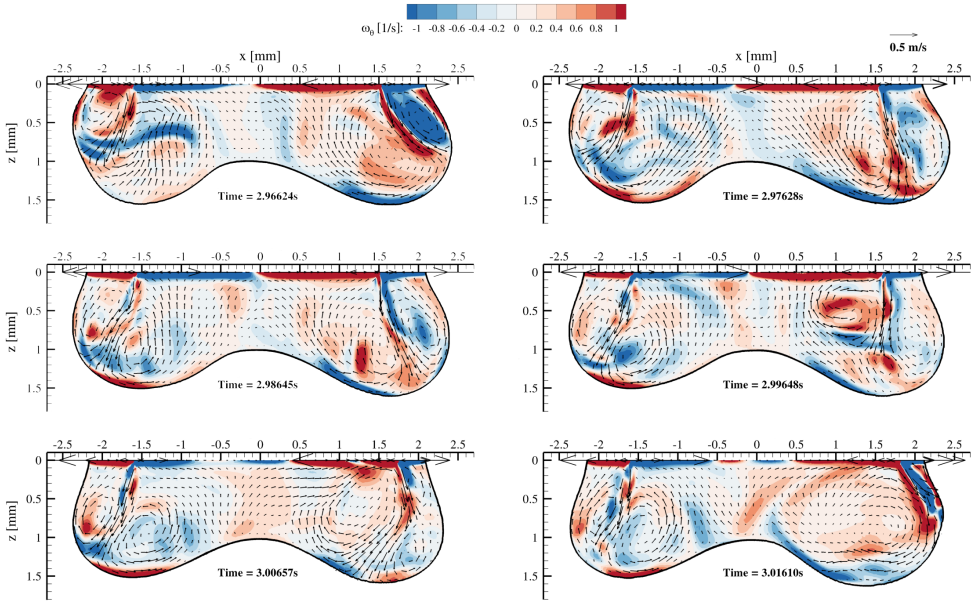

Figure 5.8.: In-plane (x,z) velocity vectors in the y=0 mm plane at a few time instances around $t = 3.0$ s (approximately 0.01 s apart), and out-of-plane vorticity contours.

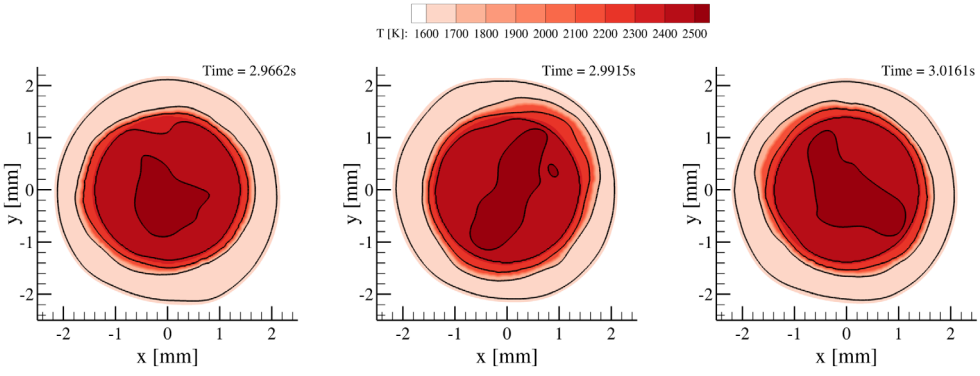

Figure 5.9.: Pool surface (z=0 mm) temperatures in Kelvin at three time instances, top view. Isolines are drawn at 1620K, 1700K, 2200K, 2400K and 2500K (from outside to inside).

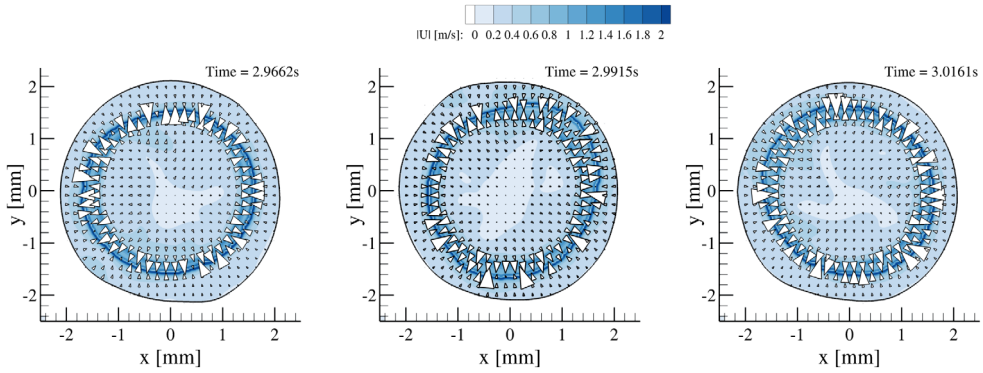

Figure 5.10.: Pool surface (z=0 mm) flow at three time instances, top view. The largest vectors in the vicinity of the stagnation point have been blanked for clarity.

5.4.3. Analysis of turbulent flow properties

We now address a more quantitative analysis of the turbulent nature of the melt pool flow, and the importance of turbulent heat transfer.

Using the computed instantaneous velocity fluctuations $U' = U - \bar{U}$, we can determine the turbulent kinetic energy $k = \overline{U' \cdot U'}/2$, and the turbulent viscosity as $\nu_t = 0.09k^2/\epsilon$, with the turbulent kinetic energy dissipation rate $\epsilon = \nu\overline{\nabla U' : \nabla U'}$. Here, all averages have been computed over the time interval between 4.5 and 5s. The results are shown in Fig.5.11 and Fig.5.12, respectively. The turbulent kinetic energy takes its highest values near the extreme positions of the jet and near the stagnation point at the free surface. The turbulent viscosity assumes its largest values of roughly 50 times the molecular value in an area around the end point of the jet. The space averaged value of the turbulent viscosity is approximately 7.4 times the molecular value. This, coincidentally, is close to the factor 7 enhancement for the transport properties used by Pitscheneder et al. [89] to match their experimental results. However, the uniform enhancement used by Pitscheneder et al. leads to distinctly different melt pool shapes than the turbulent enhancement following from our DNS simulations. In the first, a hemispherical melt pool shape is obtained which is deepest at the centre, whereas the maximum turbulent enhancement occurs in the oscillating jet regions and causes the pool to be wider and deeper at the edges.

To further quantitatively investigate the oscillating flow, we track a monitoring point at a distance of x=1 mm and a depth of z=1 mm from the centre of the pool surface. The temperature history at this monitoring point is shown in Fig. 5.13a. After reaching a quasi steady state, it shows an irregular oscillation with an amplitude of about 200 K around a mean temperature of 1720 K. The velocity magnitude at the monitoring point (Fig. 5.13b) oscillates violently with an amplitudes of roughly 50% of its mean value.

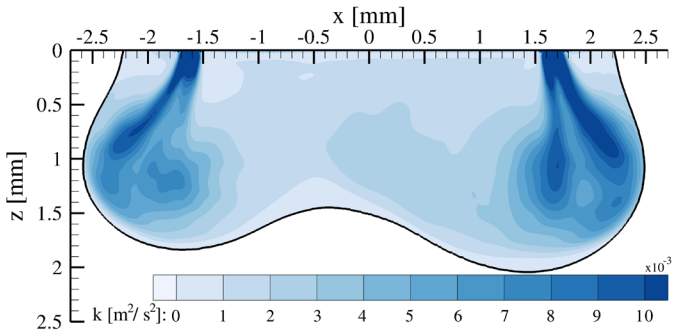

Figure 5.11.: Turbulent kinetic energy k in the y=0 mm plane, averaged over 0.5 s.

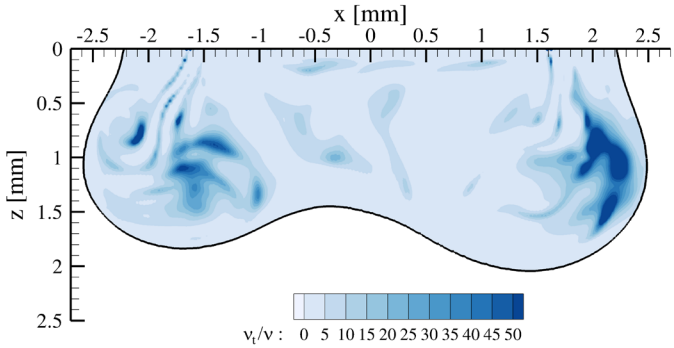

Figure 5.12.: Ratio of turbulent diffusivity over molecular diffusivity ν_t/ν in the y=0 mm plane, based on turbulent kinetic energy and turbulence dissipation averaged over 0.5 s.

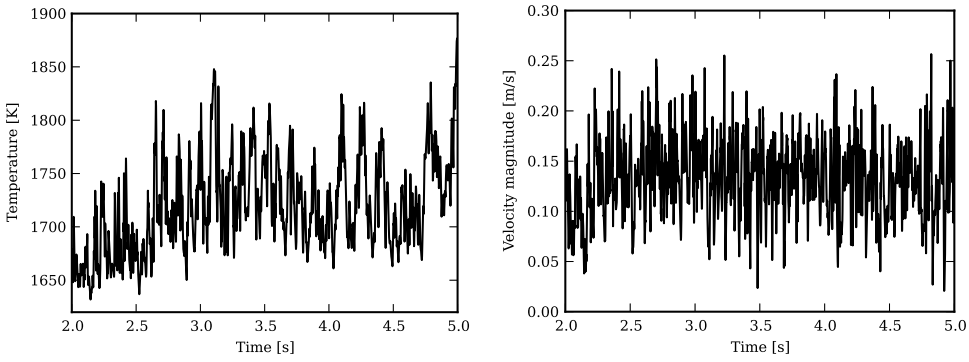

(a) Temperature at monitoring point. **(b)** Total velocity magnitude at monitoring point.

Figure 5.13.: Temperature and velocity magnitude at monitoring location x=1 mm, y=0 mm, z=1 mm

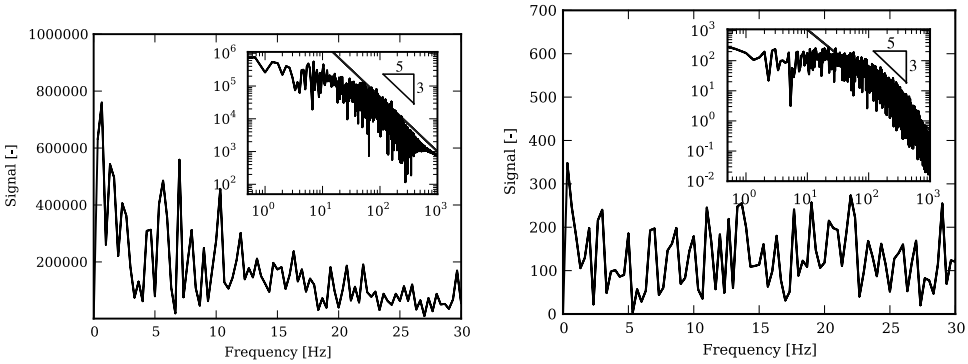

(a) DFT of temperature at monitoring point **(b)** DFT of velocity magnitude at monitoring point

Figure 5.14.: DFT of temperature and velocity magnitude at monitoring point x=1 mm, y=0 mm, z=1 mm. Inserts on log-log scale, in which, as a reference, a blue line with -5/3 slope is shown.

The frequency spectrum of the temperature and velocity magnitude signals at the monitoring point, obtained by a discrete Fourier transform (DFT) of the signals for the quasi steady state period between 2 and 5 seconds after the onset of heating, is shown in figures 5.14a and 5.14b, respectively. Both spectra exhibit multiple peaks in the low-frequency region up to 10 Hz. Due to the low Prandtl number of the fluid, momentum diffusivity is small compared to thermal diffusivity. As a result, high frequency oscillations are more strongly damped for temperature as compared to velocity. The temperature signal drops beyond 10 Hz, whereas the velocity signal only starts dropping around 30 Hz. The most dominant frequencies in the temperature spectrum are around 5, 7 and 11 Hertz, which also appear in the spectrum of the velocity magnitude, though accompanied here by many other peaks up to 30 Hertz.

5.4.4. The 3D nature of the flow instabilities

To unravel to which extent the complexity and oscillating instability of the melt pool flow is related to its three-dimensionality, we have also performed a high-fidelity two-dimensional axisymmetric simulation with a mesh that was very similar to that of the 3D simulations, and identical numerical schemes. The 2D simulated flow, unlike earlier published 2D flow simulations with enhanced transport coefficients on coarse meshes with diffusive numerical schemes, exhibits a highly unstable nature, very similar to that observed in the 3D simulations. A characteristic flow oscillation is shown in Fig. 5.15. The, now axisymmetric, circular downward jet stemming from the stagnation point at the free surface shows qualitatively the same oscillatory pattern as observed in the 3D simulations. It may therefore be concluded that the additional degree of freedom of three-dimensionality is not a requirement for triggering the jet instability. However, in the 2D case the oscillation is much more regular, which can easily be observed from the temperature signal at the monitoring point (Fig. 5.15). While the amplitude of the oscillation of roughly 250 K is even larger than in the 3D flow, the oscillation frequency is low and regular, with large peaks in the spectrum reoccurring at roughly 4 Hz.

A similar oscillation pattern has been reported in literature for the case of a slot jet impinging on a concave curved wall [158]. However, in the presently studied melt pool flow, at least in 2D, the instability appears not to be simply due to the interaction between the impinging jet and the concave bottom of the pool, but stems from a more complex interplay between the jet, its oscillating origin, and the constantly deforming melt pool bottom due to melting and re-solidification. We performed a 2D axisymmetric simulation in which, after a quasi steady-state with strong jet oscillations had been reached, further melting (and re-solidification) of the pool boundary was prevented by artificially increasing the latent heat of melting by a factor 100, thus de facto fixing the pool boundary. With this fixed pool boundary, the jet oscillations quickly died out and the flow became steady-state. This demonstrates that, at least in 2D, the interplay with a deforming melt pool boundary is necessary to sustain the jet oscillations. The same fixation of the pool boundary in 3D did not

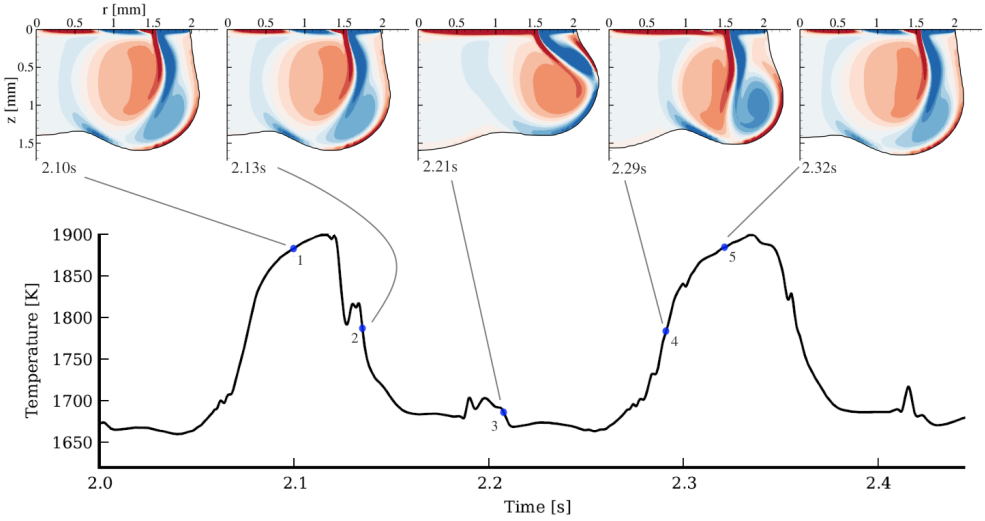

Figure 5.15.: Two-dimensional flow vorticity at various time instances in the axisymmetric case, with corresponding temperature probe at a monitoring point at r=1mm, z=1mm

lead to a suppression of the oscillations, indicating that the 3D case is more prone to instabilities than the 2D case.

5.5. Conclusion and outlook

We have simulated the liquid metal flow in the melt pool of a conduction-mode laser weld, using high-fidelity direct-numerical-simulations to gain insight into flow instabilities that have been reported in experimental studies, but not in numerical studies to date.

In our simulations, unlike earlier numerical studies that used coarse meshes, diffusive numerical schemes and enhanced transport coefficients, we observe self-sustained flow instabilities. These arise even in the absence of a deformable liquid-gas surface, temperature dependent material properties, or non-uniform surfactant concentrations. The instabilities even occur when restricting the flow to axial symmetry, albeit the oscillation is much more regular in that case.

The amplitude and frequency spectrum of the temperature and velocity oscillations support the argument of enhanced heat and momentum transport due to turbulent flow in the melt pool. Averaged in space, the turbulent diffusivities are approximately seven times higher than their molecular values. This turbulent transport

enhancement is of the same order of magnitude as ad-hoc enhancement factors commonly used in previous studies to obtain agreement between numerical weld pool simulations and experimentally observed weld pool shapes. However, the observed turbulent enhancement is strongly non-uniform, and highest in the regions of the oscillating jets near the rim of the weld pool. Therefore, unlike in simulations assuming uniform transport enhancement and unlike experimentally observed for this case, our simulations lead to W-shaped melt pools that are deepest near the rim of the pool.

Thus, while we have clearly demonstrated the presence of turbulent flow instabilities and turbulent transport enhancement in laser weld pools, the predicted turbulence does not lead to proper melt pool shape predictions. We believe the most likely deficiency of our model to be in the assumed uniform surfactant concentration due to the lack of a mass transport model for surfactant species. Winkler et al. [136] have demonstrated that surfactant concentrations may actually be highly non-uniform, leading to strong alterations of the Marangoni forces and flow. Hence, combining the results from Winkler et al. [136] with the present results, direct numerical or dynamic large eddy turbulence simulations coupled with a mass transport model for the surfactants are probably needed to move forward towards really predictive melt pool models for welding.

6. The influence of surfactants on thermocapillary flow instabilities in low Prandtl melting pools*

Flows in low Prandtl number liquid pools are relevant for various technical applications, and have so far only been investigated for the case of pure fluids, i.e. with a constant, negative surface tension temperature coefficient $\partial\gamma/\partial T$. Real-world fluids containing surfactants have a temperature dependent $\partial\gamma/\partial T > 0$, which may change sign to $\partial\gamma/\partial T < 0$ at a critical temperature T_c. Where thermocapillary forces are the main driving force, this can have a tremendous effect on the resulting flow patterns and the associated heat transfer.

Here we investigate the stability of such flows for five Marangoni numbers in the range of $2.1 \times 10^6 \leq Ma \leq 3.4 \times 10^7$ using dynamic large eddy simulations (LES), which we validate against a high resolution direct numerical simulation (DNS). We find that the five cases span all flow regimes, i.e. stable laminar flow at $Ma \leq 2.1 \times 10^6$, transitional flow with rotational instabilities at $Ma = 2.8 \times 10^6$ and $Ma = 4.6 \times 10^6$ and turbulent flow at $Ma = 1.8 \times 10^7$ and $Ma = 3.4 \times 10^7$.

6.1. Introduction

Flows in heated liquid pools with a free surface are of interest in various technical applications, such as metals processing including fusion welding, electron beam evaporation, casting and crystal growth. In these processes, low Prandtl number liquids are subjected to large surface temperature gradients, which, through resulting gradients in surface tension γ, lead to thermocapillary motion of the liquid. In spite of the relevance of low Prandtl number liquids, most research has been devoted to high Prandtl number liquids such as silicone oils [159], as these are easy to work with experimentally and resistant to contamination which can have a major effect on the flow. Where instabilities in low Prandtl number liquids have been investigated, it has been done for pure materials, i.e. with a constant, negative surface tension temperature coefficient $\partial\gamma/\partial T$, in various geometric configurations (e.g. rectangular [160–162], liquid bridges [163–165], annular [166] or cylindrical [167]).

*The contents of this chapter have been published in the journal Physics of Fluids 28(6) (June 2016), doi:10.1063/1.4953797

However, real-world applications often involve (i) non-pure materials, i.e. materials containing surface active elements (surfactants), and (ii) melting/solidification phase change, both of which influence the thermocapillary flow. The presence of surfactants, even when homogeneously distributed, can have a tremendous effect on the thermocapillary motion by introducing a temperature dependence of the surface tension temperature coefficient $\partial\gamma/\partial T$. Even traces of surfactants such as sulfur or oxygen can be sufficient to introduce a sign change from positive to negative $\partial\gamma/\partial T$ at a critical temperature T_c in many materials [32, 168], such as iron, silver, copper or nickel.

The stability of thermocapillary flows in such non-pure low Prandtl number liquids has not been thoroughly studied. Azami et al. [169] used X-ray tomography to probe the flow of liquid silicon in a half-zone liquid bridge subject to a controlled atmosphere containing varying concentrations of oxygen, which is surface active in silicon and many other liquid metals. They found the flow to be chaotic for low oxygen partial pressures, and to stabilize when the partial pressure is increased above a certain threshold. Here, the oxygen, after adsorption to the silicon, alters the value of $\partial\gamma/\partial T$, which however remains negative and may be regarded as constant, as the applied temperature difference is fairly low. Zhao et al., using particle image velocimetry (PIV) to image the movement of oxide particles floating on the free surface, examined the thermocapillary flow in liquid steel melt pool, heated by a translating electric arc [134] or a stationary laser [170]. For the translating arc, where the surfactant was present as an oxide layer on the surface, they observed an elliptic pool shape subject to periodic non-symmetric oscillations of the surface flow. For stationary laser heating, where oxygen was introduced through a controlled atmosphere, they observed a circular melt pool in which the surface flow was asymmetric and rotational. Kou et al. [171], using qualitative video analysis of the surface of steel melts with sulfur impurities, observe free surface oscillations, indicating instationary flow phenomena. Previous numerical studies of thermocapillary flows taking into account the presence of surfactants and phase change, e.g. Winkler and Amberg [137] and Do-Quang et al. [172], fail to report instabilities observed in the aforementioned experiments, probably due to imposed symmetry and the use of diffusive numerical schemes.

The available literature on the instability of low Prandtl number thermocapillary flows with surfactants is thus exclusively experimental, and rather qualitative. We aim to improve the understanding of instabilities arising in such flows by providing insight into the flow in the pool, addressing the possible occurrence of flow instabilities and turbulence. Specifically, we will investigate thermocapillary flows with non-uniform axisymmetric heating at the free surface such that a negative radial temperature gradient dT/dr develops across the free surface.

For pure low Prandtl fluids with constant, negative $\partial\gamma/\partial T$ in such cylindrical domains, the onset of oscillatory and turbulent convection is already well understood. Pumir and Blumenfeld [37] derived scaling laws for the dimensionless heat transport assuming laminar ($Nu \sim Ma^{1/4}Pr^{1/2}$) or turbulent ($Nu \sim Ma^{1/3}Pr^{1/3}$) thermo-

capillary flow. Here, the Marangoni number is defined as $Ma = \partial\gamma/\partial T P(\rho\nu\alpha\lambda)^{-1}$, with P, ρ, ν, α, λ the absorbed power, and the fluid density, kinematic viscosity, thermal diffusivity and thermal conductivity, respectively. Karcher et al. [173] experimentally investigated the flow of liquid iron ($Pr \approx 0.1$) in a vacuum, heated by a high-power electron beam up to 50 kW. At Marangoni numbers between 10^7 and 10^8 they find turbulent convection, indicated by a $Nu \sim Ma^{1/3}$ scaling behavior of the dimensionless heat transfer[37]. Dikshit et al. [174] experimentally observed a scaling between the laminar and turbulent behavior at Marangoni numbers between 10^4 and 10^5. Boeck and Karcher [175] studied a similar electron beam heating process for a $Pr = 0.1$ fluid via three dimensional direct numerical simulations. They find a transition from stationary to oscillatory convection around $Ma \approx 2 \times 10^4$ and eventually chaotic flow above $Ma \approx 2 \times 10^5$, and good agreement with scaling laws derived by Pumir and Blumenfeld [37]. Kuhlmann and Schoisswohl [176] used linear stability analysis to study the occurrence of flow instabilities in thermocapillary liquid pools in cylindrical domains with multiple aspect ratios, heated by a non-uniform heat source. For low Prandtl number fluids above a critical Marangoni number, they find a stationary centrifugal instability driven by inertial effects.

We conduct our study of the flow in a pool of a low Prandtl number liquid with surfactants ($Pr = \mathcal{O}(10^{-1})$) with a non-uniform heat-flux at the free surface using dynamic large eddy simulations (LES). The well-resolved large eddy simulations are validated using a high resolution direct numerical simulation (DNS). We will provide a novel insight into the flow inside the liquid pool and investigate the occurrence of flow instabilities and turbulence over a range of Marangoni numbers.

6.2. Mathematical Model

6.2.1. Governing equations

We investigate a solid cylinder of metal targeted on one end by a high power laser. The laser irradiation is absorbed by the metal, leading to an increase in temperature and eventually a melting phase change and the creation of a liquid melt pool. Heat is transferred into the solid bulk of the material by conduction and thermocapillary driven convection (Fig.6.1). This system is mathematically modeled with an energy transport equation with a source term for the latent heat of the phase change

$$\frac{D}{Dt}(T) = \nabla \cdot (\alpha \nabla T) + S_{latent} \tag{6.1}$$

with the thermal diffusivity $\alpha = \lambda/\rho c_p$.

Due to the non-uniform heating of the top surface, large radial surface temperature gradients develop. These result in radial gradients in surface tension, leading

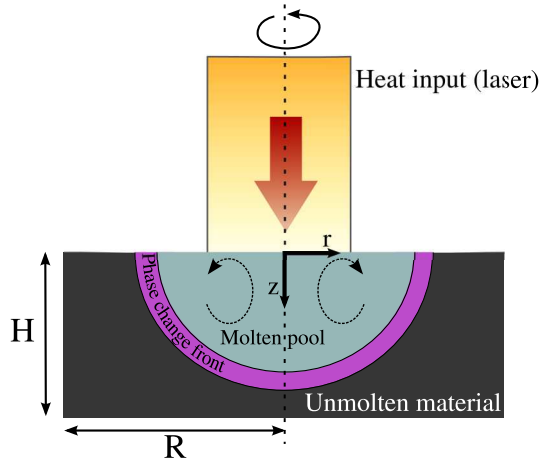

Figure 6.1.: Schematic representation of the studied problem.

to thermocapillary forces along the liquid-gas interface driving flow in the molten pool. The momentum transport is described by the Navier-Stokes equations, with a momentum sink to account for solid and semi-solid regions

$$\frac{D}{Dt}\vec{U} = -\frac{1}{\rho}\nabla p + \nabla \cdot (\nu \nabla \vec{U}) - \vec{F}_{damp} \tag{6.2}$$

Here, we have assumed constant density over all phases, and have neglected buoyancy since the Grashof number $Gr = \mathcal{O}(10^3)$ is small Kuhlmann and Schoisswohl [176]. Furthermore, since surface tension is very strong in liquid metals ($Ca = \mu U/\gamma = \mathcal{O}(10^{-1})$, with $U \sim \Delta\gamma/\mu$), we assume the liquid-gas interface to be undeformable.

The effect of melting and solidification on the heat transfer is taken into account via the source term S_{latent} in equation 6.1,

$$S_{latent} = \frac{h_f}{c_p}\frac{dg}{dt} \tag{6.3}$$

with h_f the specific latent heat of fusion, and g the volume fraction of solid material, which is assumed to vary linearly over the melting temperature range between solidus T_s and liquidus T_l

$$g = \frac{T_l - T}{T_l - T_s},\ T_s < T < T_l \tag{6.4}$$

Through the inclusion of the momentum sink term, the momentum equation 6.2 is valid for the entire domain including liquid, semi-solid and solid regions. The (semi-)solid regions are modeled as a porous medium, introducing a momentum sink following the isotropic Blake-Kozeny model [52]

$$\vec{F}_{damp} = \frac{\mu}{\rho K}\vec{U} = \frac{\vec{U}}{\rho}\frac{\mu}{K_0}\frac{g^2}{(1-g)^3+\varepsilon} \tag{6.5}$$

with $\varepsilon = 10^{-3}$ and K_0 a constant coefficient characterizing the porosity.

6.2.2. Boundary conditions

At the top surface, the laser irradiation is modeled as a top-hat distributed heat flux. Because the heat loss from the outer surfaces of the cylindrical domain to the ambient due to radiation and convection is only a small fraction of the laser irradiation, we apply adiabatic boundary conditions everywhere except the irradiated area, where we apply a top-hat distribution as

$$\lambda \nabla_n T\Big|_{z=0} = \frac{P}{\pi r_q^2},\ r \leq r_q \tag{6.6}$$

Here we set the laser beam radius $r_q = 1.4\,\text{mm}$ and absorbed powers P of 170, 195, 250, 500 and 675 W, to mimic realistic absorbed irradiation relevant for metals processing applications [89].

At all surfaces except the liquid-gas interface, we set the velocity to zero. At the gas-liquid interface, which is assumed to remain flat, we impose a shear stress in the liquid due to surface tension gradients along the interface, known as Marangoni or thermocapillary stress:

$$\mu \nabla_n U_t\Big|_{z=0} = \frac{d\gamma}{dT}\nabla_t T \tag{6.7}$$

The surface tension temperature coefficient $\partial\gamma/\partial T$ has a defining influence on the nature of the flow as it determines the only driving force acting here. As discussed in the introduction, in the present work we wish to study the stability of flows in liquids containing a homogeneously distributed surface active element. The surfactant will react with the liquid metal, significantly reducing the surface tension at the liquid-gas interface. At increasing temperatures, chemical bonds between metal

atoms and surfactant molecules break, and surfactant molecules dissociate. Hence the surface tension increases at increasing temperatures and $\partial\gamma/\partial T$ is positive. At very high temperatures however, after all surfactant molecules have dissociated, the liquid will start to behave as the pure liquid metal and $\partial\gamma/\partial T$ will approach the constant, negative value of the pure liquid metal. The transition between the states is smooth, and there is a critical temperature T_c where $\partial\gamma/\partial T$ changes its sign and the surface tension has a local maximum. The surface tension gradients drive a flow from low to high surface tension areas. In laser heating applications, the maximum temperature will typically be at the center of the beam, decreasing towards its edge. A chemically pure liquid metal would thus have its highest surface tension at the edge of the pool and flow towards that cooler edge. In melts with impurities the surface tension maximum will shift towards the center of the irradiated area, and thus the resulting flow pattern will be different.

A realistic relationship [32, 177] between the surface tension temperature coefficient $\partial\gamma/\partial T$ and temperature for a binary liquid metal – surfactant mixture, as shown in Fig. 6.2, will be used in the simulations:

$$\gamma = \gamma_0 - \partial\gamma/\partial T|_0 (T - T_0) - RT\Gamma_s \ln\left[1 + k_l a_s \exp(\Delta H^0/(RT))\right] \tag{6.8}$$

This relationship, based on the combination of Gibbs and Langmuir adsorption isotherms, has been derived by Sahoo et al. [32] for a binary iron-sulfur system. The shape of the surface tension–temperature curve and thus the system behavior is not specific to the iron-sulfur system, but also applies to e.g. silver [177] and nickel [178] in the presence of oxygen.

6.2.3. Non-dimensional formulation

Using the non-dimensional variables $x^* = x/L$, $t^* = t\alpha/L^2$, $\vec{U}^* = \vec{U}L/\alpha$, $T^* = T/\Delta T$, $p^* = pL^2/\rho\alpha^2$, following Pumir and Blumenfeld [37], and $K^* = L^2K$ the governing equations can be written as

$$\frac{1}{Pr}\left(\frac{\partial\vec{U}^*}{\partial t^*} + \nabla\cdot(\vec{U}^*\vec{U}^*) + \nabla p^*\right) = \nabla^2\vec{U}^* + K^*\vec{U}^* \tag{6.9}$$

$$\frac{\partial T^*}{\partial t^*} + \nabla\cdot(\vec{U}^*T^*) = \nabla^2 T^* + \frac{1}{St}\frac{\partial g}{\partial t^*} \tag{6.10}$$

and the boundary conditions

$$\nabla_n U_t^* = Ma\nabla_t T^* \tag{6.11}$$

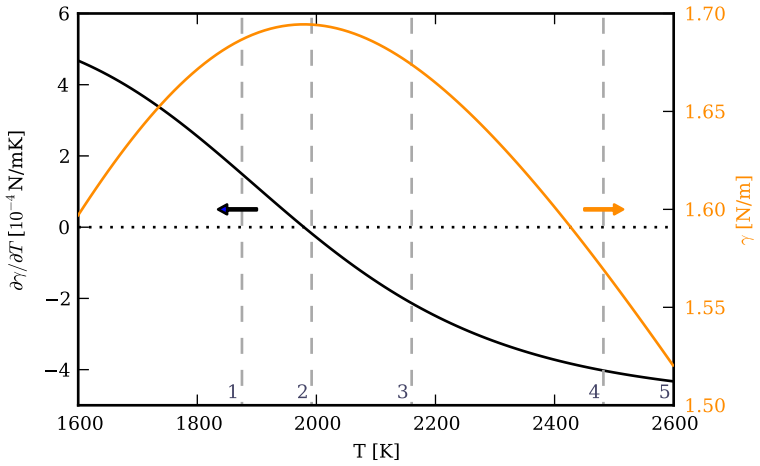

Figure 6.2.: Surface tension temperature coefficient. The critical temperature at which the sign change occurs is $T_c = 1979\,\mathrm{K}$. The vertical dashed lines indicate the maximum surface temperature reached in cases 1-5, as discussed later.

The dimensionless numbers appearing in the governing equations are the Prandtl number $Pr = \nu/\alpha = 0.18$ and the Stefan number $St = c_p \Delta T / h_f$, gauging the ratio of sensible to latent heat. In the following, we will take the laser beam radius r_q as the characteristic length scale L, and $P/(L\lambda)$ as the characteristic temperature difference ΔT. With this, and for constant $\partial\gamma/\partial T$, the Marangoni number $Ma = \partial\gamma/\partial T L \Delta T (\mu\alpha)^{-1}$, i.e. the ratio of surface tension to viscous forces, is commonly defined as

$$Ma = \frac{\partial\gamma}{\partial T}\frac{P}{\mu\alpha\lambda} \tag{6.12}$$

For the present case with varying $\partial\gamma/\partial T$, we linearize $\partial\gamma/\partial T$ around T_c leading to $\partial\gamma/\partial T \sim (\partial^2\gamma/\partial T^2)|_{T_c}\Delta T$ and define Ma as

$$Ma = \left.\frac{\partial^2\gamma}{\partial T^2}\right|_{T_c}\frac{\Delta T^2 L}{\mu\alpha} \sim \left.\frac{\partial^2\gamma}{\partial T^2}\right|_{T_c}\frac{P^2}{\mu\alpha\lambda^2 L}\frac{1}{Nu^2} \tag{6.13}$$

with $\partial^2\gamma/\partial T^2|_{T_c} = 1.38 \times 10^{-6}\,\mathrm{N\,m^{-1}\,K^{-2}}$. The resulting dimensionless numbers are tabulated in Tab.6.1. The relevant material properties are listed in Tab.A.2 in the appendix, sec.A.5. The ratio Ma/Gr is very large indeed, which further justifies neglecting buoyancy forces.

Table 6.1.: Dimensionless numbers

Case	P [W]	Ma	St
1	170	2.1×10^6	4.7
2	195	2.8×10^6	5.3
3	250	4.6×10^6	6.7
4	500	1.8×10^7	13.5
5	675	3.4×10^7	18.3

6.2.4. Discretization

Our solver has been developed using the open source finite volume framework OpenFOAM (version 2.1.x) [118]. The time derivative is discretized with a second order backward differencing scheme. The divergence terms in the transport equations are discretized with the second order limitedLinear(V) TVD scheme [157]. At every time step, the non-linearity associated with the pressure-velocity-coupling is handled by the iterative PISO algorithm [120]. Once a divergence free velocity field has been computed at a given time step, the temperature equation is solved. The non-linearity of the temperature equation due to latent heat is dealt with using an implicit source term linearization technique [83].

The solution domain is a cylinder of radius $R = 7.5\,\text{mm}$ and height $H = 7.5\,\text{mm}$ (see Fig.6.1), discretized with a mesh of 2.15 million cubic control volumes. The region where we expect fluid flow consists of small cubes with a a cell spacing of 31 µm, whereas we use larger cells of 250 µm away from the liquid region. The mesh is shown in Fig.6.3. The time step is dynamically set obeying a maximum Courant number of $Co = U\Delta t/\Delta x < 0.35$, resulting in a typical time step of roughly 15 µs. A simulation on 48 cores (Intel E5-2650 v2) of the LISA compute cluster[†] is completed in roughly four weeks time.

To model turbulence, we use Large Eddy Simulations based on the dynamic Smagorinsky approach [179, 180] as proposed by Lilly [181, 182]. We do not allow for backscatter of energy from the small to large scale, and thus the subgridscale viscosity ν_{SGS} is clipped to zero. The turbulent thermal diffusivity is not determined via the dynamic Smagorinsky approach, but via Reynolds analogy $\alpha_t = \nu_t/Pr_t$, with $Pr_t = 0.4$ [183, 184]. The equations are integrated up in the entire domain without applying wall models to the immersed solid boundary.

[†] `https://surfsara.nl/systems/lisa`

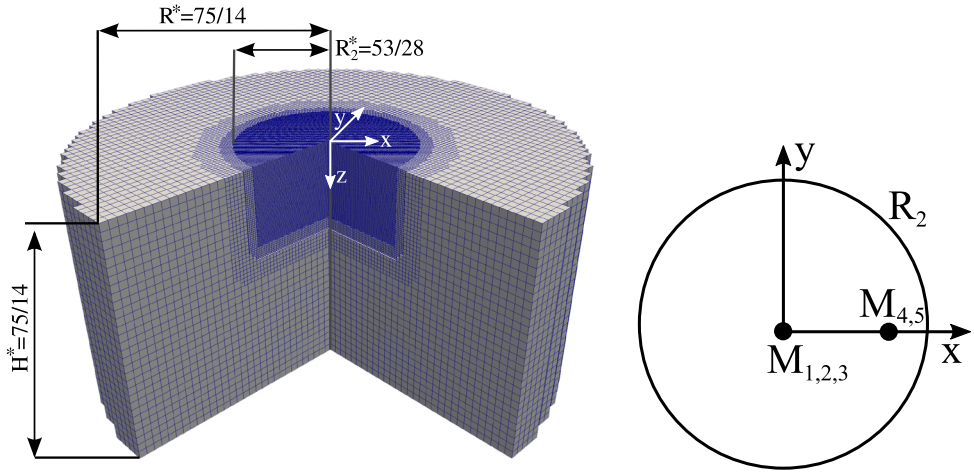

Figure 6.3.: 3D mesh, where one quarter of the domain has been clipped for visualization. The coarse outer mesh with a grid cell size of $\Delta x^* = 0.178$ is refined in three steps to the finest inner mesh with a grid cell size of The latter is too fine to be resolved in this figure. The sketch on the right shows monitoring point locations at a depth of $z^* = 3/14$ and radial distances of $x^* = 0$ ($M_{1,2,3}$) and $x^* = 15/14$ ($M_{4,5}$).

6.3. Results and discussion

The high power laser irradiation melts the target material and within fractions of a second a liquid pool develops. The developing shape of this pool is tightly connected to the thermocapillary flow due to surface tension gradients at the free surface. These surface tension gradients in turn are dependent on the thermal gradients and the local temperature at the free surface itself.

Preceding the discussion of the physics of our results, we present a comparison of temperature data obtained with DNS and LES for validation, as well as the subgridscale viscosity of the LES simulation, to prove the adequate performance of our simulations.

We then present the flow patterns observed on the free surface, similarly to what an experimentalist might see observing the opaque pool from the top using e.g. PIV [170, 185] or PTV methods applied to particles floating on the liquid surface, followed by a discussion of the observations in the next section.

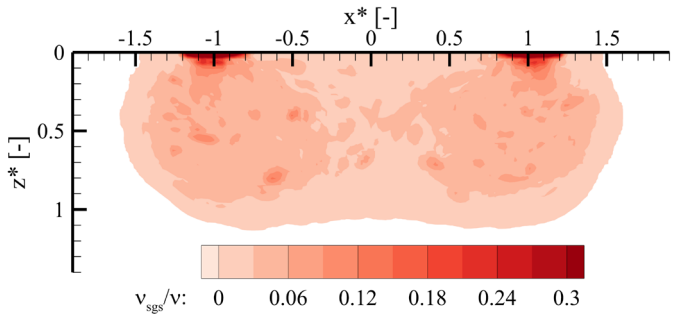

Figure 6.4.: Maximum values of the ratio of subgridscale and molecular diffusivity ν_{SGS}/ν in case 4, proving a well-resolved LES simulation.

6.3.1. Validation of LES

Fig. 6.4 shows the maximum values of ν_{SGS}/ν obtained during the course of a simulation of case 4. The maximum value of the subgridscale turbulent viscosity ν_{SGS} is at most in the order of the molecular viscosity, which indicates a well resolved LES solution. The results obtained for the other cases are not shown here, but are similar or better.

To further validate our results, we have performed a direct numerical simulation for the highest laser power (case 5) on a grid with 21 million cells (14 µm grid spacing). Time averaged temperature profiles over a period of 2 s are shown in Fig. 6.5. We can conclude adequate performance of the dynamic LES solution on a 10x coarser mesh. It is reasonable to expect the solution to be similarly good or better for the other laser powers.

6.3.2. Free surface flow

At the lowest laser power (case 1, Tab. 6.1), the flow is radially symmetric, directed from the rim of the pool towards the center, with the lowest velocities close to the pool rim gradually increasing towards the center of the pool (Fig. 6.6a). The flow is stable, and even when perturbed numerically quickly restores symmetry. With increased laser power (case 2), initially the same flow pattern is observed. At some point in time, the symmetry breaks (Fig. 6.6b), and a stable rotational motion develops near the center of the pool surface. Later on, a high frequency pulsating motion (radial oscillation) is superimposed onto the rotation, which remains very stable nonetheless. The same basic flow topology is observed for case 3, where the flow is again directed from the rim of the pool towards the center, though now the highest velocities are observed close to the pool rim gradually decreasing towards

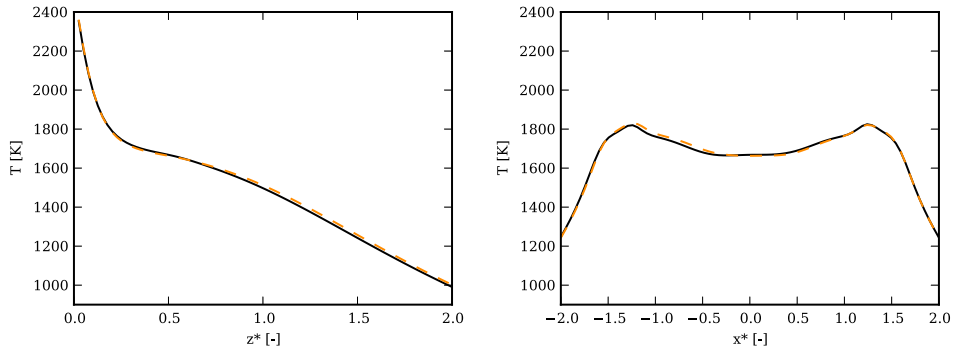

Figure 6.5.: Comparison of temperatures on $x^* = 0$ and $z^* = 0.5$ averaged over the period from 1.5 to 3.5 s, computed by dynamic LES (dashed, 2.5M cell mesh) and DNS (solid, 21M cell mesh).

the center of the pool (Fig. 6.6c). Again, the flow is initially axisymmetric, but very soon becomes asymmetric and unstable. The velocity distribution on the free surface shows a rotational motion. Unlike the results at the lower powers, the rotational motion is not stable and unpredictably changes its direction. For all three cases the pool boundary remains almost perfectly circular, despite any instabilities in the flow.

The numerical experiment at a higher laser power (case 4) exhibits a dramatically different flow pattern (Fig. 6.6d). Here, there is flow from the pool rim towards the pool center, which, after only a short distance from the rim, meets a flow stemming from the pool center towards the rim in a vicinity where the highest velocity magnitudes are encountered. The flow is highly unstable and even the pool boundary is significantly distorted. At the highest laser power (case 5), the flow pattern shown in Fig. 6.6e is similar to the one observed in case 4. Here also an inward flow from the pool rim meets an outward flow from the pool center, leading to a stagnation region fairly close to the pool boundary. In contrast to the previous case, the stagnation region is spread over a wider area, and the pool boundary is not quite as unstable.

6.3.3. Temperature profile on the free surface

The surface flow presented in the previous section is of course driven by surface tension gradients due to non-uniform temperatures at the free surface, and thus a look at the temperature distributions on the free surface is necessary to understand the observations.

At the lowest laser power (case 1, Fig. 6.2), the temperature distribution is radially symmetric with a maximum temperature in the center well below $T_c = 1979\,\mathrm{K}$. The surface force is thus always directed towards the hot pool center. Increasing the

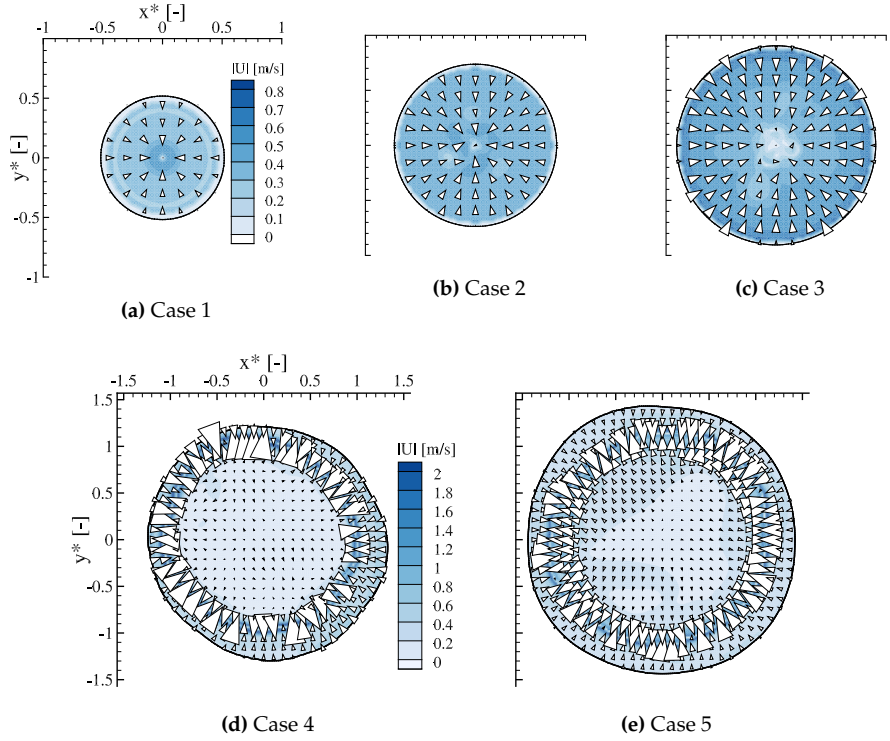

(a) Case 1 **(b)** Case 2 **(c)** Case 3

(d) Case 4 **(e)** Case 5

Figure 6.6.: Free surface flow with velocity vectors and contours of velocity magnitude, at t=2s for increasing laser power.

laser power (case 2), the initially similar symmetric pattern is superseded by first a rotating square (Fig. 6.7a) and then a rotating trefoil pattern (Fig. 6.7b). The rotational instability develops before the maximum temperature at the surface reaches T_c. Once the maximum temperature surpasses T_c, a pulsating motion superimposes the rotation. Higher laser powers are necessary to push the temperature significantly beyond T_c. In case 3, temperatures up to 2300 K, well beyond T_c, are sustained at the free surface in a narrow region near the pool center, while the majority of the free surface temperature remains below T_c. This leads to a sign change in $\partial\gamma/\partial T$ (cf. Fig. 6.2), which explains the flow pattern shown previously (Fig. 6.6c), where the flow directed towards the center of the pool is decelerated by the opposing Marangoni force but not permanently reversed. The strongest Marangoni forces appear close to the pool boundary, due to a combination of the highest thermal gradients and the highest value of $\partial\gamma/\partial T$ in this region. Qualitatively, the surface temperature patterns are similar to case 2 with an initial radially symmetry of the isotherms, which breaks down much sooner compared to case 2. The isotherms in the vicinity the pool center then briefly deform into a square shape, followed by a trefoil shape which rotates with time (Fig. 6.8a). Unlike case 2, the rotation is stable only for short periods, and unpredictably reverses its direction (Fig. 6.8b). A qualitatively similar asymmetrical rotational surface flow has previously been observed in an experimental study of laser melting of steel exposed to surface active oxygen [170, 185].

When the laser power is increased even further, the resulting higher temperatures increases the strength of the Marangoni flow directed towards the pool boundary, and the region with temperatures above T_c is larger. As a result, the flow topology changes because a flow from the pool center to the boundary is now sustainable. For the second largest power, case 4, maximum temperatures of around 2600 K are observed. The outward flow shown earlier in Fig. 6.6d drives heat from the pool center towards the pool boundary. As a result, the temperatures around the center of the pool are fairly uniform, whereas extreme temperature gradients of 4500 K mm^{-1} are encountered in the stagnation region. Since the stagnation region is only ≈ 0.1 mm wide, small spatial disturbances result in large changes in the temperature gradient and thus the resulting local Marangoni forces. This makes the flow highly unstable, and strong disturbances are indeed visible on the free surface of the pool (Fig. 6.9a), which evolve rapidly in time.

At the highest laser power, case 5 (Fig. 6.9b), the pool volume is larger, but the general flow features are similar to the previously discussed case 4. The stagnation region is quite a bit wider, leading to much lower gradients of 2100 K mm^{-1}, and the oscillations observed at the free surface are less intermittent.

With the computed temperatures at the free surface, we can determine Nusselt numbers $Nu = P/(r_q\lambda(T_{max} - T_s))$ as discussed previously. The values for all cases lie between 14 and 22, highlighting the large effect of fluid flow on heat transfer in the liquid pools.

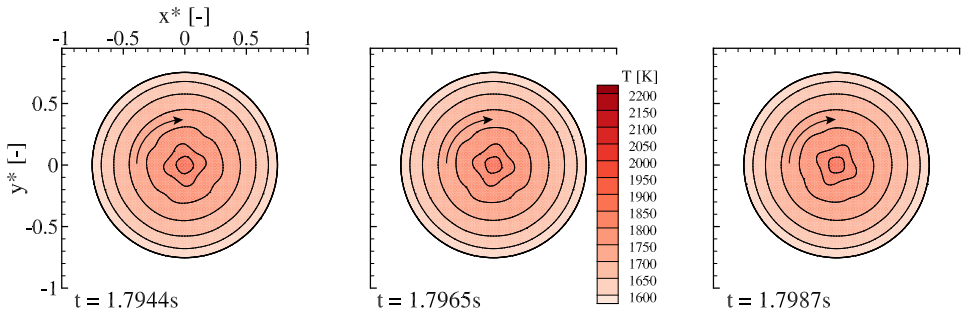

(a) Square pattern

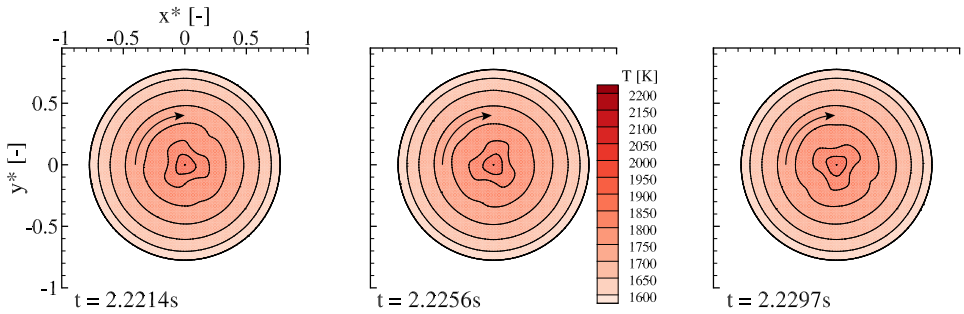

(b) Trefoil pattern

Figure 6.7.: Steady clockwise rotational motion of initially square and later trefoil shaped isotherm pattern on free surface, case 2.

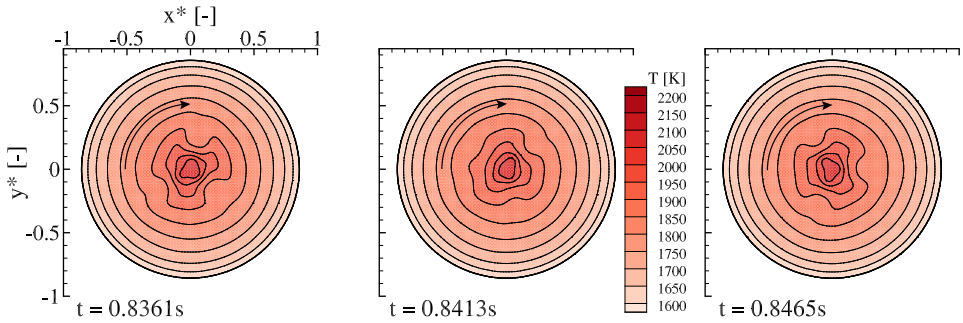

(a) Clockwise rotation

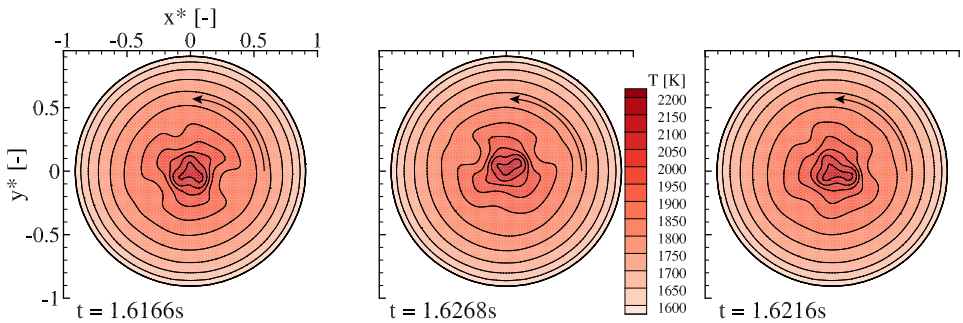

(b) Counter-clockwise rotation

Figure 6.8.: Isotherms on free surface, case 3, showing clockwise rotation of the trefoil pattern at a certain time instance followed by counter-clockwise rotation at a later time.

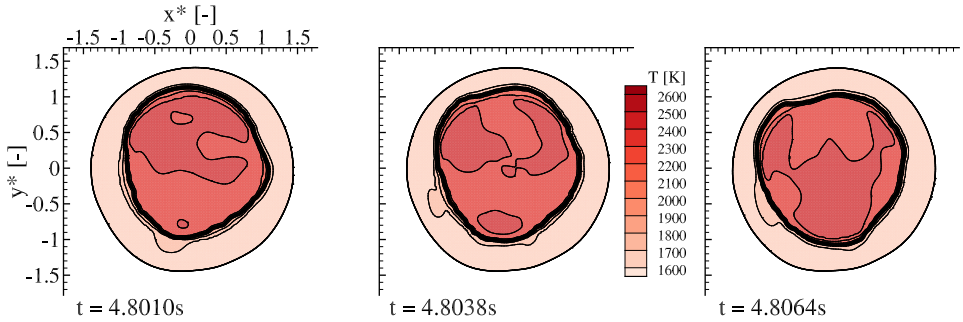

(a) Case 4

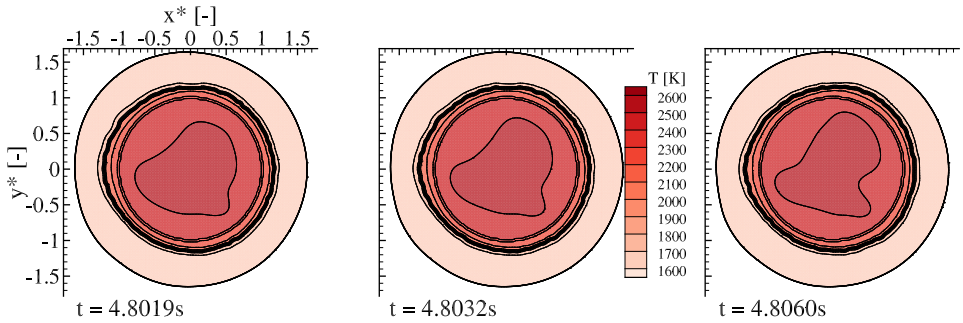

(b) Case 5

Figure 6.9.: Isotherms on the free surface for case 4 and 5, showing highly chaotic temporal behavior for case 4 and irregular, less intermittent behavior for case 5.

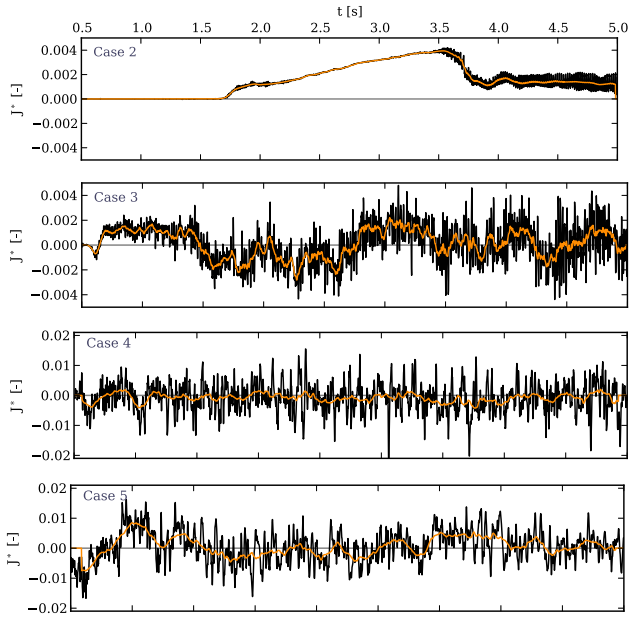

Figure 6.10.: Spatially averaged angular momentum J^* of the free surface over time (orange line: moving average) for increasing laser power. Negative values translate to counter-clockwise motion.

There is a clearly visible rotational motion of the temperature pattern on the free surface in cases 2 and 3. Judging plainly from the temperature profile at the free surface such a motion could not be identified in the temperature profiles at the higher laser powers. We have therefore investigated the temporal behavior of the spatially averaged, normalized angular momentum $J^*(t) = \langle \vec{r} \times \vec{U} \rangle_A / \langle \vec{r} \cdot \vec{U} \rangle_A = \langle -yu_x + xu_y \rangle_A / \langle xu_x + yu_y \rangle_A$, where $\langle \rangle_A$ denotes the average over the pool surface (Fig. 6.10). For the stable non-rotational flow in case 1, $J^*(t) = 0$ for all t (not shown here). The onset of stable clockwise rotation after 1.7 s in case 2, and the onset of pulsation after roughly 3.6 s is clearly distinguished from the initial stable flow. Also clear are the reversals of the direction of rotation occurring for case 3. For case 4, the angular momentum over time frequently changes its sign and no clear rotational motion is visible in the plot. The averaged angular momentum at the highest laser power, case 5, exhibits more persistent features than the chaotic case 4, but the rotation is not as clear as in cases 2 and 3.

The rotationally oscillating surface temperature patterns and the oscillating rotational momentum of the pool surface reported here, particularly at low power (case 2), bear resemblance to hydrothermal waves [186–188], which have previously also been observed for capillary driven flows in low Prandtl number liquids in annular

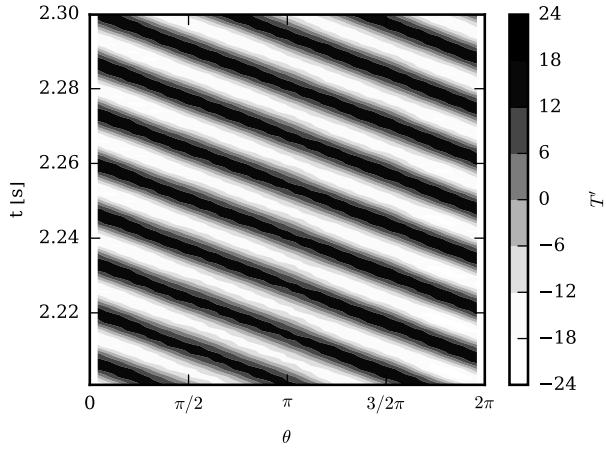

Figure 6.11.: Temperature fluctuation $T' = T - \frac{1}{2\pi}\oint_0^{2\pi} T d\theta$ at $r^* = 0.143$ in case 2, with θ the azimuthal coordinate

configurations [189]. At low Prandtl numbers, these waves travel obliquely to the thermal gradient. For the radial thermal gradients in the studied cases, this leads to thermal waves with an azimuthal velocity component, as is indeed observed. This is further illustrated in Fig.6.11, showing temperature perturbations around the time-averaged temperature as a function of time as a function of the azimuthal coordinate on a curve of constant r*=0.143 in case 2, resembling patterns reported for hydrothermal waves.

We do not, however, believe that hydrothermal waves are the main cause for the flow instabilities and turbulence observed experimentally in weld pools at higher laser powers [170, 173]. In simulations at high laser powers, flow instabilities leading to turbulence are present even when the flow is restricted to a 2D axisymmetric domain [190], excluding the presence of obliquely traveling thermal waves. The true mechanism underlying the flow instabilities will be further discussed in the following sections 6.3.4 and 6.3.5.

6.3.4. Flow within the pool

For the lowest laser power (case 1, not shown), the surface tension force towards the center of the pool drives a stable, symmetric donut-shaped vortex with upward flow at the edge and downward flow at the center of the pool. This leads to increased melting under the stagnation point at the center of the free surface. No azimuthal velocities are present. At increased laser powers the flow does not remain axisymmetric, with significant azimuthal velocities (case 2 and 3, Fig. 6.12a and Fig. 6.12b).

In the cross-section of the vortex-ring, the two halves oscillate and compete, one growing at the expense of the other. The oscillation is regular in case 2, and unpredictable in case 3, where even larger, non-homogeneous azimuthal velocities are present. Even though the flow is highly unsteady, the pool boundary still remains quasi-steady.

For the highest laser powers, instead of the singular surface stagnation point at the lower powers, there is a stagnation ring at the free surface, where the outward surface flow from the pool center meets the inward flow from the pool boundary, from which a strong circular jet towards the base of the pool emerges. There are thus two main counter-rotating donut-shaped vortex rings which are visible as four major counter-rotating vortices in the cross-section of the pool. At early times, the outer vortex ring is small, yet exerts a big influence on the stability of the flow. A plot of the instantaneous flow obtained for case 4, in and normal to the cross-section plane, is shown in Fig. 6.12c. We see that the flow is strongly asymmetric, and changes quickly and unpredictably within 0.004 s. Unlike the previously shown results at lower laser powers, not only the flow, but also the pool boundary is unsteady (Fig. 6.13a). The chaotic flow in the pool leads to a uniform transfer of heat from the surface to the base of the melt pool, and thus a much more uniform pool depth. At the highest laser power of case 5 (Fig. 6.12d), the circular jet stemming from the stagnation ring between the counter-rotating vortices is stronger and somewhat less chaotic, leading to a W-shaped melt pool. The pool boundary responds to the jet oscillation similarly to case 4, however, here the boundary oscillation occurs at a lower frequency (Fig. 6.13b).

To visualize the fluid flow within the opaque melt pool, an experimentalist would have to resort to X-ray radiography techniques using non-melting (e.g. tungsten) tracer particles. The particle traces will be complex two-dimensional projections of the real particle trajectory [191–193], and reconstruction of the 3D particle motion is not possible unless the pool is imaged with multiple sources and detectors simultaneously [194].

We have introduced three massless tracer particles into the pool in our simulations to obtain particle traces over a time of 1 s (Fig. 6.14), useful for comparison with experimental radiography results. For case 2 (not shown) and 3, the donut-shaped vortex-ring can be recognized fairly well in the particle tracks. It is remarkable that some of the particles traverse a very large area of the pool, whereas others remained local to a certain region. The tracks obtained agree qualitatively with experimental results by Czerner [192]. For cases 4 and 5 (latter not shown), all particles have moved through a large part of the domain, and the particle track projections are difficult to interpret, indicating turbulent flow. The particle track for case 1 is not shown as the laminar flow obtained leads to a very regular, linear pattern without deviations in the azimuthal direction.

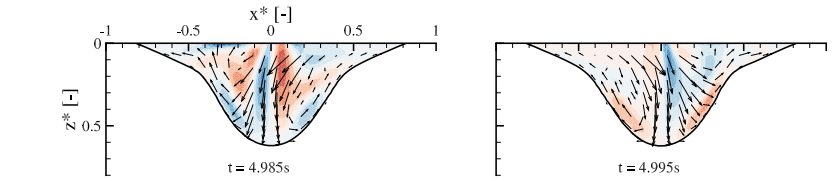

(a) Case 2

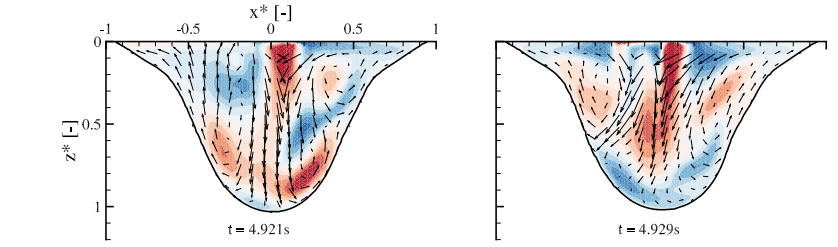

(b) Case 3

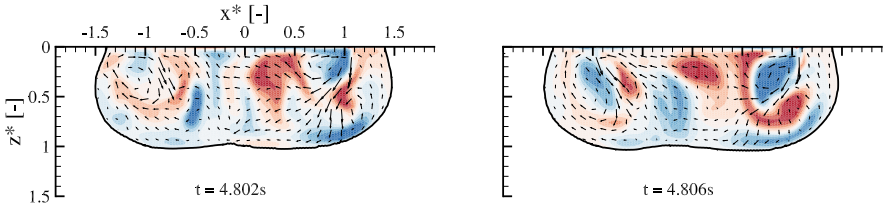

(c) Case 4

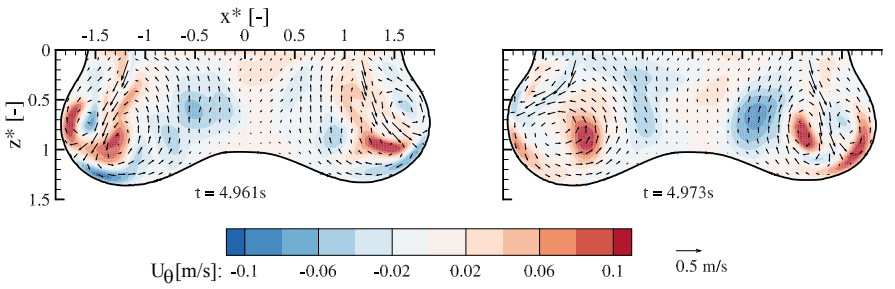

(d) Case 5

Figure 6.12.: Instationary in-plane (x,z) velocities in the $y^* = 0$ plane at two time instances indicated by vectors, and azimuthal velocities indicated by color contours (movies online).

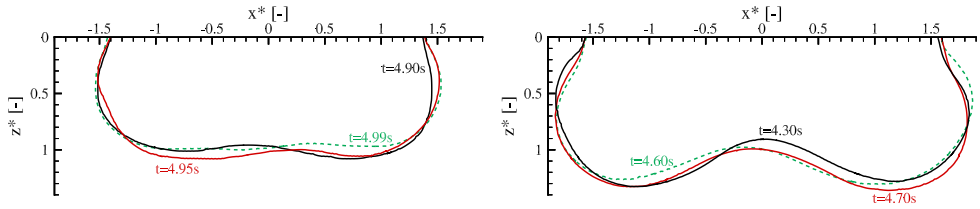

(a) Case 4 **(b)** Case 5

Figure 6.13.: Pool boundary oscillation observed in case 4 and 5. The oscillation frequency is significantly higher in case 4.

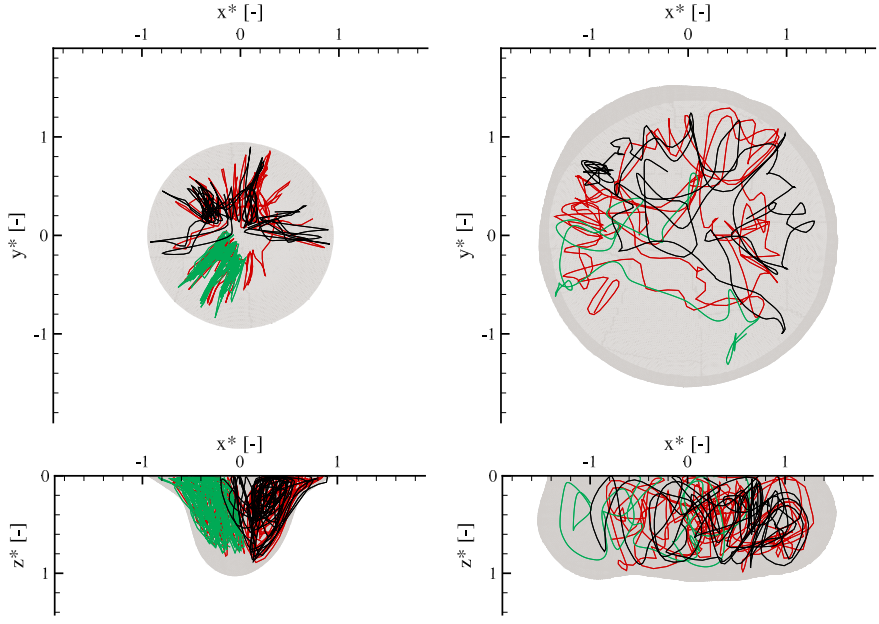

Figure 6.14.: Particle tracks for cases 3 (left half) and 4 (right half), showing regular unsteady motion for case 3 and chaotic motion for case 4.

6.3.5. Turbulence in the pool

To quantify the level of turbulence in the pool, we placed a monitoring probe at $(x^*, y^*, z^*) = (0, 0, 3/14)$ for cases 1-3, and $(x^*, y^*, z^*) = (15/14, 0, 3/14)$ for cases 4 and 5 (cf. Fig.5.3). The monitoring point is thus placed close to the free surface and in proximity to the downward jet emerging from the stagnation line at the free surface for all cases.

The temperature history at these monitoring points is shown in Fig.6.15. After roughly 2 s, the temperature signal in all cases reaches a quasi steady state, where the conductive heat loss to the solid material more or less matches the heat input. For case 1, the temperature signal is smooth, again indicating laminar flow (not shown here). The onset of rotational motion in case 2 cannot be seen in the probe history at the pool center. Only when the pulsation begins, the temperature signal at this location begins to oscillate with low amplitude and high frequency, with the most significant peak at 120 Hz. The temperature signal recorded for case 3 also oscillates at high frequency with a rather low amplitude. The signal spectrum is fairly uniform up to 100 Hz, where it drops. At the two highest laser powers, cases 4 and 5, the oscillation frequency is lower but amplitude is significantly higher. The signal spectrum drops off much sooner at around 10 Hz for case 4, with a sharp peak at 9 Hz. For case 5, the maximum frequency is shifted to 12.5 Hz and the frequency drops after 20 Hz.

Using the computed instantaneous velocity fluctuations $U' = U - \bar{U}$, we can determine the turbulent viscosity as $\nu_t = 0.09k^2/\epsilon$ (Fig.6.16), with the turbulent kinetic energy $k = \overline{U' \cdot U'}/2$ and the turbulent kinetic energy dissipation rate $\epsilon = \nu \overline{\nabla U' : \nabla U'}$. Here, all averages, denoted by an overbar, have been computed over the time interval between 4.5 and 5s. Unsurprisingly the turbulent viscosity is zero for the lowest power (case 1), since the flow is stable and laminar. For case 2, the turbulent viscosity is fairly uniform, with the space averaged value being of the same order of the molecular viscosity.

For case 3, the local turbulent viscosity observed in the return flow of the jet from the pool bottom reaches values up to 50 times the molecular value, much higher than the values at the lower laser powers. The space averaged turbulent viscosity is 4 times the molecular value. For case 4, higher values of up to 400 times the molecular viscosity are obtained surrounding the jet stemming from the stagnation ring at the free surface. The space averaged value of the turbulent viscosity is 18 times the molecular value, and thus the contribution of momentum diffusivity due to turbulence is significant. A very similar distribution is obtained for the highest laser power, case 5. However, the maximum value of 200 times the molecular value is somewhat lower, and so is the space averaged value of 7 times the molecular value.

In Fig.6.17 we show an isosurface of Q, the second invariant of ∇U, [195] to visualize coherent vortices in the pool. For case 3, we can identify a few coherent structures

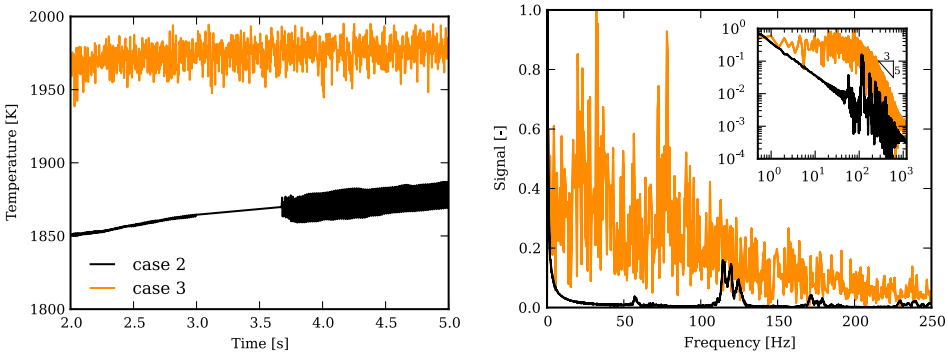

(a) Case 2 and 3, point $M_{1,2,3}$

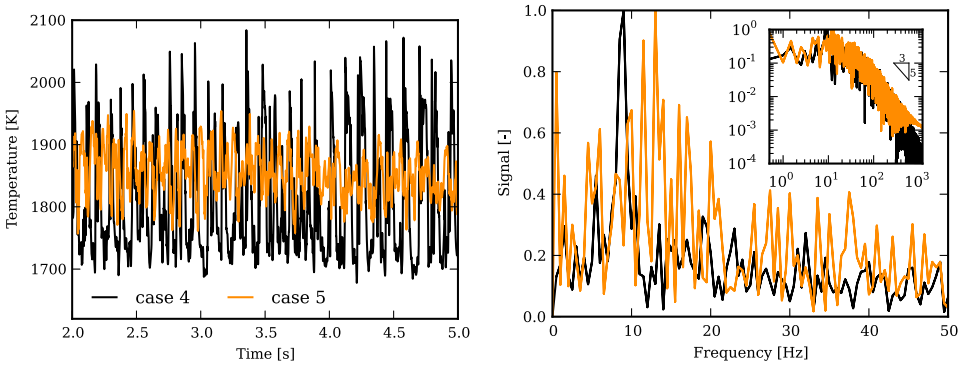

(b) Case 4 and 5, point $M_{4,5}$

Figure 6.15.: Temperature signal and spectrum at monitoring points (see Fig. 5.3) for varying laser powers. The signal spectrum has been normalized with the respective maximum peak.

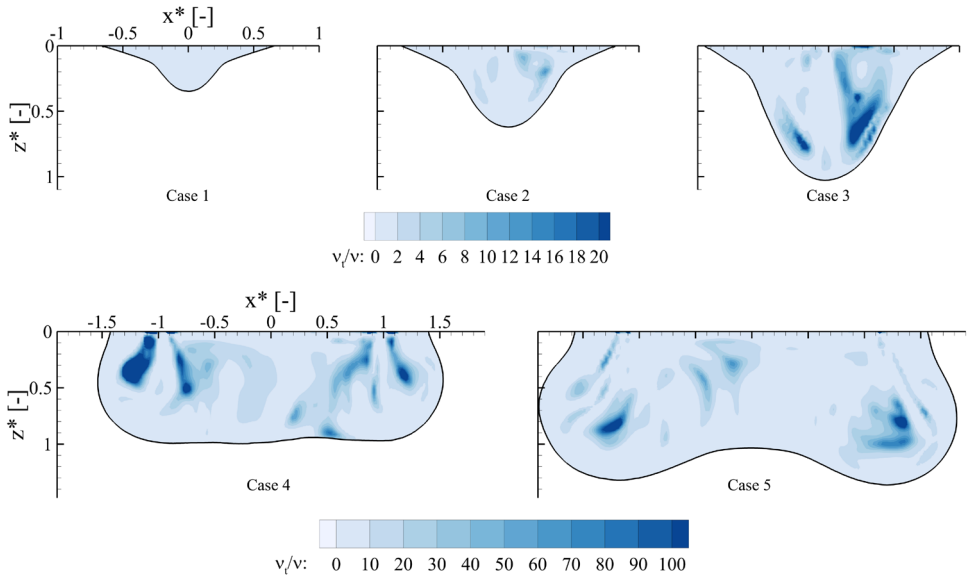

Figure 6.16.: Ratio of turbulent diffusivity over molecular diffusivity ν_t/ν in the $y^* = 0$ plane, based on turbulent kinetic energy and turbulence dissipation averaged over the 4.5 to 5 s period.

which span a large area of the pool, wrapping around in a corkscrew-like shape. Similarly to the temperature patterns at the free surface discussed earlier, the vortex structures rotate with time. For case 4, a large coherent structure appears, with a long connected vortex tube that spans the entire pool circumference and few isolated tubes around it. At the highest laser power, case 5, the structure has broken up significantly, and is much less uniform.

6.4. Conclusions

We studied the flow and heat transfer in low Prandtl number liquid pools driven by thermocapillary forces that arise due to surface tension gradients caused by temperature gradients across the free surface. Unlike previous studies on thermocapillary instabilities, we take into account phase change and the presence of a surface active species, which dramatically changes the relationship between surface tension γ and temperature T, leading to a maximum in the surface tension at a temperature T_c. Qualitative experimental observations[134, 169, 170, 173, 185, 192] of such systems have indicated the occurrence of flow instabilities and possibly even turbulence.

We find a stable, laminar flow for a Marangoni number of 2.1×10^6. A slightly

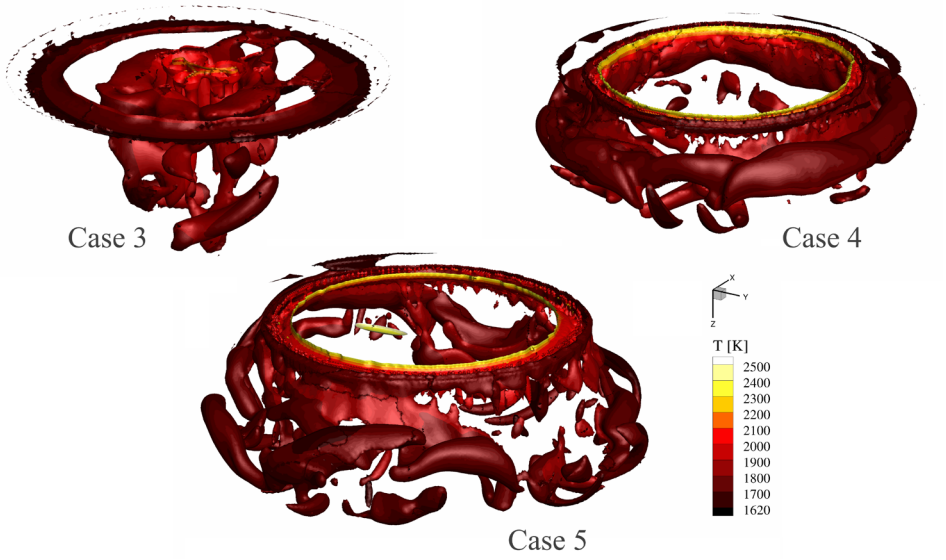

Figure 6.17.: Isosurface of Q at a time instance, colored according to temperature, visualizing vortex tubes in the unsteady liquid pools.

higher Marangoni number of 2.8×10^6 initially triggers a self-sustained rotational instability, as long as the maximum temperature is below T_c. Once the critical temperature T_c is exceeded and the surface tension temperature coefficient $\partial\gamma/\partial T$ locally changes its sign, a regular pulsating, non-turbulent motion is superposed on the rotation.

At Marangoni numbers of 4.6×10^6 and higher, temperatures so far above T_c are reached that the Marangoni force directed towards the pool boundary has a clear effect on the free surface flow, noticeably decelerating or even reversing the flow, causing significant flow instabilities. The amplitude and frequency spectrum of temperature oscillations support the argument of enhanced heat and momentum transport due to turbulent flow in the melt pool. The computed turbulent viscosity is locally orders of magnitude larger than the molecular value, and averaged in space it is 4-20 times larger. This enhanced heat and momentum transport is in agreement with ad-hoc modifications necessary to match experimental results in previously published numerical studies of industrial processes involving thermocapillary flows in liquid low Prandtl number pools, where the flow has been assumed to be laminar [87, 89, 127–131].

It is noteworthy that the self-sustained oscillations arise even without taking into account complex interactions such as a deformable liquid-gas interface, temperature dependent material properties, non-uniform surfactant concentrations or additional, competing forces such as buoyancy.

7. Conclusion and outlook

In this thesis, a model for the numerical simulation of conduction mode laser welding has been presented. The focus of the work lies on the coupling between macroscale fluid flow and heat transfer and mesoscale phenomena occurring in the weld pool, specifically (i) the mesoscale solidification structure developing after the heat source has been shut off, and (ii) increased heat and mass transfer and kinetic energy dissipation due to mesoscale eddies in the liquid pool.

To investigate the solidification structure, the macroscale fluid flow and heat transfer model has been coupled to a mesoscale solidification model. To investigate mesoscale flow effects, i.e. flow instabilities and turbulence, two approaches have been employed: a direct numerical simulation (DNS) capable of resolving the mesoscale effects in time and space, as well as a large eddy simulation (LES) where the mesoscale is filtered and replaced by a subgridscale model to reduce the computational cost.

7.1. Conclusions and answers to research questions

The main conclusions of this work are as follows:

(1) The combined macro-mesoscale model has been applied to study the melting and solidification of a laser spot weld on two Fe-Cr-Ni steel alloys, *viz*. with a low and high sulfur content. The predicted solidification evolution has been compared to that obtained with the commonly used equilibrium enthalpy method, in which solidification kinetics is ignored. Apart from the fact that an equilibrium method cannot predict the important transitions in grain morphology, a marked difference between the two methods was observed in the thermal gradients within the weld pool during solidification. This in turn has a strong impact on the developing grain structure. However, if only the weld pool shape is of interest, the equilibrium enthalpy method is found to be sufficient to obtain accurate results.

Addressing our research question 1 (see sec. 1.2):

The use of grain refining particles was found to be an effective means to favorably alter the grain morphology by initiating a transition from columnar to equiaxed growth. This transition was found to be not very sensitive to model parameters, which are the coherency threshold value and the density of grain refining particles (above a certain critical value). Neglecting fluid flow during the cooling phase, as

done in previously reported studies, was found to have a significant influence on the predicted weld pool shape and grain morphology. Thus any accurate simulation of weld pools should include fluid flow.

(2) A longstanding question in the modeling of weld pool flows is the relevance of flow instabilities and turbulence. Indications of such instabilities have been observed experimentally, but the effect has been ignored or over-simplified in modeling studies to date. DNS results presented in this thesis have shown turbulence to be relevant in conduction mode laser welding, even when complex effects such as a deformable free surface, additional flow driving forces besides the thermocapillary force, or surfactant redistribution are ignored. Such effects will likely further destabilize the flow increasing turbulence levels. It is thus important to take turbulence into account when simulating weld pool flows.

Addressing our research question 2 (see sec.1.2):

Turbulence in weld pools was found to lead to a significant increase in momentum and thermal energy transport, manifesting itself as an increased apparent viscosity and thermal conductivity in coarse grained flow simulations. In our simulations, we found an average effective viscosity of $\mathcal{O}(10)$ times the laminar viscosity. The effect of turbulence was found to be highly non-uniform and can thus not properly be replicated with a constant factor increase in transport properties, as commonly applied in the welding literature. However, even with our detailed DNS approach for modeling turbulence, our model simulations have failed to reproduce experimental results with respect to the (post-solidification) shape of the weld pool, which suggests some significant physical effects have still been wrongfully neglected. This is further discussed below.

(3) Using the DNS results, a dynamic LES approach has been validated, which was then applied to simulate a laser welding process over a wide range of powers, translating into more than an order of magnitude variation (2×10^6 - 3×10^7) in the Marangoni number.

Addressing our research question 3 (see sec.1.2):

It was shown that the flow is stable, axisymmetric and laminar below a critical Marangoni number, above which a stable transient rotational motion develops. At even higher Marangoni numbers, the flow becomes turbulent.

7.2. Discussion and outlook

As discussed above, even when taking turbulence into account through detailed DNS or LES approaches, our model simulations have failed to reproduce experimental results with respect to the (post-solidification) shape of the weld pool. This suggests some significant physical effects have still been wrongfully neglected. A likely

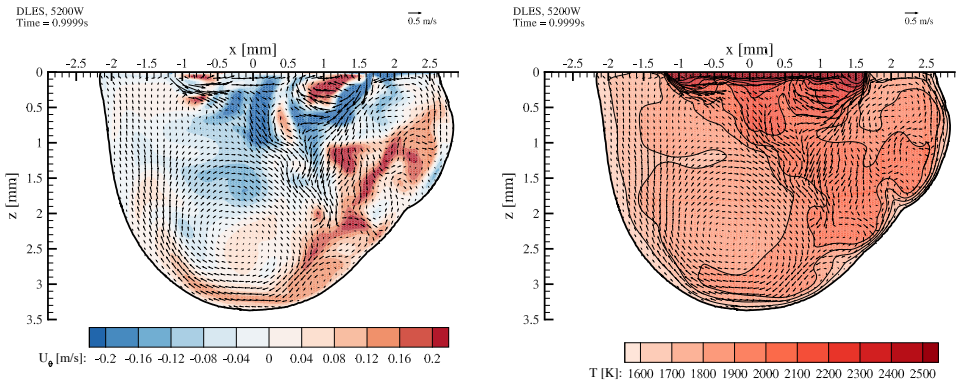

(a) Azimuthal velocity **(b)** Temperature

Figure 7.1.: Weld pool flow and temperature at t=1 s, taking into account the surface active effect of both sulfur and oxygen. The pool shape is closer to the experimental result shown in Fig. 3.11c than the result presented in chapter 5, Fig.5.6.

deficiency lies in the simplistic inclusion of surface active elements in the model. We have assumed only a single surfactant to be present which is homogeneously distributed, neglecting any surface chemistry or surfactant redistribution.

A possible first next step, while still assuming homogeneously distributed surfactant concentrations, would be to include the simultaneous influence of multiple surfactants, e.g. the combined effect of sulfur and oxygen. Models exist to estimate the combined effect of oxygen and sulfur on the surface tension [81]. We have applied such a model in a dynamic LES simulation of the 5200 W, 150ppm sulfur Pitscheneder laser welding case [89] discussed in detail in sec.3.3.2. Unlike what was done in chapter 3, here we obtained promising results for the weld pool shape without any artificial enhancement of the transport coefficients, as shown in Fig.7.1.

However, keeping the assumption of a spatially and temporally constant surfactant concentration is problematic to justify [196]. Sulfur, and even more so oxygen, react with other, secondary, species in the liquid pool, such as aluminum, and thereby can be rendered inert. The concentration of the secondary species may vary in time and space due to vaporization. Furthermore, the concentration of surface active species at the free surface is not necessarily the same as in the bulk of the pool. Adsorption and desorption as well as the redistribution of species along the liquid-gas interface have been shown to lead to non-uniformities in the surface concentration of surface active species. The above effects are even more relevant when taking into account ambient oxygen, e.g. mixed into the otherwise inert shielding gas. Inclusion of some of these phenomena has been shown to improve simulation results [136, 137, 172].

Finally, non-homogeneous distributions of the surfactant will not only modify the

thermocapillary force, but also lead to an additional solutocapillary force that has not been taken into account in the context of welding.

Ehlen et al. [102] and Saldi et al. [103] have shown that the shape of the weld pool may still change significantly during the solidification stage. Thus, the often neglected solidification stage can have a significant influence on the prediction of the weld pool shape. Both Ehlen et al. and Saldi et al. assumed a constant homogeneous surfactant concentration, during the melting stage as well as the solidification stage, leading to thermocapillary forces only. The latter vanish when temperature gradients diminish during the solidification stage. Yin and Emi [197], however, have shown that segregation of sulfur and oxygen during solidification can lead to additional solutocapillary forces with a significant influence on the melt pool flow. These solutocapillary forces remain active even when the thermal gradients diminish during solidification. Including the effect of segregation and taking into account solutocapillary forces might thus further improve the simulation predictions.

Further research on weld pool simulations should focus on physiochemical predictions of spatial and temporal concentration variations of surface active species within the weld pool, in mutual interaction with the fluid flow, both during the melting and the solidification stage.

A. Appendix

A.1. Typical material properties of liquid steel

Table A.1.: Typical material properties of liquid steel

Property	Value	Unit
λ	35	$\mathrm{W\,m^{-1}\,K^{-1}}$
c_p	700	$\mathrm{J\,kg^{-1}\,K^{-1}}$
ρ	7000	$\mathrm{kg\,m^{-3}}$
β_T	-7×10^{-6}	$\mathrm{m\,K^{-1}}$
ν	8×10^{-7}	$\mathrm{m^2\,s^{-1}}$
σ_T	-4.3×10^{-4}	$\mathrm{N\,m^{-1}\,K^{-1}}$
σ_e	10^6	$\mathrm{S\,m^{-1}}$
μ_m	$4\pi \times 10^{-7}$	$\mathrm{H\,m^{-1}}$

A.2. Modeling of thermal conductivity

The simplest correlation to obtain a temperature dependent thermal conductivity is the Wiedeman-Franz-Lorenz (WFL) law. It states that the ratio of thermal and electric conductivity is roughly constant, and thus the thermal conductivity can be obtained from the (easier to measure) electric conductivity:

$$\frac{\lambda}{\sigma_e} = L_{WFL} T, \;\; L_{WFL} = 2.44 \cdot 10^{-8} W\Omega K^{-2} \tag{A.1}$$

Temperature dependent data for the electric resistivity can be found e. g. in Wilthan et al. [198] or the electrical resistivity handbook [199]. The correlations by Wilthan et al. have been tested, and it is to note that equation 24 in their work is likely to be

erroneous. Thus it has been left out, and the correlations reduce to:

$$\rho_e \cdot 10^6 = \begin{cases} 0.015 + 1.998 \cdot 10^{-4} T + 5.433 \cdot 10^{-7} T^2 & \\ \qquad + 1.935 \cdot 10^{-10} T^3 & , T < 1050\,\mathrm{K} \\ 0.591 + 6.594 \cdot 10^{-4} T - 1.648 \cdot 10^{-7} T^2 & , 1050\,\mathrm{K} < T < 1800\,\mathrm{K} \\ 1.232 + 2.342 \cdot 10^{-5} T & , 1800\,\mathrm{K} < T \end{cases} \tag{A.2}$$

There are some drawbacks to the WFL law: First, L_{WFL} is not strictly a constant, but varies to a certain extent from one material to another (up to 25%), and second, that the WFL implicitly assumes all thermal transport occurs through free electrons, although some thermal transport in metals is achieved by lattice vibrations. And finally, the WFL law is only valid for solids.

A more accurate estimation of the thermal conductivity which also includes the effect of lattice vibrations is given by Mills [200]:

$$\lambda_s = \begin{cases} \lambda_{298} + \frac{T - 298K}{775K} \cdot (25 - \lambda_{298}) & , T < 1060\,\mathrm{K} \\ 25 + 0.013 \cdot (T - 1073) & , 1060\,\mathrm{K} < T < 1573\,\mathrm{K} \end{cases} \tag{A.3}$$

Again, this estimation is only valid for the solid steel alloy. For the liquid, all steel alloys tend towards a constant value of $33\,\mathrm{W\,m^{-1}\,K}$. The uncertainty is specified by $\pm 10\%$. In the laser welding code, λ_{298} is specfied as a constant which was manually calculated with data given by the reference for an Fe-1.5Mn-0.5C alloy. See Mills [200] on coefficients for other alloys.

A.3. Linearization of the energy equation

The latent heat release during melting is dependent on the liquid fraction, which in turn is dependent on the temperature. Naturally the release of heat changes the solution of the energy conservation equation as well, and thus this term makes the energy equation non-linear. There are many ways to handle the non-linearity to enable solving the equation [201]. Because of it's rapid convergence and numerical stability, the source term method devised by Voller and Swaminathan [83] has been adopted into the solver developed as part of this thesis.

To reduce the algorithm description to it's essence, we start with a simplified energy equation for a stagnant medium:

$$\frac{\partial H}{\partial t} = \nabla \cdot (\lambda \nabla T) \tag{A.4}$$

The equation can be rewritten in terms of temperatures:

$$\rho c_p \frac{\partial T}{\partial t} = \nabla \cdot (\lambda \nabla T) + \underbrace{\rho h_f \frac{\partial g}{\partial t}}_{S} \tag{A.5}$$

The source term is discretized as $S = \rho h_f (g_P^{m+1} - g_P^{old})/\Delta t$, where the unknown g_P^{m+1} can be replaced by a Taylor expansion

$$g_P^{m+1} = g_P^m + \frac{dF}{dT}\left[T_P^{m+1} - F^{-1}(g_P^m)\right] \tag{A.6}$$

$F(T)$ is the function used to describe the solid fraction evolution (here, a linear dependency on temperature, equation 2.13), F^{-1} is a function that determines a temperature for a given liquid fraction, and dF/dT is an analytically determined derivative of the solid fraction function, which is a constant when a linear update function is used.

To improve convergence, the source term can additionally be split up into an implicit and an explicit part, $S = S_P T_P^{m+1} + S_C$, with

$$S_P = \frac{\rho h_f}{\Delta t}\frac{dF}{dT} \tag{A.7}$$

$$S_C = \frac{\rho h_f}{\Delta t}\left[\left(g_P^m - g_P^{old}\right) - \frac{dF}{dT}F^{-1}(g_P^m)\right] \tag{A.8}$$

After calculating the updated temperature, the liquid fraction can be corrected by using equation A.6. The algorithm usually converges after few iterations (less than five).

Using a front-tracking technique to determine the position of the solid-liquid interface, the evolution of the solid fraction cannot be linearized using a Taylor expansion, as no algebraic formulation for the update is given. Here, we have to resort to operator splitting accompanied by underrelaxation:

$$\rho c_p \frac{\partial T}{\partial t} = \nabla \cdot (\lambda \nabla T) + \underbrace{\rho h_f \frac{\partial f_s \phi_s}{\partial t}}_{S} \tag{A.9}$$

$$S = \rho h_f \left(f_{s,P}^{old} \frac{(\phi_{s,P}^{t+1} - \phi_{s,P}^{old})}{\Delta t} + \phi_{s,P}^{old} \frac{(f_{s,P}^{m+1} - V_{s,P}^{old})}{\Delta t} \right) \tag{A.10}$$

Here, ϕ_s is the volume fraction of mushy material in a given computational cell as determined by the front tracking algorithm. ϕ_s is computed explicitly based on the temperature computed in the previous time step. This introduces a time step limit for stability, which is less restrictive than the Courant number criterion for fluid flow. The thickening of the mushy zone, i.e. how much material within the mushy zone is actually solid and how much is liquid, is given by the term f_s. Here, we assume f_s is linearly dependent on temperature. The resulting source term in the temperature equation is non-linear, which is solved by operator splitting, i.e. the successive solution of T^{m+1} and f_s^{m+1}. This fixed-point iteration will typically only converge when both T and f_s are underrelaxed:

$$f_s^{m+1} = \omega_s f_s^{m+1} + (1 - \omega_s) f_s^m \tag{A.11}$$

A typical value for ω_s is 0.3.

A.4. Moving frame of reference

Unlike the spot welds investigated in this thesis, often linear welds with a translating heat source or target are performed. Here, the velocity can be decomposed into a constant translational component and the superimposed fluid velocity

$$\vec{U} = \vec{U}_f + \vec{U}_t \tag{A.12}$$

Applying the decomposition to the governing equations and simplifying the terms gives

$$\nabla \cdot (\rho \vec{U}_f) = 0 \tag{A.13}$$

$$\rho c_p \frac{\partial}{\partial t} T + \nabla \cdot (\rho c_p T \vec{U}_f) + \nabla \cdot (\rho c_p T \vec{U}_t) - \nabla \cdot (\rho g h_f \vec{U}_f) = \nabla \cdot \lambda \nabla T + \rho h_f \frac{\partial}{\partial t} g \tag{A.14}$$

$$\rho\frac{\partial}{\partial t}\vec{U}_f + \nabla\cdot(\rho\vec{U}_f\vec{U}_f) + \nabla\cdot(\rho\vec{U}_t\vec{U}_f) = \nabla\cdot\nu\nabla U_f - \frac{\mu}{\rho K_0}\frac{g^2}{(1-g)^3+\epsilon}U_f - \frac{1}{\rho}\nabla p \tag{A.15}$$

A detailed derivation and validation of these equations can be found in Beekers [202].

A.5. Material properties for LES simulations

The dimensioned material properties used are listed in Tab. A.2 for convenience. The relationship between surface tension and temperature shown in Fig. 6.2 is:

$$\gamma = \gamma_0 - \partial\gamma/\partial T|_0(T - T_0) - RT\Gamma_s \ln\left[1 + k_l a_s \exp(\Delta H^0/(RT))\right] \tag{A.16}$$

Table A.2.: Material properties

Property	Value	Unit
Solidus temperature T_s	1610	K
Liquidus temperature T_l	1620	K
Mushy zone porosity coefficient μ/K_0	10^6	$\mathrm{N\,s\,m^{-4}}$
Specific heat capacity c_p	670	$\mathrm{J\,kg^{-1}\,K^{-1}}$
Density ρ	8100	$\mathrm{kg\,m^{-3}}$
Thermal conductivity λ	22.9	$\mathrm{W\,m^{-1}\,K^{-1}}$
Latent heat of fusion h_f	2.508×10^5	$\mathrm{J\,kg^{-1}}$
Viscosity μ	6×10^{-3}	Pa s
Surface tension temperature coefficient $\partial\gamma/\partial T\|_0$	-5.0×10^{-4}	$\mathrm{N\,m^{-1}\,K^{-1}}$
Entropy factor k_l	3.18×10^{-3}	–
Standard heat of adsorption ΔH^0	-1.66×10^8	$\mathrm{J\,kg^{-1}}$
Surface excess at saturation Γ_s	1.3×10^{-8}	$\mathrm{kmol\,m^{-2}}$
Surfactant activity a_s	150×10^{-4}	wt%

Bibliography

[1] W. Moos, R. Janßen-Timmen, J. Klöpper, and N. Leonenko. Gesamtwirtschaftliche und sektorale Wertschöpfung aus der Produktion und Anwendung von Fügetechnik in Deutschland und Europa. *Schweißen&Schneiden*, 65(9):572–584, 2013.

[2] Cyril S. Smith. Art, technology, and science: Notes on their historical interaction. *Technology and Culture*, 11(4):493–549, October 1970. doi: 10.2307/3102690.

[3] F. C. Campbell. *Joining - Understanding the Basics*. ASM International, 2011. ISBN 978-1-61503-825-1.

[4] James G. Bralla. *Handbook of Manufacturing Processes - How Products, Components and Materials are Made*. Industrial Press, 2007. ISBN 978-0-8311-3179-1.

[5] K. Weman. *Welding Processes Handbook (Woodhead Publishing Series in Welding and Other Joining Technologies)*. Woodhead Publishing, 2 edition, November 2011.

[6] A. C. Davies. *Welding science and technology*. Cambridge University Press, 1992. ISBN 9780521434034.

[7] Electric welding for shipbuilding. *Scientific American*, 87 (2248supp):79–80, February 1919. ISSN 0036-8733. doi: 10.1038/scientificamerican02011919-79supp.

[8] Annette O'Brien, editor. *Welding Processes, Part 1*, volume 2 of *Welding Handbook*. American Welding Society, 9 edition, 2004. ISBN 0-87171-729-8.

[9] R.W. Cahn. *The Coming of Materials Science, Volume 5 (Pergamon Materials Series)*. Pergamon, 1 edition, March 2001. ISBN 0080426794.

[10] Division on Engineering and Physical Sciences and Engineering. *Materials and Man's Needs: Materials Science and Engineering*. National Academies Press, January 1974. ISBN 0309022207.

[11] Gerald L. Liedl. The science of materials. *Scientific American*, 255(4):126–134, October 1986. ISSN 0036-8733. doi: 10.1038/scientificamerican1086-126.

[12] Aldo V. La Rocca. Laser applications in manufacturing. *Scientific American*, 246 (3):94–103, March 1982. ISSN 0036-8733. doi: 10.1038/scientificamerican0382-94.

[13] W. S. Bennett and G. S. Mills. GTA weldability studies on high manganese stainless steel. *Welding Journal*, 53:548–s–553–s, December 1974.

[14] S. S. Glickstein and W. Yeniscavich. A review of minor element effects on the welding arc and weld penetration. *Welding Research Council Bulletin*, (226), May 1977.

[15] K. Ishizaki. Interfacial tension theory of arc welding phenomena: formation of welding bead. *J. Jap. Weld. Soc.*, 34(2):146–153, 1965.

[16] R. A. Woods and D. R. Milner. Motion in the weld pool in arc welding. *Welding Journal*, 50(4):163–s–173–s, April 1971. ISSN 0043-2296.

[17] W. H. S. Lawson and H. W. Kerr. Fluid motion in GTA weld pools. Part 1: Flow patterns and weld pool homogeneity. *Welding Research International*, 6(5):63–80, 1976. ISSN 0306-9427.

[18] D. R. Atthey. A mathematical model for fluid flow in a weld pool at high currents. *Journal of Fluid Mechanics*, 98(04):787–801, June 1980. ISSN 1469-7645. doi: 10.1017/s0022112080000390.

[19] J. R. Roper and D. L. Olson. Capillarity effects in the GTA weld penetration of 21-6-9 stainless steel. *Welding Journal*, 57:103–s–107–s, April 1978.

[20] Dag Andersson. Streaming due to a thermal surface tension gradient - a summary. *Journal of Colloid and Interface Science*, 56(1):184–185, jul 1976. ISSN 00219797. doi: 10.1016/0021-9797(76)90163-6.

[21] C. R. Heiple and J. R. Roper. Mechanism for minor element effect on GTA fusion zone geometry. *Welding Journal*, 61(4):97–s–102–s, 1982.

[22] C. R. Heiple, J. R. Roper, R. T. Stagner, and R. J. Aden. Surface active element effects on the shape of GTA, laser, and electron beam welds. *Welding Journal*, 62 (3):72–s+, March 1983.

[23] John Goldak, Aditya Chakravarti, and Malcolm Bibby. A new finite element model for welding heat sources. *Metallurgical Transactions B*, 15(2):299–305, 1984. doi: 10.1007/bf02667333.

[24] L. E. Cram. A model of the cathode of a thermionic arc. *Journal of Physics D: Applied Physics*, 16(9):1643+, September 1983. ISSN 0022-3727. doi: 10.1088/0022-3727/16/9/011.

[25] J. J. Lowke. Calculated properties of vertical arcs stabilized by natural convection. *Journal of Applied Physics*, 50(1):147–157, January 1979. ISSN 0021-8979. doi: 10.1063/1.325698.

[26] J. McKelliget and J. Szekely. Heat transfer and fluid flow in the welding arc. *Metallurgical and Materials Transactions A*, 17(7):1139–1148, July 1986. ISSN 0360-2133. doi: 10.1007/bf02665312.

[27] Lars-Erik Lindgren. Finite element modeling and simulation of welding part 1: Increased complexity. *Journal of Thermal Stresses*, 24(2):141–192, February 2001. doi: 10.1080/01495730150500442.

[28] J. C. Villafuerte, E. Pardo, and H. W. Kerr. The effect of alloy composition and welding conditions on columnar-equiaxed transitions in ferritic stainless steel gas-tungsten arc welds. *Metallurgical Transactions A*, 21(7):2009–2019, 1990. doi: 10.1007/bf02647249.

[29] R. T. C. Choo, J. Szekely, and R. C. Westhoff. On the calculation of the free surface temperature of gas-tungsten-arc weld pools from first principles: Part i. modeling the welding arc. *Metallurgical Transactions B*, 23(3):357–369, 1992. doi: 10.1007/bf02656291.

[30] R. T. C. Choo, J. Szekely, and S. A. David. On the calculation of the free surface temperature of gas-tungsten-arc weld pools from first principles: Part ii. modeling the weld pool and comparison with experiments. *Metallurgical Transactions B*, 23(3):371–384, 1992. doi: 10.1007/bf02656292.

[31] Anthony B. Murphy. A self-consistent three-dimensional model of the arc, electrode and weld pool in gas metal arc welding. *Journal of Physics D: Applied Physics*, 44(19):194009+, May 2011. ISSN 0022-3727. doi: 10.1088/0022-3727/44/19/194009.

[32] P. Sahoo, T. Debroy, and M. McNallan. Surface tension of binary metal - surface active solute systems under conditions relevant to welding metallurgy. *Metallurgical and Materials Transactions B*, 19(3):483–491–491, June 1988. ISSN 0360-2141. doi: 10.1007/bf02657748.

[33] Mingming Tong, Gregory Duggan, Jun Liu, Yu Xie, Mike Dodge, Lee Aucott, Hongbiao Dong, Ruslan L. Davidchack, Jon Dantzig, Olga Barrera, Alan C. F. Cocks, Hiroto Kitaguchi, Sergio Lozano-Perez, Chuangxin Zhao, Ian M. Richardson, Anton Kidess, Chris R. Kleijn, Shuwen Wen, Roger Barnett, and David J. Browne. Multiscale, multiphysics numerical modeling of fusion welding with experimental characterization and validation. *JOM*, November 2012. ISSN 1047-4838. doi: 10.1007/s11837-012-0499-6.

[34] NEN-EN 14610:2004 Lassen en verwante processen - Definities van lasprocessen voor metalen. Technical report, 2004.

[35] R. P. Behringer and Guenter Ahlers. Heat transport and temporal evolution of fluid flow near the Rayleigh-Bénard instability in cylindrical containers. *Journal of Fluid Mechanics*, 125:219–258, December 1982. ISSN 1469-7645. doi: 10.1017/s0022112082003322.

[36] Damiân Rivas and Simon Ostrach. Scaling of low-Prandtl-number thermocapillary flows. *International Journal of Heat and Mass Transfer*, 35(6):1469–1479, June 1992. ISSN 00179310. doi: 10.1016/0017-9310(92)90037-s.

[37] Alain Pumir and Laure Blumenfeld. Heat transport in a liquid layer locally heated on its free surface. *Physical Review E*, 54:R4528–R4531, November 1996. doi: 10.1103/physreve.54.r4528.

[38] S. Chakraborty, S. Sarkar, and P. Dutta. Scaling analysis of momentum and heat transport in gas tungsten arc weld pools. *Science and Technology of Welding and Joining*, 7(2):88–94, April 2002. ISSN 13621718. doi: 10.1179/136217102225001322.

[39] T. DebRoy and S. A. David. Physical processes in fusion welding. *Reviews of Modern Physics*, 67(1):85–112, January 1995. doi: 10.1103/revmodphys.67.85.

[40] Nilanjan Chakraborty, Dipankar Chatterjee, and Suman Chakraborty. A scaling analysis of turbulent transport in laser surface alloying process. *Journal of Applied Physics*, 96(8):4569–4577, 2004. doi: 10.1063/1.1790061.

[41] Nilanjan Chakraborty and Suman Chakraborty. Thermal transport regimes and generalized regime diagram for high energy surface melting processes. *Metallurgical and Materials Transactions B*, 38(1):143–147, February 2007. ISSN 1073-5615. doi: 10.1007/s11663-006-9000-7.

[42] Eung-Ji Ha and Woo-Seung Kim. A study of low-power density laser welding process with evolution of free surface. *International Journal of Heat and Fluid Flow*, 26(4):613–621, August 2005. ISSN 0142727X. doi: 10.1016/j.ijheatfluidflow.2005.03.009.

[43] Damián Rivas. High-Reynolds-number thermocapillary flows in shallow enclosures. *Physics of Fluids A: Fluid Dynamics (1989-1993)*, 3(2):280–291, February 1991. ISSN 0899-8213. doi: 10.1063/1.858136.

[44] Randall L. Zehr. *Thermocapillary convection in laser melted pools during materials processing*. PhD thesis, University of Illinois at Urbana-Champaign, 1991.

[45] P. S. Wei, J. S. Yeh, C. N. Ting, T. DebRoy, F. K. Chung, and C. L. Lin. The effects of Prandtl number on wavy weld boundary. *International Journal of Heat and Mass Transfer*, 52(15-16):3790–3798, July 2009. ISSN 00179310. doi: 10.1016/j.ijheatmasstransfer.2009.02.020.

[46] Wajira U. Mirihanage and David J. Browne. Combined analytical/numerical modelling of nucleation and growth during equiaxed solidification under the influence of thermal convection. *Computational Materials Science*, 46(4):777–784, October 2009. ISSN 09270256. doi: 10.1016/j.commatsci.2009.04.016.

[47] C. Winkler, G. Amberg, H. Inoue, and T. Koseki. A numerical and experimental investigation of qualitatively different weld pool shapes. In H. Cerjak and H. K. D. H. Bhadeshia, editors, *Mathematical Modelling of Weld Phenomena 4*, Materials Modelling Series, pages 37–69, London, September 1997. IOM Communications Ltd. ISBN 1-86125-060-6.

[48] Ivaldo L. Ferreira, Vaughan R. Voller, Britta Nestler, and Amauri Garcia. Two-dimensional numerical model for the analysis of macrosegregation during solidification. *Computational Materials Science*, 46(2):358–366, August 2009. ISSN 09270256. doi: 10.1016/j.commatsci.2009.03.020.

[49] C. Swaminathan and V. R. Voller. Towards a general numerical scheme for solidification systems. *International Journal of Heat and Mass Transfer*, 40(12):2859–2868, August 1997. ISSN 00179310. doi: 10.1016/s0017-9310(96)00329-8.

[50] C. Swaminathan and V. Voller. A general enthalpy method for modeling solidification processes. *Metallurgical and Materials Transactions B*, 23(5):651–664, October 1992. ISSN 0360-2141. doi: 10.1007/BF02649725.

[51] D. R. Poirier. Permeability for flow of interdendritic liquid in columnar-dendritic alloys. *Metallurgical Transactions B*, 18(1):245–255, 1987. doi: 10.1007/bf02658450.

[52] A. Singh, R. Pardeshi, and B. Basu. Modelling of convection during solidification of metal and alloys. *Sadhana*, 26(1):139–162, February 2001. ISSN 0256-2499. doi: 10.1007/bf02728483.

[53] V. R. Voller and C. Prakash. A fixed grid numerical modelling methodology for convection-diffusion mushy region phase-change problems. *International Journal of Heat and Mass Transfer*, 30(8):1709–1719, August 1987. ISSN 0017-9310. doi: 10.1016/0017-9310(87)90317-6.

[54] Jerzy Banaszek and David J. Browne. Modelling columnar dendritic growth into an undercooled metallic melt in the presence of convection. *Materials Transactions*, 46(6):1378–1387, 2005. ISSN 1345-9678.

[55] J. Banaszek, S. McFadden, D. J. Browne, L. Sturz, and G. Zimmermann. Natural convection and Columnar-to-Equiaxed transition prediction in a Front-Tracking model of alloy solidification. *Metallurgical and Materials Transactions A*, 38(7):1476–1484, 2007. doi: 10.1007/s11661-007-9140-7.

[56] R. Rai, G. G. Roy, and T. DebRoy. A computationally efficient model of convective heat transfer and solidification characteristics during keyhole mode laser welding. *Journal of Applied Physics*, 101(5):054909+, 2007. doi: 10.1063/1.2537587.

[57] A. D. Brent, V. R. Voller, and K. J. Reid. Enthalpy-porosity technique for modeling convection-diffusion phase change: Application to the melting of a pure metal. *Numerical Heat Transfer*, 13(3):297–318, April 1988. doi: 10.1080/10407788808913615.

[58] R. Pardeshi, V. Voller, A. Singh, and P. Dutta. An explicit-implicit time stepping scheme for solidification models. *International Journal of Heat and Mass Transfer*, 51(13-14):3399–3409, July 2008. ISSN 00179310. doi: 10.1016/j.ijheatmasstransfer.2007.11.060.

[59] W. Bennon and F. Incropera. A continuum model for momentum, heat and species transport in binary solid-liquid phase change systems - I. Model formulation. *International Journal of Heat and Mass Transfer*, 30(10):2161–2170, October 1987. ISSN 00179310. doi: 10.1016/0017-9310(87)90094-9.

[60] Jonathan A. Dantzig. Modelling liquid-solid phase changes with melt convection. *Int. J. Numer. Meth. Engng.*, 28(8):1769–1785, 1989. doi: 10.1002/nme.1620280805.

[61] David G. Thomas. Transport characteristics of suspension: VIII. A note on the viscosity of Newtonian suspensions of uniform spherical particles. *Journal of Colloid Science*, 20(3):267–277, March 1965. ISSN 00958522. doi: 10.1016/0095-8522(65)90016-4.

[62] D. Bergström. *The Absorption of Laser Light by Rough Metal Surfaces*. PhD thesis, Luleå University of Technology, August 2008.

[63] A. Mahrle and E. Beyer. Theoretical aspects of fibre laser cutting. *Journal of Physics D: Applied Physics*, 42(17):175507+, September 2009. ISSN 0022-3727. doi: 10.1088/0022-3727/42/17/175507.

[64] David R. Lide. *CRC Handbook of Chemistry and Physics, 88th Edition (CRC Handbook of Chemistry & Physics)*. CRC Press, 88 edition, June 2007. ISBN 0849304881.

[65] Edward D. Palik. *Handbook of Optical Constants of Solids (5 Volume Set)*. Academic Press, January 1997. ISBN 012544415X.

[66] Moriaki Wakaki, editor. *Physical Properties and Data of Optical Materials*. CRC Press, 2007. ISBN 978-0-8247-2761-1. doi: 10.1201/9781420015508.

[67] J. Xie, A. Kar, J. A. Rothenflue, and W. P. Latham. Temperature-dependent absorptivity and cutting capability of CO2, Nd:YAG and chemical oxygen-iodine lasers. *Journal of Laser Applications*, 9(2):77–85, April 1997. ISSN 1042-346X.

[68] F Dausinger and Jl Shen. Energy coupling efficiency in laser-surface treatment. *ISIJ International*, 33(9):925–933, 1993.

[69] G. Belton. Langmuir adsorption, the Gibbs adsorption isotherm, and interracial kinetics in liquid metal systems. *Metallurgical and Materials Transactions B*, 7(1):35–42, March 1976. ISSN 0360-2141. doi: 10.1007/BF02652817.

[70] LeThu Hoai and Joonho Lee. Effect of surface adsorption of carbon on the surface tension of liquid Fe-Mn-C alloys. *Journal of Materials Science*, 47(24):8303–8307, September 2012. ISSN 0022-2461. doi: 10.1007/s10853-012-6836-x.

[71] Yunkyum Kim, Junghyuk Lim, Joongkil Choe, and Joonho Lee. Surface tension of liquid Fe-O alloys: Revisiting Belton's two-step adsorption model. 45(3):947–952, 2014. doi: 10.1007/s11663-014-0033-z.

[72] Joonho Lee, Koji Yamamoto, and Kazuki Morita. Surface tension of liquid Fe-Cr-O alloys at 1823 K. *Metallurgical and Materials Transactions B*, 36(2):241–246, April 2005. ISSN 1073-5615. doi: 10.1007/s11663-005-0025-0.

[73] Z. Li, K. Mukai, M. Zeze, and K. C. Mills. Determination of the surface tension of liquid stainless steel. *Journal of Materials Science*, 40(9-10):2191–2195, May 2005. ISSN 0022-2461. doi: 10.1007/s10853-005-1931-x.

[74] K. C. Mills and B. J. Keene. Factors affecting variable weld penetration. *International Materials Reviews*, 35(1):185–216, 1990. ISSN 0950-6608.

[75] M. Divakar, J. P. Hajra, A. Jakobsson, and S. Seetharaman. Thermodynamics of surfaces and adsorption in the Fe-C-S-O system. *Metallurgical and Materials Transactions B*, 31(2):267–276, 2000. doi: 10.1007/s11663-000-0045-8.

[76] J. P. Hajra and M. Divakar. Applicability of Butler's equation in interpreting the thermodynamic behavior of surfaces and adsorption in Fe-S-O melts. *Metallurgical and Materials Transactions B*, 27(2):241–253, 1996. doi: 10.1007/bf02915050.

[77] Joonho Lee and Kazuki Morita. Evaluation of surface tension and adsorption for liquid Fe-S alloys. *ISIJ International*, 42(6):588–594, 2002. ISSN 0915-1559. doi: 10.2355/isijinternational.42.588.

[78] Kusuhiro Mukai, Taishi Matsushita, Kenneth Mills, Seshadri Seetharaman, and Takahiro Furuzono. Surface tension of liquid alloys - A thermodynamic approach. *Metallurgical and Materials Transactions B*, 39(4):561–569, August 2008. ISSN 1073-5615. doi: 10.1007/s11663-008-9164-4.

[79] Jaana Riipi and Timo Fabritius. Surface tension of liquid Fe-N-O-S alloy. *ISIJ International*, 47(11):1575–1584, 2007. ISSN 0915-1559. doi: 10.2355/isijinternational.47.1575.

[80] Small, P. Sahoo, and K. Li. Prediction of surface tension in molten Fe-O-S system. *Scripta Metallurgica et Materialia*, 24(6):1155–1158, June 1990. ISSN 0956716X. doi: 10.1016/0956-716x(90)90316-9.

[81] Y. Su, Z. Li, and K. Mills. Equation to estimate the surface tensions of stainless steels. *Journal of Materials Science*, 40(9):2201–2205, May 2005. ISSN 0022-2461. doi: 10.1007/s10853-005-1933-8.

[82] Yuchu Su, K. Mills, and A. Dinsdale. A model to calculate surface tension of commercial alloys. *Journal of Materials Science*, 40(9):2185–2190–2190, May 2005. ISSN 0022-2461. doi: 10.1007/s10853-005-1930-y.

[83] V. R. Voller and C. R. Swaminathan. General source-based method for solidification phase change. *Numerical Heat Transfer, Part B: Fundamentals: An International Journal of Computation and Methodology*, 19(2):175–189, 1991. doi: 10.1080/10407799108944962.

[84] V. Voller. Development and application of a heat balance integral method for analysis of metallurgical solidification. *Applied Mathematical Modelling*, 13(1):3–11, January 1989. ISSN 0307904X. doi: 10.1016/0307-904X(89)90191-1.

[85] D. J. Browne and J. D. Hunt. A fixed grid front-tracking model of the growth of a columnar front and an equiaxed grain during solidification of an alloy. *Numerical Heat Transfer, Part B: Fundamentals: An International Journal of Computation and Methodology*, 45(5):395–419, 2004. doi: 10.1080/10407790490430606.

[86] L. H. Tan, S. S. Leong, E. Leonardi, and T. J. Barber. A numerical study of solid-liquid phase change with Marangoni effects using a multiphase approach. *Progress in Computational Fluid Dynamics, an International Journal*, 6(6):304–313, January 2006.

[87] Wenda Tan, Neil S. Bailey, and Yung C. Shin. Numerical modeling of transport phenomena and dendritic growth in laser spot conduction welding of 304 stainless steel. *Journal of Manufacturing Science and Engineering*, 134(4):041010+, 2012. ISSN 10871357. doi: 10.1115/1.4007101.

[88] J. Xie and A. Kar. Mathematical modeling of melting during laser materials processing. *Journal of Applied Physics*, 81(7):3015–3022, 1997. doi: 10.1063/1.364336.

[89] W. Pitscheneder, T. DebRoy, K. Mundra, and R. Ebner. Role of sulfur and processing variables on the temporal evolution of weld pool geometry during multikilowatt laser beam welding of steels. *Welding Journal*, 75(3):71–s–80–s, March 1996.

[90] G. J. Davies and J. G. Garland. Solidification structures and properties of fusion welds. *International Materials Reviews*, 20(1):83–108, January 1975. ISSN 0950-6608. doi: 10.1179/imr.1975.20.1.83.

[91] J. C. Villafuerte, H. W. Kerr, and S. A. David. Mechanisms of equiaxed grain formation in ferritic stainless steel gas tungsten arc welds. *Materials Science and Engineering: A*, 194(2):187–191, May 1995. ISSN 09215093. doi: 10.1016/0921-5093(94)09656-2.

[92] Bruce L. Bramfitt. The effect of carbide and nitride additions on the heterogeneous nucleation behavior of liquid iron. *Metallurgical Transactions*, 1(7):1987–1995, 1970. doi: 10.1007/bf02642799.

[93] Joo H. Park. Effect of inclusions on the solidification structures of ferritic stainless steel: Computational and experimental study of inclusion evolution. *Calphad*, 35(4):455–462, December 2011. ISSN 03645916. doi: 10.1016/j.calphad.2011.08.004.

[94] M. Gäumann and W. Kurz. Why is it so difficult to produce an equiaxed microstructure during welding? In H. Cerjak and H. K. D. H. Bhadeshia, editors, *Mathematical Modelling of Weld Phenomena 4*, Materials Modelling Series, pages 125–136, London, 1997. The Institute of Materials, IOM Communications. ISBN 1-86125-060-6.

[95] F. C. Campbell. *Defects leading to failure*, chapter A.8.6.1, pages 619+. ASM International, Materials Park, Ohio, 2012. ISBN 978-1-62198-373-6.

[96] S. A. David and J. M. Vitek. Correlation between solidification parameters and weld microstructures. *International Materials Reviews*, 34(1):213–245, January 1989. ISSN 0950-6608. doi: 10.1179/imr.1989.34.1.213.

[97] J. A. Spittle. Columnar to equiaxed grain transition in as solidified alloys. *International Materials Reviews*, 51(4):247–269, August 2006. ISSN 0950-6608. doi: 10.1179/174328006x102493.

[98] Wajira U. Mirihanage, Huijuan Dai, Hongbiao Dong, and David J. Browne. Computational modeling of columnar to equiaxed transition in alloy solidification. *Adv. Eng. Mater.*, 15(4):216–229, April 2013. doi: 10.1002/adem.201200220.

[99] Michael Kanouff and Ralph Greif. The unsteady development of a GTA weld pool. *International Journal of Heat and Mass Transfer*, 35(4):967–979, April 1992. ISSN 00179310. doi: 10.1016/0017-9310(92)90261-p.

[100] Y. P. Lei, Hidekazu Murakawa, Y. W. Shi, and X. Y. Li. Numerical analysis of the competitive influence of Marangoni flow and evaporation on heat surface temperature and molten pool shape in laser surface remelting. *Computational Materials Science*, 21(3):276–290, July 2001. ISSN 09270256. doi: 10.1016/s0927-0256(01)00143-4.

[101] W. Zhang, G. G. Roy, J. W. Elmer, and T. DebRoy. Modeling of heat transfer and fluid flow during gas tungsten arc spot welding of low carbon steel. *Journal of Applied Physics*, 93(5):3022–3033, 2003. doi: 10.1063/1.1540744.

[102] Georg Ehlen, Andreas Ludwig, and Peter R. Sahm. Simulation of time-dependent pool shape during laser spot welding: Transient effects. *Metallurgical and Materials Transactions A*, 34(12):2947–2961, December 2003. ISSN 1073-5623. doi: 10.1007/s11661-003-0194-x.

[103] Z. S. Saldi, A. Kidess, S. Kenjereš, C. Zhao, I. M. Richardson, and C. R. Kleijn. Effect of enhanced heat and mass transport and flow reversal during cool down on weld pool shapes in laser spot welding of steel. *International Journal of Heat and Mass Transfer*, 66:879–888, November 2013. ISSN 00179310. doi: 10.1016/j.ijheatmasstransfer.2013.07.085.

[104] Shijia Chen, Gildas Guillemot, and Charles-André Gandin. 3D coupled cellular automaton (CA)-finite element (FE) modeling for solidification grain structures in gas tungsten arc welding (GTAW). *ISIJ International*, 54(2):401–407, 2014. ISSN 0915-1559. doi: 10.2355/isijinternational.54.401.

[105] G. Duggan, W. U. Mirihanage, M. Tong, and D. J. Browne. A combined enthalpy / front tracking method for modelling melting and solidification in laser welding. *IOP Conference Series: Materials Science and Engineering*, 33(1):012026+, July 2012. ISSN 1757-899X. doi: 10.1088/1757-899x/33/1/012026.

[106] G. Duggan, M. Tong, and D. J. Browne. An integrated meso-scale numerical model of melting and solidification in laser welding. *IOP Conference Series: Materials Science and Engineering*, 27(1):012077+, January 2012. ISSN 1757-899X. doi: 10.1088/1757-899x/27/1/012077.

[107] T. Koseki, H. Inoue, Y. Fukuda, and A. Nogami. Numerical simulation of equiaxed grain formation in weld solidification. *Science and Technology of Ad-*

vanced Materials, 4(2):183–195, January 2003. ISSN 1468-6996. doi: 10.1016/s1468-6996(03)00026-3.

[108] X. H. Zhan, Z. B. Dong, Y. H. Wei, and Y. L. Xu. Dendritic grain growth simulation in weld molten pool based on CA-FD model. *Cryst. Res. Technol.*, 43(3): 253–259, March 2008. doi: 10.1002/crat.200710966.

[109] D. J. Browne and J. D. Hunt. A fixed grid front-tracking model of the growth of a columnar front and an equiaxed grain during solidification of an alloy. *Numerical Heat Transfer, Part B: Fundamentals*, 45(5):395–419, May 2004. doi: 10.1080/10407790490430606.

[110] M. H. Burden and J. D. Hunt. Cellular and dendritic growth. II. *Journal of Crystal Growth*, 22(2):109–116, April 1974. ISSN 00220248. doi: 10.1016/0022-0248(74)90127-4.

[111] W. Kurz, B. Giovanola, and R. Trivedi. Theory of microstructural development during rapid solidification. *Acta Metallurgica*, 34(5):823–830, May 1986. ISSN 00016160. doi: 10.1016/0001-6160(86)90056-8.

[112] J. S. Langer and J. Müller-Krumbhaar. Stability effects in dendritic crystal growth. *Journal of Crystal Growth*, 42:11–14, December 1977. ISSN 00220248. doi: 10.1016/0022-0248(77)90171-3.

[113] W. U. Mirihanage, K. V. Falch, I. Snigireva, A. Snigirev, Y. J. Li, L. Arnberg, and R. H. Mathiesen. Retrieval of three-dimensional spatial information from fast in situ two-dimensional synchrotron radiography of solidification microstructure evolution. *Acta Materialia*, 81:241–247, December 2014. ISSN 13596454. doi: 10.1016/j.actamat.2014.08.016.

[114] J. W. Christian. *The Theory of Transformations in Metals and Alloys (Part I + II): v. 1-2*. Pergamon, 1 edition, December 2002.

[115] V. B. Biscuola and M. A. Martorano. Mechanical blocking mechanism for the columnar to equiaxed transition. 39(12):2885–2895, 2008. doi: 10.1007/s11661-008-9643-x.

[116] Wajira Mirihanage, Shaun McFadden, and David J. Browne. Macroscopic model for predicting columnar to equiaxed transitions using columnar front tracking and average equiaxed growth. *Materials Science Forum*, 649:355–360, May 2010. ISSN 1662-9752. doi: 10.4028/www.scientific.net/msf.649.355.

[117] G. Duggan, M. Tong, and D. J. Browne. Modelling the creation and destruction of columnar and equiaxed zones during solidification and melting in multi-pass welding of steel. *Computational Materials Science*, 97:285–294, February 2015. ISSN 09270256. doi: 10.1016/j.commatsci.2014.09.022.

[118] H. G. Weller, G. Tabor, H. Jasak, and C. Fureby. A tensorial approach to computational continuum mechanics using object-oriented techniques. *Computers in Physics*, 12(6):620–631, 1998. doi: 10.1063/1.168744.

[119] John D. Hunter. Matplotlib: A 2D graphics environment. *Computing in Science and Engineering*, 9(3):90–95, May 2007. ISSN 1521-9615. doi: 10.1109/mcse.2007.55.

[120] R. I. Issa. Solution of the implicitly discretised fluid flow equations by operator-splitting. *Journal of Computational Physics*, 62(1):40–65, January 1986. ISSN 00219991. doi: 10.1016/0021-9991(86)90099-9.

[121] T. Koseki, H. Inoue, A. Nogami, and Y. Fukada. Columnar-to-equiaxed transition during solidification of steel welds. In S. A. David, editor, *6th International Trends in Welding Research Conference Proceedings*, Trends in Welding Research, pages 35–40. ASM International, ASM International, April 2002. ISBN 9781615032518 1615032517.

[122] J. W. Elmer, T. W. Eager, and S. M. Allen. Single-phase solidification during rapid resolidification of stainless steel alloys. In *Proc. of the Materials Weldability Symposium*, pages 143–150, Materials Park, OH, 143, May 1990. ASM International.

[123] R. F. Brooks, A. T. Dinsdale, and P. N. Quested. The measurement of viscosity of alloys - a review of methods, data and models. *Measurement Science and Technology*, 16(2):354+, January 2005. ISSN 0957-0233. doi: 10.1088/0957-0233/16/2/005.

[124] Thomas J. Lienert, Sudarsanam S. Babu, Thomas A. Siewert, and Viola L. Acoff. *Laser beam welding*, pages 558+. ASM International, 2011. ISBN 978-1-61344-660-7.

[125] P. J. Roache. Perspective: A method for uniform reporting of grid refinement studies. *Journal of Fluids Engineering*, 116(3):405–413, 1994. doi: 10.1115/1.2910291.

[126] J. D. Hunt. Steady state columnar and equiaxed growth of dendrites and eutectic. *Materials Science and Engineering*, 65(1):75–83, July 1984. ISSN 00255416. doi: 10.1016/0025-5416(84)90201-5.

[127] V. Pavlyk and U. Dilthey. A numerical and experimental study of fluid flow and heat transfer in stationary GTA weld pools. In H. Cerjak and H. K. D. H. Bhadeshia, editors, *Mathematical Modelling of Weld Phenomena 5*, Materials Modelling Series, pages 135–163. IOM Communications Ltd, 2001. ISBN 1 86125 115 7.

[128] T. D. Anderson, J. N. DuPont, and T. DebRoy. Origin of stray grain formation in single-crystal superalloy weld pools from heat transfer and fluid flow modeling. *Acta Materialia*, 58(4):1441–1454, February 2010. ISSN 13596454. doi: 10.1016/j.actamat.2009.10.051.

[129] A. De and T. DebRoy. Probing unknown welding parameters from convective heat transfer calculation and multivariable optimization. *Journal of*

Physics D: Applied Physics, 37(1):140+, December 2003. ISSN 0022-3727. doi: 10.1088/0022-3727/37/1/023.

[130] A. De and T. DebRoy. A smart model to estimate effective thermal conductivity and viscosity in the weld pool. *Journal of Applied Physics*, 95(9):5230–5240, 2004. doi: 10.1063/1.1695593.

[131] A. De and T. DebRoy. Improving reliability of heat and fluid flow calculation during conduction mode laser spot welding by multivariable optimisation. *Science and Technology of Welding and Joining*, 11(2):143–153, March 2006. ISSN 1362-1718. doi: 10.1179/174329306x84346.

[132] S. Mishra, T. J. Lienert, M. Q. Johnson, and T. DebRoy. An experimental and theoretical study of gas tungsten arc welding of stainless steel plates with different sulfur concentrations. *Acta Materialia*, 56(9):2133–2146, May 2008. ISSN 13596454. doi: 10.1016/j.actamat.2008.01.028.

[133] H. G. Kraus. Surface temperature measurements of GTA weld pools on thin-plate 304 stainless steel. *Welding Journal*, 68(3):84–s–91–s, March 1989.

[134] C. X. Zhao, V. van Steijn, I. M. Richardson, C. R. Kleijn, S. Kenjeres, and Z. Saldi. Unsteady interfacial phenomena during inward weld pool flow with an active surface oxide. *Science and Technology of Welding & Joining*, 14(2):132–140, February 2009. ISSN 1362-1718. doi: 10.1179/136217108x370281.

[135] C. Zhao. *Measurements of fluid flow in weld pools*. PhD thesis, Delft University of Technology, May 2011.

[136] C. Winkler, G. Amberg, H. Inoue, T. Koseki, and M. Fuji. Effect of surfactant redistribution on weld pool shape during gas tungsten arc welding. *Science and Technology of Welding and Joining*, 5(1):8–20, February 2000. ISSN 1362-1718. doi: 10.1179/stw.2000.5.1.8.

[137] C. Winkler and G. Amberg. Multicomponent surfactant mass transfer in GTA-welding. *Progress in Computational Fluid Dynamics, An International Journal*, 5(3-5): 190–206, April 2005. ISSN 1468-4349. doi: 10.1504/pcfd.2005.006754.

[138] X. He, J. W. Elmer, and T. DebRoy. Heat transfer and fluid flow in laser microwelding. *Journal of Applied Physics*, 97(8):084909+, April 2005. ISSN 0021-8979. doi: 10.1063/1.1873032.

[139] G. G. Roy, J. W. Elmer, and T. DebRoy. Mathematical modeling of heat transfer, fluid flow, and solidification during linear welding with a pulsed laser beam. *Journal of Applied Physics*, 100(3):034903+, 2006. doi: 10.1063/1.2214392.

[140] R. T. C. Choo and J. Szekely. The possible role of turbulence in GTA weld pool behaviour. *Welding Journal*, 73(2):25–S–31–S, 1994.

[141] Nilanjan Chakraborty, Suman Chakraborty, and Pradip Dutta. Modelling of turbulent transport in arc welding pools. *International Journal of Numerical Methods for Heat & Fluid Flow*, 13(1):7–30, 2003. ISSN 0961-5539. doi: 10.1108/09615530310456741.

[142] Nilanjan Chakraborty, Dipankar Chatterjee, and Suman Chakraborty. Modeling of turbulent transport in laser surface alloying. *Numerical Heat Transfer, Part A: Applications*, 46(10):1009–1032, December 2004. doi: 10.1080/10407780490517629.

[143] Nilanjan Chakraborty and Suman Chakraborty. Influences of sign of surface tension coefficient on turbulent weld pool convection in a gas tungsten arc welding (GTAW) process: A comparative study. *Journal of Heat Transfer*, 127(8):848+, 2005. ISSN 00221481. doi: 10.1115/1.1928913.

[144] Nilanjan Chakraborty, Suman Chakraborty, and Pradip Dutta. Three-dimensional modeling of turbulent weld pool convection in GTAW processes. *Numerical Heat Transfer, Part A: Applications*, 45(4):391–413, March 2004. doi: 10.1080/10407780490250364.

[145] Nilanjan Chakraborty and Suman Chakraborty. Modelling of turbulent molten pool convection in laser welding of a copper-nickel dissimilar couple. *International Journal of Heat and Mass Transfer*, 50(9-10):1805–1822, May 2007. ISSN 00179310. doi: 10.1016/j.ijheatmasstransfer.2006.10.030.

[146] Wenchao Dong, Shanping Lu, Dianzhong Li, and Yiyi Li. GTAW liquid pool convections and the weld shape variations under helium gas shielding. *International Journal of Heat and Mass Transfer*, 54(7-8):1420–1431, March 2011. ISSN 00179310. doi: 10.1016/j.ijheatmasstransfer.2010.07.069.

[147] Massoud Goodarzi, Roland Choo, Tomio Takasu, and James M. Toguri. The effect of the cathode tip angle on the gas tungsten arc welding arc and weld pool: II. The mathematical model for the weld pool. *Journal of Physics D: Applied Physics*, 31(5):569+, March 1998. ISSN 0022-3727. doi: 10.1088/0022-3727/31/5/014.

[148] K. Hong, D. Weckman, and A. Strong. The influence of thermofluids phenomena in gas tungsten arc welds in high and low thermal conductivity metals. *Canadian Metallurgical Quarterly*, 37(3-4):293–303, July 1998. ISSN 00084433. doi: 10.1016/s0008-4433(97)00021-9.

[149] K. Hong, D. C. Weckman, A. B. Strong, and W. Zheng. Modelling turbulent thermofluid flow in stationary gas tungsten arc weld pools. *Science and Technology of Welding and Joining*, 7(3):125–136, June 2002. ISSN 1362-1718. doi: 10.1179/136217102225002619.

[150] K. Hong, D. C. Weckman, A. B. Strong, and W. Zheng. Vorticity based turbulence model for thermofluids modelling of welds. *Science and Technology of Welding and Joining*, 8(5):313–324, October 2003. ISSN 1362-1718. doi: 10.1179/136217103225005507.

[151] J. Jaidi, K. S. S. Murthy, and P. Dutta. A k-ϵ model for turbulent weld pool convection in gas metal arc welding process. In S. A. David, editor, *6th International Trends in Welding Research Conference Proceedings*, Trends in Welding Research, pages 147–152. ASM International, ASM International, April 2002.

[152] J. Jaidi and P. Dutta. Three-dimensional turbulent weld pool convection in gas metal arc welding process. *Science and Technology of Welding and Joining*, 9(5): 407–414, October 2004. ISSN 1362-1718. doi: 10.1179/136217104225021814.

[153] Alexandros K. Skouras, Nilanjan Chakraborty, and Suman Chakraborty. Computational analysis of the effects of process parameters on molten pool transport in Cu-Ni dissimilar laser weld pool. *Numerical Heat Transfer, Part A: Applications*, 58(4):272–294, September 2010. doi: 10.1080/10407782.2010.505154.

[154] Xinxin Wang, Ding Fan, Jiankang Huang, and Yong Huang. A unified model of coupled arc plasma and weld pool for double electrodes TIG welding. *Journal of Physics D: Applied Physics*, 47(27):275202+, July 2014. ISSN 0022-3727. doi: 10.1088/0022-3727/47/27/275202.

[155] Dipankar Chatterjee and Suman Chakraborty. Large-eddy simulation of laser-induced surface-tension-driven flow. *Metallurgical and Materials Transactions B*, 36(6):743–754, December 2005. ISSN 1073-5615. doi: 10.1007/s11663-005-0078-0.

[156] Nilanjan Chakraborty and Suman Chakraborty. Thermal transport regimes and generalized regime diagram for high energy surface melting processes. *Metallurgical and Materials Transactions B*, 38(1):143–147, February 2007. ISSN 1073-5615. doi: 10.1007/s11663-006-9000-7.

[157] Edin Berberovic. *Investigation of Free-surface Flow Associated with Drop Impact: Numerical Simulations and Theoretical Modeling*. PhD thesis, Technische Universitaet Darmstadt, 2010.

[158] Virginie Gilard and Laurent-Emmanuel Brizzi. Slot jet impinging on a concave curved wall. *Journal of Fluids Engineering*, 127(3):595+, 2005. ISSN 00982202. doi: 10.1115/1.1905643.

[159] Michael F. Schatz and G. Paul Neitzel. Experiments on thermocapillary instabilities. *Annual Review of Fluid Mechanics*, 33(1):93–127, 2001. doi: 10.1146/annurev.fluid.33.1.93.

[160] M. Ohnishi, H. Azuma, and T. doi. Computer simulation of oscillatory Marangoni flow. *Acta Astronautica*, 26(8-10):685–696, August 1992. ISSN 00945765. doi: 10.1016/0094-5765(92)90158-f.

[161] D. Morvan and Ph Bournot. Oscillatory flow convection in a melted pool. *International Journal of Numerical Methods for Heat & Fluid Flow*, 6(1):13–20, January 1996. ISSN 0961-5539. doi: 10.1108/eum0000000004128.

[162] E. Bucchignani and D. Mansutti. Rayleigh-Marangoni horizontal convection of low Prandtl number fluids. *Physics of Fluids*, 16(9):3269–3280, September 2004. ISSN 1070-6631. doi: 10.1063/1.1772381.

[163] Mårten Levenstam, Gustav Amberg, and Christian Winkler. Instabilities of thermocapillary convection in a half-zone at intermediate Prandtl numbers. *Physics of Fluids*, 13(4):807–816, April 2001. ISSN 1070-6631. doi: 10.1063/1.1337063.

[164] M. Lappa. Three-dimensional numerical simulation of Marangoni flow instabilities in floating zones laterally heated by an equatorial ring. *Physics of Fluids*, 15(3):776–789, March 2003. ISSN 1070-6631. doi: 10.1063/1.1543147.

[165] Y. Kamotani, S. Matsumoto, and S. Yoda. Recent developments in oscillatory Marangoni convection. *Fluid Dynamics & Materials Processing*, 3(2):147–160, 2007. doi: 10.3970/fdmp.2007.003.147.

[166] You-Rong Li, Nobuyuki Imaishi, Takeshi Azami, and Taketoshi Hibiya. Three-dimensional oscillatory flow in a thin annular pool of silicon melt. *Journal of Crystal Growth*, 260(1-2):28–42, January 2004. ISSN 00220248. doi: 10.1016/j.jcrysgro.2003.08.017.

[167] B. Xu, X. Ai, and B. Q. Li. Rayleigh-Bénard-Marangoni instabilities of low-Prandtl-number fluid in a vertical cylinder with lateral heating. *Numerical Heat Transfer, Part A: Applications*, 51(12):1119–1135, June 2007. doi: 10.1080/10407780601009074.

[168] T. Hibiya, K. Morohoshi, and S. Ozawa. Oxygen partial pressure dependence of surface tension and its temperature coefficient for metallic melts: a discussion from the viewpoint of solubility and adsorption of oxygen. *Journal of Materials Science*, 45(8):1986–1992, December 2010. ISSN 0022-2461. doi: 10.1007/s10853-009-4107-2.

[169] T. Azami, S. Nakamura, and T. Hibiya. Effect of oxygen on thermocapillary convection in a molten silicon column under microgravity. *Journal of The Electrochemical Society*, 148(4):G185–G189, April 2001. ISSN 1945-7111. doi: 10.1149/1.1353579.

[170] C. X. Zhao, C. Kwakernaak, Y. Pan, I. M. Richardson, Z. Saldi, S. Kenjeres, and C. R. Kleijn. The effect of oxygen on transitional Marangoni flow in laser spot welding. *Acta Materialia*, 58(19):6345–6357, November 2010. ISSN 13596454. doi: 10.1016/j.actamat.2010.07.056.

[171] S. Kou, C. Limmaneevichitr, and Ps Wei. Oscillatory Marangoni flow: A fundamental study by conduction-mode laser spot welding. *Welding Journal*, 90(12):229–S–240–S, 2011.

[172] Minh Do-Quang, Gustav Amberg, and Claes-Ove Pettersson. Modeling of the adsorption kinetics and the convection of surfactants in a weld pool. *Journal of Heat Transfer*, 130(9):092102+, September 2008. ISSN 00221481. doi: 10.1115/1.2946476.

[173] Ch Karcher, R. Schaller, Th Boeck, Ch Metzner, and A. Thess. Turbulent heat transfer in liquid iron during electron beam evaporation. *International Journal of Heat and Mass Transfer*, 43(10):1759–1766, May 2000. ISSN 00179310. doi: 10.1016/s0017-9310(99)00248-3.

[174] B. Dikshit, G. R. Zende, M. S. Bhatia, and B. M. Suri. Convection in molten pool created by a concentrated energy flux on a solid metal target. *Physics of Fluids*, 21(8):084105+, August 2009. ISSN 1070-6631. doi: 10.1063/1.3210763.

[175] Thomas Boeck and Christian Karcher. Low-Prandtl-number Marangoni convection driven by localized heating on the free surface: Results of three-dimensional direct simulations. In Ranga Narayanan and Dietrich Schwabe, editors, *Interfacial Fluid Dynamics and Transport Processes*, volume 628 of *Lecture Notes in Physics*, pages 157–175. Springer Berlin Heidelberg, 2003. doi: 10.1007/978-3-540-45095-5_8.

[176] H. C. Kuhlmann and U. Schoisswohl. Flow instabilities in thermocapillary-buoyant liquid pools. *Journal of Fluid Mechanics*, 644:509–535, February 2010. ISSN 1469-7645. doi: 10.1017/s0022112009992953.

[177] Taketoshi Hibiya and Shumpei Ozawa. Effect of oxygen partial pressure on the Marangoni flow of molten metals. *Cryst. Res. Technol.*, 48(4):208–213, April 2013. doi: 10.1002/crat.201200514.

[178] S. Ozawa, S. Takahashi, N. Watanabe, and H. Fukuyama. Influence of oxygen adsorption on surface tension of molten nickel measured under reducing gas atmosphere. 35(9-10):1705–1711, 2014. doi: 10.1007/s10765-014-1674-5.

[179] Bernhard W. Righolt. *Hydrodynamics of electromagnetically controlled jet oscillations*. PhD thesis, Delft University of Technology, 2016.

[180] Eugene de Villiers. *The Potential of Large Eddy Simulation for the Modeling of Wall Bounded Flows*. PhD thesis, Imperial College of Science, Technology and Medicine, July 2006.

[181] D. K. Lilly. A proposed modification of the Germano subgrid-scale closure method. *Physics of Fluids A: Fluid Dynamics (1989-1993)*, 4(3):633–635, March 1992. ISSN 0899-8213. doi: 10.1063/1.858280.

[182] Alberto Passalacqua. dynamicSmagorinsky - Implementation of the dynamic Smagorinsky SGS model as proposed by Lilly (1992) for OpenFOAM. Published electronically online, `https://bitbucket.org/albertop/dynamicsmagorinsky`, 2014.

[183] Thomas M. Eidson. Numerical simulation of the turbulent Rayleigh-Bénard problem using subgrid modelling. *Journal of Fluid Mechanics*, 158:245–268, September 1985. ISSN 1469-7645. doi: 10.1017/s0022112085002634.

[184] S. Kenjereš and K. Hanjalić. LES, T-RANS and hybrid simulations of thermal convection at high Ra numbers. *International Journal of Heat and Fluid Flow*, 27(5): 800–810, October 2006. ISSN 0142727X. doi: 10.1016/j.ijheatfluidflow.2006.03.008.

[185] Chuangxin Zhao and Ian Richardson. Complex flow motions during laser welding. In *40th AIAA Plasmadynamics and Lasers Conference*, Fluid Dynamics

and Co-located Conferences. American Institute of Aeronautics and Astronautics, June 2009. doi: 10.2514/6.2009-3739.

[186] Marc K. Smith and Stephen H. Davis. Instabilities of dynamic thermocapillary liquid layers. part 1. convective instabilities. *Journal of Fluid Mechanics*, 132(-1): 119–144, July 1983. ISSN 1469-7645. doi: 10.1017/s0022112083001512.

[187] S. H. Davis. Thermocapillary instabilities. *Annual Review of Fluid Mechanics*, 19(1):403–435, 1987. doi: 10.1146/annurev.fl.19.010187.002155.

[188] Marcello Lappa. *Thermal convection patterns, evolution and stability*. Wiley, 2010. ISBN 9780470749999.

[189] Yourong Li, Lan Peng, Shuangying Wu, and Nobuyuki Imaishi. Bifurcation of thermocapillary convection in a shallow annular pool of silicon melt. *Acta Mechanica Sinica*, 23(1):43–48, 2007. doi: 10.1007/s10409-006-0053-2.

[190] Anton Kidess, Sasa Kenjeres, Bernhard W. Righolt, and Chris R. Kleijn. Marangoni driven turbulence in high energy surface melting processes. *International Journal of Thermal Sciences*, 104(104):412–422, June 2016. doi: 10.1016/j.ijthermalsci.2016.01.015.

[191] Yoshiaki Arata, Michio Tomie, Nobuyuki Abe, and Xiang-Yu Yao. Observation of molten metal flow during eb welding. *Transactions of JWRI*, 16(1):13–16, June 1987.

[192] Stefan Czerner. *Schmelzbaddynamik beim Laserstrahl-Wärmeleitungsschweißen von Eisenwerkstoffen*. PhD thesis, Universität Hannover, 2005.

[193] M. Gatzen, Z. Tang, F. Vollertsen, M. Mizutani, and S. Katayama. X-ray investigation of melt flow behavior under magnetic stirring regime in laser beam welding of aluminum. *Journal of Laser Applications*, 23(3):032002+, August 2011. ISSN 1938-1387. doi: 10.2351/1.3580552.

[194] Y. Morisada, H. Fujii, Y. Kawahito, K. Nakata, and M. Tanaka. Three-dimensional visualization of material flow during friction stir welding by two pairs of x-ray transmission systems. *Scripta Materialia*, 65(12):1085–1088, December 2011. ISSN 13596462. doi: 10.1016/j.scriptamat.2011.09.021.

[195] Yves Dubief and Franck Delcayre. On coherent-vortex identification in turbulence. *Journal of Turbulence*, 1(N11):1–22, 2000. doi: 10.1088/1468-5248/1/1/011.

[196] Yu, U. Gernert, T. Nink, and O. Bostanjoglo. Segregation and surface transport of impurities: New mechanisms affecting the surface morphology of laser treated metals. *Journal of Applied Physics*, 81(6):2835–2838, March 1997. ISSN 0021-8979. doi: 10.1063/1.363942.

[197] Hongbin Yin and Toshihiko Emi. Marangoni flow at the gas/melt interface of steel. *Metallurgical and Materials Transactions B*, 34(5):483–493, 2003. doi: 10.1007/s11663-003-0015-z.

[198] B. Wilthan, C. Cagran, and G. Pottlacher. Combined DSC and pulse-heating measurements of electrical resistivity and enthalpy of platinum, iron, and nickel. *International Journal of Thermophysics*, 25(5):1519–1534, September 2004. ISSN 0195-928X. doi: 10.1007/s10765-004-5756-7.

[199] G. T. Dyos and T. Farrell. *Electrical resistivity handbook*, volume 10. Peter Peregrinus Ltd, 1992.

[200] K. C. Mills. *Measurement and estimation of physical properties of metals at high temperatures*, chapter 4, pages 109+. CRC Press, 2005. ISBN 0-8493-3443-8.

[201] V. R. Voller, C. R. Swaminathan, and B. G. Thomas. Fixed grid techniques for phase change problems: A review. *International Journal for Numerical Methods in Engineering*, 30(4):875–898, 1990. ISSN 1097-0207. doi: 10.1002/nme.1620300419.

[202] Jaap Beekers. Numerical modeling of heat transfer and fluid flow in welding with a moving heat source. Technical report, Delft University of Technology, Delft, Netherlands, April 2014.

Nomenclature

A	Aspect ratio D/L	[-]
a_i	Chemical activity	[wt-pct]
C	Dendrite kinetics coefficient	$[\mathrm{m\,s^{-1}\,K^{-2}}]$
c	Speed of light	$[\mathrm{m\,s^{-1}}]$
C_0	Alloy composition	[wt-pct]
c_p	Heat capacity	$[\mathrm{J\,kg^{-1}\,K^{-1}}]$
D	Characteristic length scale (pool depth)	[m]
d_{min}	Minimum diameter of nucleating particles	[m]
D/Dt	Material derivative	
D_l	Diffusion coefficient of solute in the liquid	$[\mathrm{m^2\,s^{-1}}]$
$F(d)$	Cumulative distribution function for equiaxed nucleation	[-]
$\vec{F}_{damp}$	Momentum sink term due to solidification	$[\mathrm{m\,s^{-2}}]$
f_s	Volume fraction of solid in mush	[-]
g	Gravity	$[\mathrm{m\,s^{-2}}]$
g	Volume fraction of solid	[-]
H	Enthalpy	$[\mathrm{J\,kg^{-1}}]$
h	Convective heat transfer coefficient	$[\mathrm{W\,m^{-2}\,K^{-1}}]$
ΔH_0	Heat of adsorption	$[\mathrm{J\,kmol^{-1}}]$
h_f	Latent heat of fusion	$[\mathrm{J\,kg^{-1}}]$
J^*	Dimensionless angular momentum	[-]

K	Permeability	$[\mathrm{m}^2]$
k	Turbulent kinetic energy	$[\mathrm{m}^2\,\mathrm{s}^{-2}]$
K_i	Equilibrium constant adsorption reaction	[-]
k_L	Extinction coefficient	[-]
k_q	Gaussian distribution coefficient	[-]
L	Characteristic length scale (pool radius)	[m]
L_K	Kolmogorov length scale	[m]
m	Slope of the liquidus line	$[\mathrm{K(wt\text{-}pct}^{-1})]$
N	Count of nucleated particles	[-]
n	Refractive index	[-]
P	Laser / arc power	[W]
p	Pressure	[Pa]
Q_0	Heat flux density	$[\mathrm{W\,m}^{-2}]$
R	Ideal gas constant	$[\mathrm{m}^2\,\mathrm{kg\,s}^{-2}\,\mathrm{K}^{-1}\,\mathrm{mol}^{-1}]$
R	Volume averaged dendrite envelop radius	[m]
r_q	Laser beam radius, arc radius	[m]
S_{latent}	Latent heat source term	$[\mathrm{J\,m}^{-3}\,\mathrm{s}^{-1}]$
ΔS_v	Fusion entropy	$[\mathrm{J\,kg}^{-1}\,\mathrm{K}^{-1}]$
T	Temperature	[K]
ΔT_c	Local undercooling	[K]
t	Time	[s]
T_∞	Ambient temperature	[K]
t_K	Kolmogorov time scale	[s]
T_s, T_l	Solidus and liquidus temperature	[K]
U	Fluid velocity	$[\mathrm{m\,s}^{-1}]$

$\overline{U}$	Mean velocity	$[\mathrm{m\,s^{-1}}]$
U'	Velocity fluctuation	$[\mathrm{m\,s^{-1}}]$
U_s	Fluid velocity at free surface, characteristic velocity	$[\mathrm{m\,s^{-1}}]$
v	Dendrite tip velocity	$[\mathrm{m\,s^{-1}}]$
V_{equi}	Volume of equiaxed dendrites	$[\mathrm{m^3}]$
V_{ex}	Volume of existing equiaxed dendrites	$[\mathrm{m^3}]$
V_{new}	Volume of newly nucleated equiaxed dendrites	$[\mathrm{m^3}]$

Greek symbols

α	Thermal diffusivity	$[\mathrm{m^2\,s^{-1}}]$
α_p	Partition coefficient	[-]
β_T	Thermal expansion coefficient	$[\mathrm{K^{-1}}]$
ϵ	Emissivity	[-]
ϵ	Turbulent kinetic energy dissipation rate	$[\mathrm{m^2\,s^{-3}}]$
ϵ_0	Vacuum permittivity	$[\mathrm{F\,m^{-1}}]$
γ	Surface tension	$[\mathrm{N\,m^{-1}}]$
γ_{sl}	Solid-liquid interfacial tension	$[\mathrm{J\,m^{-2}}]$
Γ	Gibbs Thomson coefficient	$[\mathrm{m\,K}]$
Γ_s	Surface saturated excess concentration	$[\mathrm{kmol\,m^{-2}}]$
λ	Thermal conductivity	$[\mathrm{W\,m^{-1}\,K^{-1}}]$
λ_L	Laser beam wave length	[m]
μ	Dynamic viscosity	[Pa s]
$\mu_{1/2}$	Median inoculant diameter	[m]
ν	Kinematic viscosity	$[\mathrm{m^2\,s^{-1}}]$
ω	Vorticity	$[\mathrm{s^{-1}}]$
ϕ_{col}	Volume fraction of columnar dendrites	[-]

ϕ_{equi}	Volume fraction of equiaxed dendrites after taking into account grain impingement	[-]
ϕ_s	Volume fraction of mush	[-]
ρ	Density	$[\mathrm{kg\,m^{-3}}]$
ρ_{seeds}	Inoculant particle number density	$[\mathrm{m^{-3}}]$
σ_b	Stefan Boltzmann constant	$[\mathrm{W\,m^{-2}\,K^{-4}}]$
σ_d	Standard deviation for the log-normal distribution of inoculant diameters	[-]

Subscripts

n	Normal direction
t	Tangential direction

Acknowledgments

Chris you convinced me to come to Delft when I already had my mind set on a position elsewhere. Thank you for this opportunity, I learned a lot and your attention to detail helped us to produce a few nice papers. Your recommendation for the ASML PhD Master Class granted me two exciting days in Eindhoven, though I finally chose another path.

Sasa, your enthusiasm, especially during my last year in Delft, has been contagious. You have kept my spirits high during the most critical phase of my work, and I have greatly enjoyed our regular trips to the Bouwkunde espresso bar.

It has been a pleasure to work with the members of the Mintweld consortium, and I much enjoyed our get-togethers and discussions. All of you have left a lasting imprint on me. Ian, you're so passionate about welding it just had to rub off. I enjoyed our discussions, and the possibility to actually weld in your lab. David, Greg and Mingming, collaborating with you on our common paper was a great experience. David and Greg, I fondly remember sharing a pint or two with you in Oxford before heading out for dinner. Hongbiao, I am very grateful for your invitation to join your group for experiments at the Diamond synchrotron and the invitation to Leicester. Lee, working with you at Diamond and our snowboarding adventure together in Norway are some of the best memories from my time as a PhD candidate.

Anita, you're amazingly helpful, turning even the most dreadful administration work into a breeze. Stefan Mundlos, Franz Durst, Norbert Alleborn and Sadik Dost, your guidance and support in the early stages of my career helped me a lot. Vera Nübel, I'm grateful for the trust you place in me and the chance you gave me to prove myself.

My PhD track wouldn't have been enjoyable without my gezellige peers, the students of TP, and Evert. Never before have a encountered such a density of smart people. I would like to thank all of you for the great lunches, coffee breaks, borrels, conferences and nights out we've had, and I miss you all! Please forgive I won't get to name all of you in the following.

Jelle, Paul, Jaap and Gijs, I've learned a lot from you, and I hope you did too during your students projects in our group. Romboud, thanks for providing me with candy and your general sense of happiness during our night watches at TP! Conrad, I enjoyed our discussions, the toasties at the Navier-Stokes-Society and the drinks we've had.

Annekatrien, you helped me a lot getting settled in Delft, and I have yet to meet a match of your bakery skills. You also helped improve my Dutch, along with the boys of W220. Laurens, it was great to share an office with you during all those evenings and weekends, and making Oliebollen together for New Years. Michiel, I still recite "nog eendje dan", even back in Germany, thinking about the good times we've had. Duong and Wenjie, my OpenFOAM companions - thanks for the amazing Asian dinners we've had together. Wenjie, I wish we had started playing soccer together sooner! Anand, I enjoyed our many talks on work and life in general, and your visit to Augsburg. Sid, sharing a laugh and jokes on the whiteboard of our office has been a joy. Hrushikesh and Chirag, we only shared the office briefly, but had tons of interesting discussions in that time. Koen, thanks for all the fish! We didn't get to travel together for the PhD, but made up for that with a nice road trip. Rudi, the uitje to the dikke Dries was fantastic. Niels, I have good memories of the BBQs you hosted. Ina, it's really unfortunate our times in Delft only briefly overlapped. You've made an impact, and it's been great to spend time with you and the fantastic people of Catalysis!

Cees, thanks for pulling along all of TP into Ecast, helping me out with the epic Southside BBQ and all the fun and shenanigans we've had together. I'm sincerely sorry there's no room for friendship in *Civ V*. Bernhard and Dries, thank you for looking out for me, the many times you've had me in tears laughing and visiting me in Aux. I could write another whole book on the good times we've had.

Over the years, I've been fortunate to make many friends which are now scattered across the globe, and I look forward to seeing you again and adding to the great memories we've shared. Among these, I'd like to thank Oliver, Marcel, Tobias, Marco, Karin, and Armando for years of friendship, and your willingness to seek me out no matter it be in Erlangen, Victoria or Delft. Sarah, thanks for making Augsburg feel like home.

Finally, I would like to thank my family. Regina, Clemence and Hardy, thanks for being there for me all these years. Sophia, you've brought a lot of sunshine into our lives. Mischa, you are the best in-law I could have hoped for. Eve and Pete, I may be the tallest, but I still look up to you. I'm grateful for the bond we have and the love you give.

Mom, Dad, I can say with certainty that without your unconditional support and love, this thesis would have not been completed. I cannot thank you enough for all you do.

List of publications

[A1] J. Hecht, V. Seitz, M. Urban, F. Wagner, P. N. Robinson, A. Stiege, C. Dieterich, U. Kornak, U. Wilkening, N. Brieske, C. Zwingman, A. Kidess, S. Stricker, and S. Mundlos. Detection of novel skeletogenesis target genes by comprehensive analysis of a Runx2-/- mouse model. *Gene Expression Patterns*, 7(1-2), 2007.

[A2] A. Kidess, N. Armour, and S. Dost. Numerical study of the effect of magnetic fields in dissolution of silicon into germanium melt. *Journal of Crystal Growth*, 312(8), 2010.

[A3] A. Kidess, N. Armour, and S. Dost. A numerical simulation study of silicon dissolution under magnetic field. *Fluid Dynamics & Materials Processing*, 7(1):29–56, 2011.

[A4] M. Tong, J. Liu, Y. Xie, H. B. Dong, R. L. Davidchack, J. Dantzig, D. Ceresoli, N. Marzari, A. Cocks, C. Zhao, I. M. Richardson, A. Kidess, C. R. Kleijn, L. Hoglund, S. W. Wen, R. Barnett, and D. J. Browne. An integrated framework for multi-scale multi-physics numerical modelling of interface evolution in welding. *IOP Conference Series: Materials Science and Engineering*, 33(1):012029+, July 2012.

[A5] Z. Saldi, A. Kidess, S. Kenjereš, C. Zhao, I. M. Richardson, and C. R. Kleijn. Effect of enhanced heat and mass transport and flow reversal during cool down on weld pool shapes in laser spot welding of steel. *International Journal of Heat and Mass Transfer*, 66:879–888, November 2013.

[A6] M. Tong, G. Duggan, J. Liu, Y. Xie, M. Dodge, L. Aucott, H. B. Dong, R. L. Davidchack, J. Dantzig, O. Barrera, A. C. F. Cocks, H. Kitaguchi, S. Lozano-Perez, C. Zhao, I. M. Richardson, A. Kidess, C. R. Kleijn, S. W. Wen, R. Barnett, and D. J. Browne. Multiscale, multiphysics numerical modeling of fusion welding with experimental characterization and validation. *JOM*, 65(1):99–106, January 2013.

[A7] A. Kidess, M. Tong, G. Duggan, D. J. Browne, I. M. Richardson, S. Kenjereš, and C. R. Kleijn. An integrated model for the post-solidification shape and grain morphology of fusion welds. *International Journal of Heat and Mass Transfer*, 85:667–678, June 2015.

[A8] A. Kidess, S. Kenjereš, and C. R. Kleijn. The influence of surfactants on thermocapillary flow instabilities in low prandtl melting pools. *Physics of Fluids (1994-present)*, 28(6):062106+, June 2016.

[A9] A. Kidess, S. Kenjereš, B. W. Righolt, and C. R. Kleijn. Marangoni driven turbulence in high energy surface melting processes. *International Journal of Thermal Sciences*, 104:412–422, June 2016.

[A10] L. Aucott, A. Kidess, W. Mirahanage, S. Wen, R. Atwood, J. Marsden, X. Liang, M. Tong, T. Connolley, M. Drakopoulos, C. R. Kleijn, I. M. Richardson, D. J. Browne, R. Mathiesen, H. V. Atkinson, and H. B. Dong. Weld pool evolution and flow dynamics during welding of steels - a synchrotron study. *Nature: Scientific Reports*, 2016, submitted.